

UNIVERSITÀ DEGLI STUDI DI MILANO
FACOLTÀ DI SCIENZE E TECNOLOGIE

BACHELOR'S DEGREE IN PHYSICS

3D Inter-Fractional Monitoring in ^{12}C-Ion Treatments: Results from a Clinical Trial at CNAO Facility

Supervisor:
Dr. Ilaria Mattei

Co-supervisor:
Prof. Ivan Veronese

Candidate:
Alice Langella
ID Number: 994269

Academic Year 2025/2026

Contents

Introduction **v**

1 Charged Particle Therapy **1**
1.1 Charged Particle Interaction with Matter 1
1.1.1 Stopping Power 2
1.1.2 Bragg Peak 5
1.1.3 Range 6
1.1.4 Multiple Coulomb Scattering 7
1.1.5 Nuclear Fragmentation 8
1.2 Biological Effect of Radiation 10
1.2.1 DNA Strand Breaks 11
1.2.2 Linear Energy Transfer 11
1.2.3 Relative Biological Effectiveness 12
1.2.4 Survival Curve 13
1.2.5 Oxygen Enhancement Ratio 14
1.3 Range Monitoring in Particle Therapy 15
1.3.1 Treatment Planning System 15
1.3.2 Range Considerations 18

2 The Dose Profiler in the INSIDE System at CNAO **20**
2.1 CNAO Facility 20
2.2 The INSIDE System 21
2.3 Experimental Setup 22
2.3.1 Dose Profiler Design 22
2.3.2 Read-out and DAQ System 23
2.3.3 Rate Capability and Dead Time 25
2.4 INSIDE Clinical Trial 25
2.4.1 Clinical Workflow 25
2.4.2 Trial Population 27

3 Inter-Fractional Monitoring with the Dose Profiler **29**
3.1 Emission Point Reconstruction and 3D Emission Maps 29

3.1.1 Pixel Clustering 30
3.1.2 Track Reconstruction 30
3.1.3 Emission Point Evaluation 32
3.1.4 3D Emission Maps Reconstruction 33
3.2 Gamma Index Test 34
3.2.1 Gamma Index Definition 35
3.2.2 Tolerance Parameters 38
3.2.3 Hounsfield Units Maps 38
3.2.4 Parameter Optimisation 40
3.3 Validation via Monte Carlo Simulation 41
3.3.1 FLUKA Code 41
3.3.2 Patient Simulation 42

4 Results of Patient Data Analysis **44**
4.1 Patient 6 45
4.2 Patient 15 58
4.3 Patient 18 65

Conclusions **78**

Introduction

Over the centuries, different disciplines have often met and overlapped to expand their horizons. Physics and medicine provide a prime example: their encounter at the beginning of the 20th century marked the beginning of modern medical physics through the use of radiation for both diagnostic and therapeutic purposes. The idea of exploiting the energy loss that charged particles experience when travelling through a medium to treat cancer is attributed to Robert Wilson [1], and has been refined ever since. Due to technological limitations, the first operative clinical particle therapy facilities were only established in the 1990s, several decades after Wilson's proposal.

Today, malignant neoplasms represent one of the major healthcare challenges and remain the second leading cause of death worldwide [2]. Standard therapeutic strategies typically involve a combination of surgery, chemotherapy, immunotherapy, and radiotherapy. Conventional radiotherapy relies mainly on X-rays or electrons to induce irreversible damage to cancer cell DNA. However, the physical depth-dose profile of photons, characterised by an exponential absorption after an initial dose build-up, limits their ability to treat deep-seated tumours located close to organs at risk (OARs) without delivering unintended dose to surrounding healthy tissues. Hadrontherapy, or Charged Particle Therapy (CPT), overcomes such limitations by employing heavy charged particles, such as protons and carbon ions. Unlike photons, heavy charged particles deposit the majority of their energy at a spatially localised depth along their trajectory, thereby forming the Bragg peak. The Bragg peak's position can be precisely controlled by tuning the kinetic energy of the primary beam impinging on the target, maximising dose conformity to the tumour while sparing healthy tissues [3]. Among heavy charged particles, carbon-ions exhibit high Linear Energy Transfer (LET) and elevated Relative Biological Effectiveness (RBE), making them particularly suited for treating hypoxic and radioresistant tumours [4, 5]. Charged particle therapy is a growing clinical modality, with over a hundred operating facilities globally, including three active centres in Italy: CATANA in Catania, the Proton Therapy Center in Trento, and the Centro Nazionale di Adroterapia Oncologica (CNAO) in Pavia, which is the only italian facility capable of delivering both proton and carbon-ion treatments.

Despite its clinical advantages, range uncertainty is a challenge currently limiting the therapeutic potential of hadrontherapy. The spatial depth of the Bragg peak depends on the initial beam energy and the path traversed by projectile particles. Consequently, morphological variations (nasal cavity filling or emptying, or volume variations such as tumour

shrinkage) that may occur between treatment fractions, i.e. irradiation sessions, can shift the Bragg peak relative to its intended position. This shift may result in under-dosing the target volume and over-exposing adjacent healthy tissues to unnecessary radiation. While safety margins are introduced during treatment planning to mitigate range uncertainty risks, real-time or inter-fractional range monitoring is a useful tool to detect anatomical changes during the treatment course, providing clinicians with quantitative information supporting the evaluation of treatment replanning without requiring re-evaluation Computed Tomography (CT) imaging.

Because the primary beam stops within the patient, range monitoring techniques rely on detecting secondary radiation produced via nuclear interactions with tissue nuclei. Within this framework, the INSIDE (INnovative Solution for In-beam DosimEtry in hadrontherapy) collaboration developed a bimodal monitoring system installed in treatment room 1 at the CNAO facility. Specifically, in carbon-ion treatments the Dose Profiler (DP), a charged particle tracker designed to detect charged secondary fragments (predominantly protons and light ions) emitted at large angles with respect to the beam direction, is employed. Due to the spatial correlation between the production vertexes of charged secondary fragments and the primary beam's stopping region, the reconstructed three-dimensional emission distributions are an indirect observable for the detection of possible inter-fractional anatomical variations.

This thesis focuses on evaluating the performance and monitoring sensitivity of the Dose Profiler in detecting inter-fractional morphological changes during carbon-ion therapy. The analysis is primarily based on experimental data collected from a cohort of patients enrolled in a clinical trial conducted at CNAO (ClinicalTrials.gov Identifier: NCT03662373): two patients are from the second phase of the trial (2024-2026), and one selected case study from the first phase of the trial (2019) is validated through dedicated FLUKA Monte Carlo simulations.

The structure of this thesis is organised as follows. Chapter 1 introduces the physical mechanisms governing heavy charged particle interactions with matter, the principles behind hadrontherapy, and the causes of range uncertainties alongside current monitoring techniques. Chapter 2 presents the INSIDE experimental setup at the CNAO centre, describing the design, charged secondary particles tracking principles, and backtracking algorithms of the Dose Profiler, together with the clinical workflow of the trial. Chapter 3 outlines the data-analysis methodology, describing the event reconstruction pipeline including pixel clustering, the Hough transform, the charged secondary fragments emission maps, along with the mathematical framework of the gamma index test, optimisation metrics, and the Monte Carlo simulation setup. At last, Chapter 4 illustrates the analysis results of experimental and simulated data for the selected clinical cases (patients 6, 15, and 18), discussing parameter optimisation, sensitivity metrics, and the overall performance of the DP in identifying inter-fractional morphological variations.

Chapter 1

Charged Particle Therapy

Radiotherapy aims to treat cancer by targeting tumour cells to induce irreversible DNA damage, leading to malignant cell apoptosis, while sparing surrounding healthy tissues through the delivery of a conformal radiation dose. Consequently, radiotherapy is effective within a restricted dose range that represents a compromise between tumour control probability and normal tissue complication probability. One of the main goals of current research is to expand this therapeutic window by tailoring treatment plans more accurately to individual patients.

Radiotherapy can be classified into distinct categories depending on the type of radiation or particle employed [6]. Conventional external beam radiotherapy exploits highly energetic X-rays and γ-rays to reach deep-seated tumours. However, due to the photon build-up mechanism resulting from secondary electron production, the maximum dose is deposited close to the entrance channel. Therefore, overlapping multiple beams is fundamental to deliver the desired dose to the target volume, which increases the exposure of surrounding healthy tissue and the probability of unintended complications. Hadrontherapy, or Charged Particle Therapy (CPT), on the other hand, thanks to the characteristic behaviour of the interactions charged particles undergo inside a medium, is preferred for treating radioresistant tumours due to its high dose delivery precision. The most commonly used particles are protons and carbon ions, but several facilities exploit helium and oxygen ions as well. Employing heavier ions is not ideal, as it increases the contribution of nuclear fragmentation, which leads to an undesired tail in the dose-depth distribution and an overall loss of dose delivery precision [7].

1.1 Charged Particle Interaction with Matter

Although the interaction of all charged particles with matter is governed by Coulomb forces, the mechanisms of energy transfer and scattering depend on the mass of the projectile. Consequently, light and heavy particles require separate physical models. A charged particle is classified as heavy when its mass is significantly greater than the electron mass ($m \gg m_e$). Charged heavy particles lose energy primarily through inelastic Coulomb collisions with

atomic electrons. These interactions are classified into:

- *soft collisions*, in which energy transfer causes atomic excitation;
- *hard collisions*, where a larger energy transfer results in ionisation, i.e. the ejection of energetic secondary electrons known as δ-rays (or delta electrons) from the atom.

1.1.1 Stopping Power

As a heavy charged particle travels through a medium, it loses energy as it undergoes a sequence of interactions. Since the energy transferred in inelastic collisions with atomic electrons is extremely small relative to the particle's total kinetic energy, the slowing-down process can be modelled using the *Continuous Slowing Down Approximation* (CSDA). Elastic interactions with target nuclei result in negligible energy transfer and are the most responsible for particle scattering. Four different interaction modalities as a function of the semi-classical impact parameter b with respect to the absorber atomic radius can be identified [8]:

- *inelastic soft collisions* ($b \gg r_a$): the impact parameter is greater than the atomic radius. Although the energy transferred in each interaction is small ($\sim$ eV), these collisions occur with high frequency and account for the largest fraction of the total energy loss, causing the ejection of low-energy valence electrons.
- *inelastic hard collisions* ($b \approx r_a$): the impact parameter is of the order of the atomic radius. A heavy charged particle undergoes few inelastic hard collisions along its path compared to inelastic soft collisions. However, the energy transfer associated with these events is higher, and characteristic X-rays or Auger electrons can be expelled in the process.
- *elastic scattering* ($b \ll r_a$): the impact parameter is significantly smaller than the atomic radius. The heavy charged particle interacts with the electromagnetic field of the nucleus. Due to the high mass of the target nucleus relative to the projectile, energy transfer is negligible; however, significant angular deflection can occur during the interaction, as it is the primary mechanism for multiple Coulomb scattering.
- *inelastic scattering* ($b \approx 0$): the impact parameter is approximatively null, resulting in a direct collision with the nucleus associated with high energy loss. These interactions may cause target fragmentation and, if ions heavier than protons are involved, projectile fragmentation too.

The amount of energy lost per unit length by a charged particle inside matter is given by the *Stopping Power* (SP):

$$S(E) = -\frac{\mathrm{d}E}{\mathrm{d}x} \qquad \left[\frac{\mathrm{MeV}}{\mathrm{cm}}\right] \tag{1.1}$$

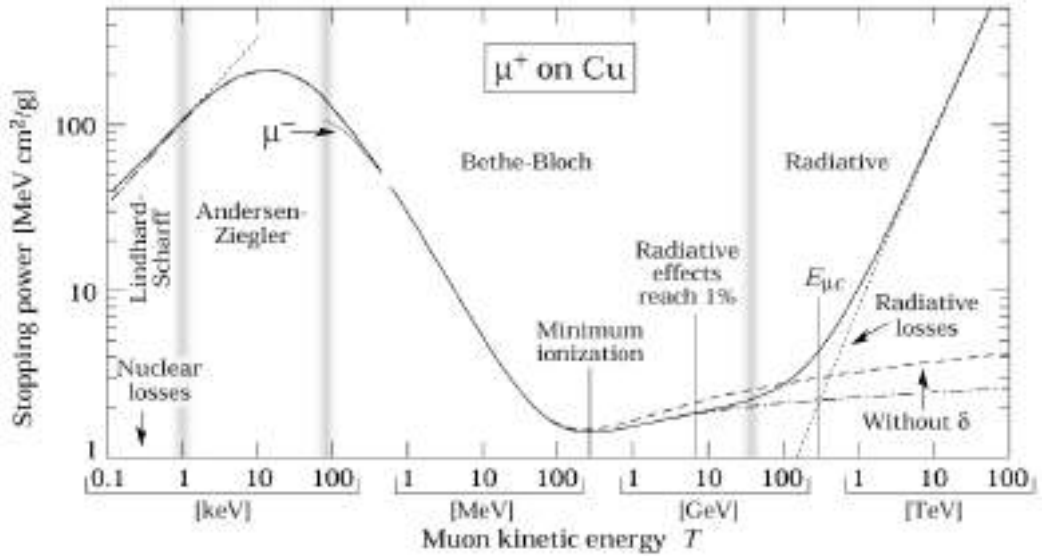

Figure 1.1: Mass stopping power for positive muons in a copper target as a function of their kinetic energy. Grey vertical lines represent boundaries between regions dominated by different physical interactions. Image from [9].

It can also be expressed normalised to the medium density ρ (*mass stopping power*):

$$\frac{S(E)}{\rho} = -\frac{1}{\rho}\frac{\mathrm{d}E}{\mathrm{d}x} \qquad \left[\frac{\mathrm{MeV}\cdot\mathrm{cm}^2}{\mathrm{g}}\right] \tag{1.2}$$

The total stopping power is evaluated as the sum of all the individual interaction contributions listed above:

$$S_{\mathrm{tot}} = S_{\mathrm{el}}^{\mathrm{hard}} + S_{\mathrm{el}}^{\mathrm{soft}} + S_{\mathrm{rad}} + S_{\mathrm{nucl}} \tag{1.3}$$

A first classical theoretical attempt to describe energy loss mechanisms involving charged particles is attributed to Niels Bohr (1913) [10]. Later on, a more precise quantum-mechanical description was achieved by Hans Bethe and Felix Bloch [11, 12]. Both theories rely on the fundamental hypothesis that the velocity and mass of the projectile particle are much greater than those of orbital electrons, and that energy loss via elastic nuclear scattering and radiative processes is negligible ($S \approx S_{\mathrm{el}}^{\mathrm{hard}} + S_{\mathrm{el}}^{\mathrm{soft}}$). Under such conditions, the Bethe-Bloch formula for collisional stopping power reads:

$$-\frac{\mathrm{d}E}{\mathrm{d}x} = 4\pi N_{\mathrm{A}} r_e^2 m_e c^2 \frac{Z_{\mathrm{p}}^2}{\beta^2}\rho\frac{Z_{\mathrm{t}}}{A_{\mathrm{t}}}\left[\frac{1}{2}\ln\left(\frac{2m_e c^2\beta^2\gamma^2 T_{\max}}{I^2}\right) - \beta^2\right] \tag{1.4}$$

where:

- N_{A} is Avogadro's number;
- m_e and r_e are the electron mass and the classical electron radius, respectively;
- Z_{t}, ρ, and A_{t} are the target atomic number, density, and atomic mass, respectively;

- Z_p and $\beta = v_\mathrm{p}/c$ are the projectile charge number and its velocity in units of the speed of light c;
- T_max is the maximum kinetic energy that can be transferred to an electron in a single collision;
- I is the mean excitation potential of the target medium;
- $\gamma = \frac{1}{\sqrt{1-\beta^2}}$ is the Lorentz factor.

Eq. (1.4) holds in the regime $0.1 \lesssim \beta\gamma \lesssim 1000$. To expand its validity range, additional correction terms must be included:

- **Shell correction:** As previously mentioned, Bethe's derivation relies on the assumption that the projectile velocity is significantly higher than the orbital velocity of bound electrons (Born's approximation). However, when the projectile slows down and its kinetic energy becomes comparable to that of orbital electrons ($\beta_\mathrm{p} \sim \beta_e \sim 1/137$), this assumption leads to an underestimation of the stopping power. To account for this effect, the shell correction term $C(\beta)/Z_\mathrm{t}$ is subtracted from Eq. (1.4).
- **Density correction:** As a relativistic charged particle traverses a condensed medium, its transverse electric field polarises the atoms, resulting in a screening effect that attenuates the Coulomb field of the projectile. Consequently, energy transfer during soft collisions is reduced, leading to a saturation of the relativistic rise in the stopping power. To account for this density effect, a correction term $\delta(\beta)/2$ is also subtracted from Eq. (1.4).

Taking both corrections into account, the complete Bethe-Bloch formula is given by [13]:

$$-\frac{\mathrm{d}E}{\mathrm{d}x} = 4\pi N_\mathrm{A} r_e^2 m_e c^2 \frac{Z_\mathrm{p}^2}{\beta^2}\rho\frac{Z_\mathrm{t}}{A_\mathrm{t}}\left[\frac{1}{2}\ln\left(\frac{2m_e c^2\beta^2\gamma^2 T_\mathrm{max}}{I^2}\right) - \beta^2 - \frac{\delta(\beta)}{2} - \frac{C(\beta)}{Z_\mathrm{t}}\right] \tag{1.5}$$

The following proportional expression better highlights the functional dependencies of the stopping power on the projectile's charge and kinetic energy, as well as on the properties of the traversed medium:

$$-\frac{\mathrm{d}E}{\mathrm{d}x} \propto \frac{Z_\mathrm{p}^2}{\beta^2}\rho\frac{Z_\mathrm{t}}{A_\mathrm{t}}\left[f(\beta) - \frac{C(\beta)}{Z_\mathrm{t}} - \frac{\delta(\beta)}{2}\right] \tag{1.6}$$

where $f(\beta) = \frac{1}{2}\ln\left(\frac{2m_e c^2\beta^2\gamma^2 T_\mathrm{max}}{I^2}\right) - \beta^2$.

The stopping power dependence on kinetic energy can be divided into four main regimes, as depicted in Figure 1.1. At very low energies, it rises with the velocity of the projectile until it reaches a maximum. In this region shell corrections cannot be neglected, as the particle's velocity approaches the orbital velocity of target electrons. Then the stopping power rapidly decreases as $1/\beta^2$ up to the absolute minimum corresponding to three to four

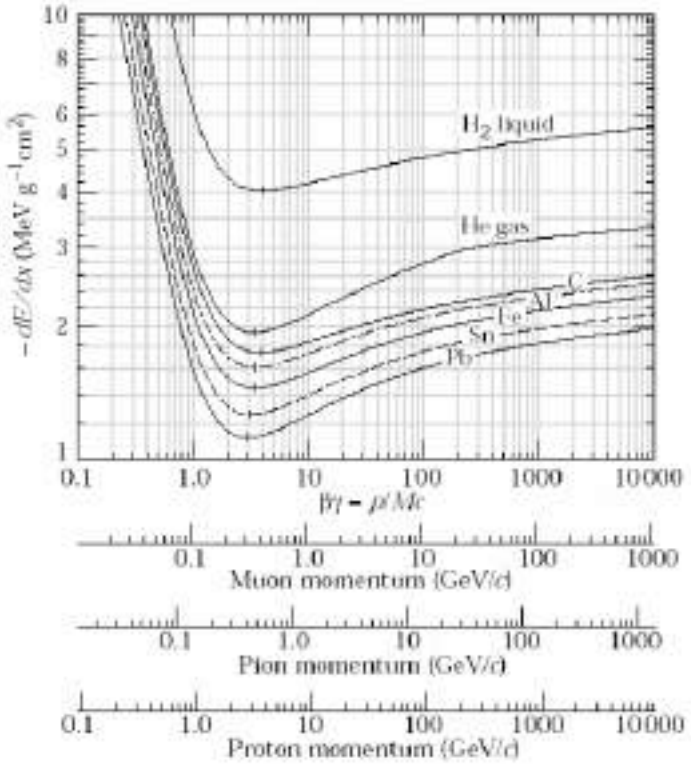

Figure 1.2: Mass stopping power for muons, pions, and protons in different target materials. Reproduced from [14].

times the rest mass energy of the projectile particle, where it acts as a *Minimum Ionising Particle* (MIP). As it enters the relativistic and the ultra-relativistic regimes, with the density correction playing a fundamental role in the latter, the stopping power undergoes a logarithmic relativistic rise.

The stopping power is proportional to the square of the projectile charge. Hence, once the stopping power for a proton is known it becomes fairly trivial to evaluate it for every other heavy charged particle travelling at the same velocity inside the same medium, as the stopping power does not depend on the projectile mass directly.

The Bethe-Bloch formula accounts for the properties of the absorber medium through three quantities: its density, the atomic number to mass number ratio, and the mean excitation potential. Except for hydrogen where $Z_\mathrm{t}/A_\mathrm{t} = 1$, the $Z_\mathrm{t}/A_\mathrm{t}$ ratio varies within a narrow range spanning from ≈ 0.5 for light elements to ≈ 0.4 for heavy elements. Overall, this causes a slight decrease in the mass stopping power as the atomic number of the target medium increases, as shown in Figure 1.2.

1.1.2 Bragg Peak

Eq. 1.5 shows that as a charged particle travels through matter its velocity progressively decreases, causing its stopping power to increase accordingly. Figure 1.3 (A) illustrates how, when the velocity of the projectile gets close to $\beta_\mathrm{p} \sim 10^{-2}$, the energy transfer to

the electrons of the medium reaches its maximum known as the *Bragg Peak* (BP). Beyond the BP, the charged particle begins to capture bound electrons from the medium and its charge Z decreases to an effective charge Z_{eff}, causing the stopping power to rapidly drop to zero. The width of the Bragg peak depends on range straggling phenomena arising from stochastic interactions between the projectile particle and the absorber medium, as well as on the lateral energy spread and the mass of the projectile [15].

Since the Bragg peak extension is on the order of a few millimetres, in charged particle therapy several beams accelerated to different energies are superimposed to obtain the *Spread-out Bragg Peak* (SOBP) shown in Figure 1.3 (B). It covers the depth of a tumoural volume, whereas the lateral extent of the target might be covered, for example, by deflecting the charged particle beam magnetically. By doing so, the entire target region receives a highly conformal radiation dose, providing superior precision compared with conventional photon radiotherapy, where surrounding healthy tissues are exposed to a higher risk of radiation toxicity [16].

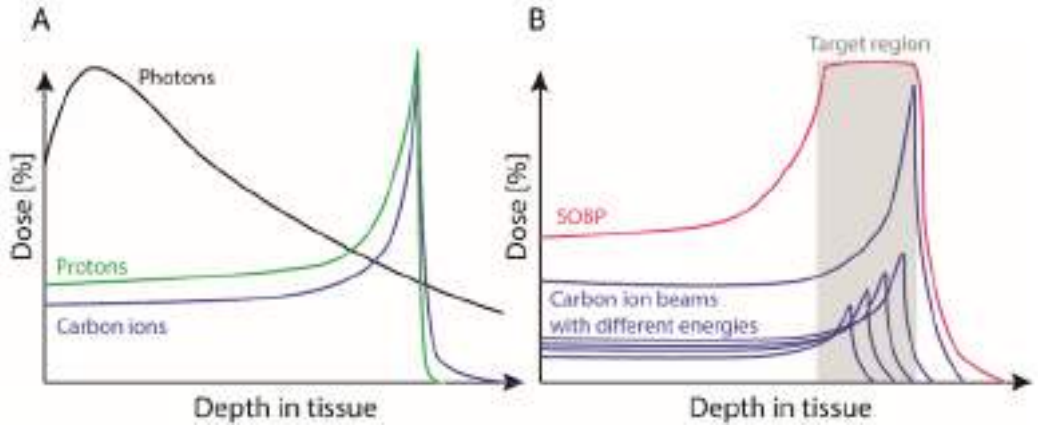

Figure 1.3: Left image (A): Depth-dose distribution of photon beam (black), proton beam (green) and carbon-ion beam (blue). Right image (B): The superposition of mono-energetic carbon-ion beams produces the Spread-out Bragg peak. Taken from [17].

1.1.3 Range

The expectation value of the distance covered by a charged particle along its path before it completely stops is defined as *range*. The range is a fundamental quantity in CPT, as it indirectly determines the beam energy required to reach a tumour or a lesion sitting at a certain depth. However, due to the stochastic nature of energy loss mechanisms, the range is not a fixed quantity as it depends on the number of collisions required to bring a moving particle to rest. These small range variations exhibit a Gaussian distribution centred around the mean range known as *range straggling*. When a light charged particle travels through a medium, it is more likely to experience scattering phenomena than heavy charged particles, the latter maintaining a straighter trajectory (see Figure 1.4, left). Figure 1.4 (right) shows the several range definitions that exist to better suit the particle type and the considered

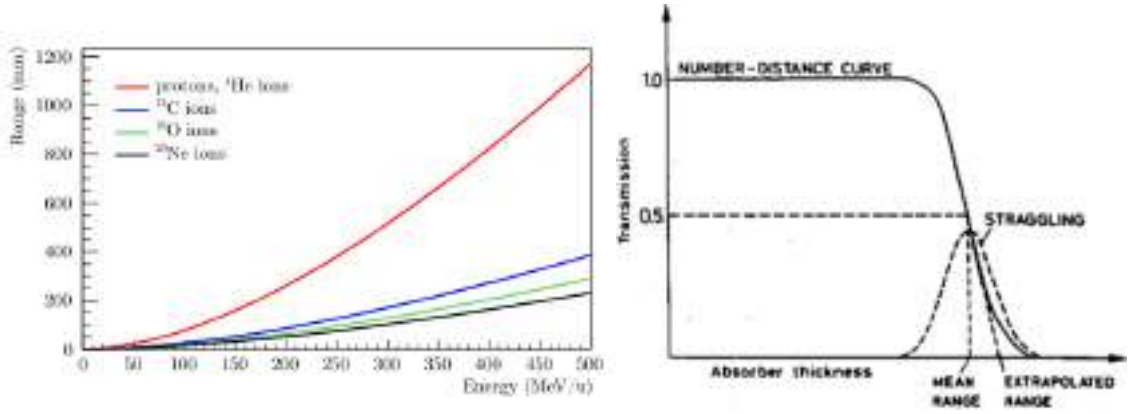

Figure 1.4: Left: CSDA range in water as a function of the energy for protons and ^{4}He (red line), ^{12}C (blue line), ^{16}O (green line) and ^{20}Ne (black line) ions. Originally published in [19]. Right: transmission curve plotted over the absorber thickness. Reproduced from [13].

application: the *extrapolated range* is identified by the intersection of the tangent to the transmission curve with the depth axis, whereas the *mean range* is the depth corresponding to the inflection point $I_0/2$, I_0 being the initial number of particles entering the medium. Due to the approximately rectilinear trajectory of heavy charged particles inside an absorber medium, the most suitable range definition to describe their interaction with matter is the *CSDA range* [18]:

$$R_{\mathrm{CSDA}}(E_0) = \int_0^{E_0} \frac{\mathrm{d}E}{S(E)} \tag{1.7}$$

This quantity can be experimentally determined by measuring the depth reached by a mono-energetic collimated particle beam impinging on a target.

1.1.4 Multiple Coulomb Scattering

Another fundamental process a charged particle experiences is multiple elastic scattering due to the interaction between the Coulomb field of the target nuclei and the particle itself. Figure 1.5 shows that the overall effect of multiple Coulomb scattering (MCS) does not translate into energy loss as much as spatial angular deflection of the projectile inside the medium, causing a lateral spread of the impinging beam that can be evaluated through the Full Width at Half Maximum (FWHM). The MCS is described by the Rutherford cross-section:

$$\frac{\mathrm{d}\sigma}{\mathrm{d}\Omega} = \left(\frac{Z_{\mathrm{p}} Z_{\mathrm{t}} e^2}{pv}\right)^2 \frac{1}{4\sin^4(\theta/2)} \tag{1.8}$$

and the Root Mean Square (RMS) angle follows an approximately Gaussian distribution according to the *Highland Approximation* [20]:

$$\theta_0 = \frac{13.6\,\mathrm{MeV}}{\beta cp} Z_{\mathrm{p}} \sqrt{\frac{\Delta x}{X_0}} \left[1 + 0.038 \ln\left(\frac{\Delta x}{X_0}\right)\right] \tag{1.9}$$

where βc, p, Z_p are the particle velocity, momentum and charge, respectively; Δx is the traversed medium thickness; and

$$X_0 = 716.4\ \mathrm{g/cm^2} \frac{A_\mathrm{t}}{Z_\mathrm{t}(Z_\mathrm{t}+1)\ln(287/\sqrt{Z_\mathrm{t}})} \tag{1.10}$$

is the radiation length of the absorber material; A_t and Z_t being the mass number and the atomic number of the target, respectively [21].
Eq. (1.9) shows that the spatial deflection is smaller for heavy and high-energy particles compared to light and slower ones, yielding a more significant effect to account for in proton therapy than in carbon-ion therapy.

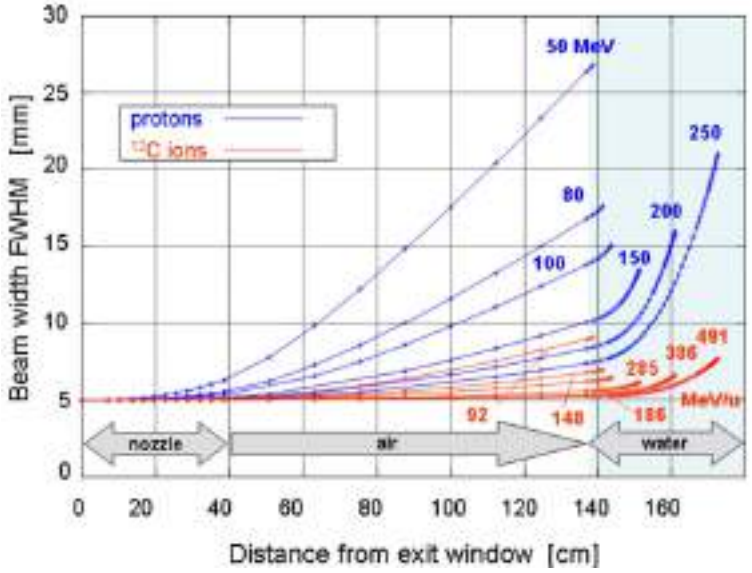

Figure 1.5: Monte Carlo simulation of lateral width evaluated at FWHM as a function of depth for proton beams (blue lines) and ^{12}C-ion beams (red lines) evaluated for different energies. Source: [22].

1.1.5 Nuclear Fragmentation

At the kinetic energies typical in hadrontherapy, spanning from tens up to hundreds of MeV/u, charged ions may overcome the Coulomb barrier. Therefore, nuclear interactions can occur leading to *target fragmentation* and/or *projectile fragmentation* if the projectile has $A_\mathrm{p} > 1$. Both processes result in the production of lower-mass and lower-charge secondary fragments, whose clinical implications vary depending on the originating mechanism.

To describe the dynamics of the above inelastic peripheral nuclear interactions, the *Abrasion-Ablation* model is commonly adopted [24]. Within its framework, the collision between nuclei, assumed to be approximately spherical, occurs in two stages. First, a fast abrasion phase takes place, during which the target and the projectile nuclei partially overlap, creating an excited reactive zone known as *fireball*. The ablation phase follows, where the fragments experience thermal de-excitation through nuclear evaporation processes

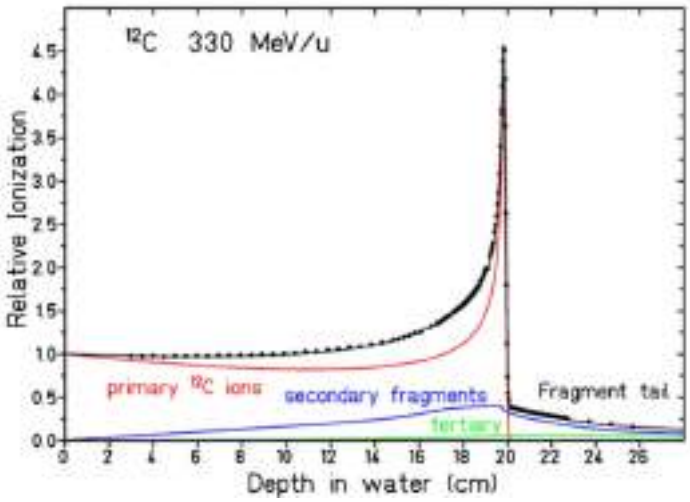

Figure 1.6: Depth-dose distribution in water for a 330 MeV/u ^{12}C-ion beam, highlighting the individual physical components. The energy deposition from primary carbon ions is shown in red, whereas the secondary and tertiary nuclear fragment contributions are depicted in blue and green, respectively. The overall depth-dose profile resulting from the sum of all components is illustrated by the black curve. Originally published in [23].

that lead to the emission of prompt gamma rays and light particles such as protons and neutrons. A schematic representation is provided by Figure 1.7.

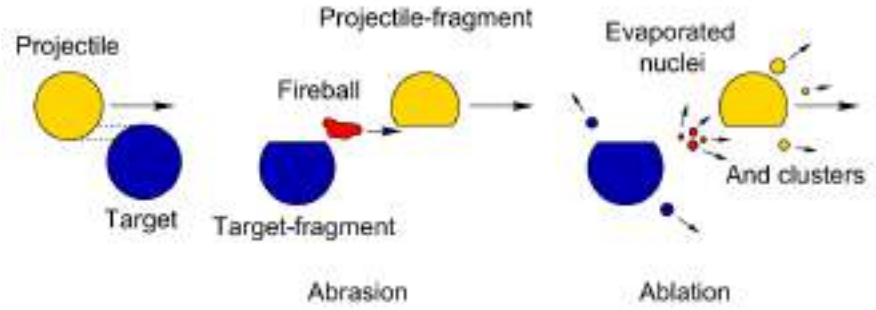

Figure 1.7: Schematic representation of the two-stage abrasion-ablation model. Adapted from [25].

Secondary particles produced due to target fragmentation are likely to have a short range, depositing their energy close to the interaction point and playing a key role mostly in the entry channel, whereas secondary projectile fragments are forward-peaked and their long range creates the distinctive dose tail beyond the Bragg peak observed in heavy-ion beams, as depicted in Figure 1.6. The overall result is a loss in precision of the delivered dose, both in the transverse plane and in the longitudinal direction, with a greater risk of damaging surrounding healthy tissues, as the effects of nuclear fragmentation are not currently fully taken into consideration in treatment plans. The lack of data regarding cross-sections in such processes at therapeutic energies remains an area of ongoing research; nonetheless, energetic secondary fragments that escape the patient's body are currently exploited for

range-monitoring purposes.

1.2 Biological Effect of Radiation

The interaction between a radiation field and matter can be described in terms of dosimetric quantities resulting from the product of a radiation field quantity and an interaction coefficient characteristic of the medium. The fundamental dosimetric quantity in particle therapy is the *absorbed dose*, defined as the energy absorbed by the tissue per unit mass:

$$D = \frac{\mathrm{d}E}{\mathrm{d}m} \qquad [\mathrm{Gy}] \tag{1.11}$$

where the gray (Gy) is a derived dimensional unit defined as one joule per kilogram.

However, the absorbed dose is a purely physical quantity that does not account for biological aspects, such as the radiosensitivity of different tissues or the ionisation density of the therapeutic beam. These factors, along with the tissue's ability to repair radiation damage, must be considered in conventional radiotherapy as well as in hadrontherapy. In radioprotection, two variables derived from the absorbed dose have been introduced to quantify radiation exposure risks: the *equivalent dose* and the *effective dose* [26].

The equivalent dose measures the biological effects of radiation on a specific tissue or organ T:

$$H_T = \sum_R w_R D_{T,R} \qquad [\mathrm{Sv}] \tag{1.12}$$

where w_R is the radiation weighting factor for a radiation type R, $D_{T,R}$ is the average absorbed dose delivered to tissue T, and the sum runs over all radiation types involved. Dimensionally identical to the gray, the equivalent dose is expressed in sieverts (Sv) to distinguish radioprotection-related quantities from the absorbed dose.

The overall risk of radiation-induced stochastic effects on the whole organism is quantified by the *effective dose*. It is defined as the weighted sum of the equivalent doses over all tissues and organs in the human body:

$$E = \sum_T w_T H_T \qquad [\mathrm{Sv}] \tag{1.13}$$

where w_T is the tissue weighting factor.

After radiation exposure, both deterministic and stochastic effects may arise. Deterministic effects (such as erythema and cataracts) manifest above a dose threshold and their severity worsens with the received dose. Stochastic effects (like chromosomal aberrations or cancers) occur with no dose threshold, but their probability of occurrence increases with the dose despite their extent being independent from it.

1.2.1 DNA Strand Breaks

The main aim in particle therapy is to kill tumour cells by inducing DNA damage that triggers their apoptosis, as the key difference between cancer cells and normal cells resides in the greater self-repair capacity of the latter. Cellular damage caused by ionisation and excitation processes can be either *direct*, when the directly-ionising particles such as protons or carbon-ions interact with the DNA structures breaking molecular bonds in the process, or *indirect*, when damage occurs via highly reactive hydroxyl free radicals OH generated through water ionisation by secondary electrons resulting from photon interactions with the medium [27] (see Figure 1.8 (a)).

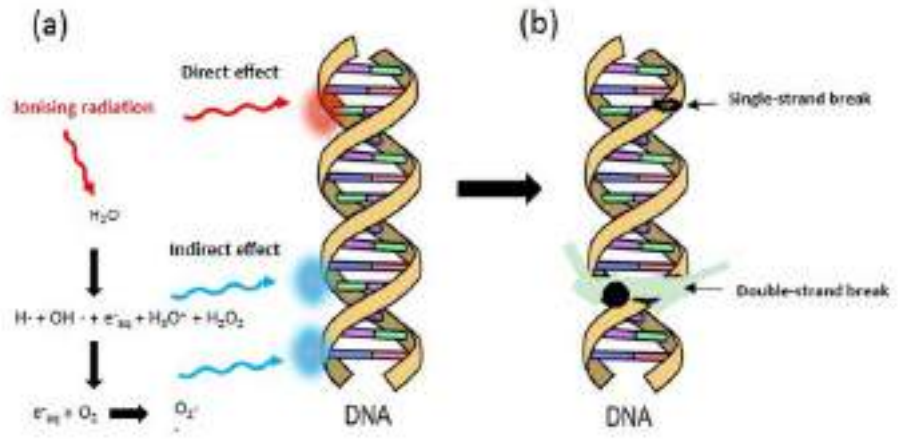

Figure 1.8: Illustration of radiation-induced DNA damage pathways: (a) direct action via targeted energy deposition within the DNA structure; (b) indirect action mediated by reactive oxygen species. Both mechanisms may induce isolated single-strand breaks (SSBs) or double-strand breaks (DSBs). Image from [27].

DNA damage is mainly classified into the following categories, listed in order of increasing severity: base damage, Single-Strand Breaks (SSBs), and Double-Strand Breaks (DSBs) (see Figure 1.8 (b)). Although base damage and single-strand breaks can be proficiently repaired, double-strand breaks are more challenging and generally lethal [28]. The efficiency of DNA repair mechanisms also depends on the cell cycle phase during irradiation, a feature widely exploited in clinical settings as it has been observed that tumour cells tend to synchronise their cycle phases between treatment fractions [29].

1.2.2 Linear Energy Transfer

A fundamental quantity in radiobiology and dosimetry is the *Linear Energy Transfer* (LET). While the stopping power is defined as the energy lost per unit length by a charged particle, the LET describes the same concept from the opposite perspective, focusing on the energy transferred to the medium by the primary ionising track.

The LET is often introduced alongside an energy cut-off Δ to exclude energy deposition by secondary electrons far from the primary track [30]. Consequently, it can be more

specifically defined as the difference between the energy lost per unit length by an ionising particle due to electronic collisions and the kinetic energy (per unit length) of secondary electrons exceeding the threshold. In other words, the LET represents the ionisation density of the primary track:

$$\mathrm{LET}_\Delta = \frac{\mathrm{d}E_\Delta}{\mathrm{d}x} \qquad \left[\frac{\mathrm{keV}}{\mu\mathrm{m}}\right] \tag{1.14}$$

Different radiation types are broadly classified into low-LET when ranging from 0.2 to 2 keV/μm, or high-LET if they fall into the 50 - 200 keV/μm interval. Within the therapeutic energy range, high-LET radiation such as carbon ions has a higher probability of inducing lethal cellular damage compared to low-LET radiation. A schematic representation of the difference between a proton and a carbon-ion track is presented in Figure 1.9, illustrating the higher density of secondary electrons produced by carbon ions that leads to enhanced DNA damage. Photons, electrons, and protons are examples of sparsely-ionising, low-LET particles. Moreover, high-LET radiation (i.e. carbon ions) is highly ionising, making it particularly effective in treating radio-resistant cancer thanks to its dense energy deposition per unit length. On the other hand, due to their greater therapeutic precision and the lack of a fragmentation tail, protons are more suited for treating tumours in close proximity to organs at risk.

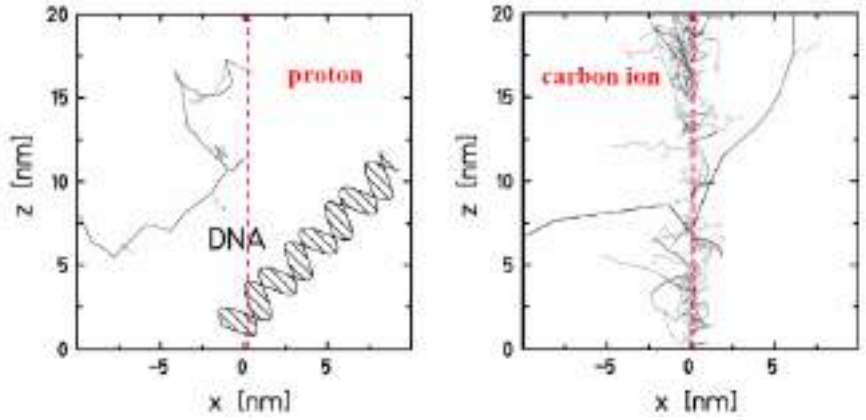

Figure 1.9: Secondary electrons produced by protons and ^{12}C ions with a schematic scale representation of a DNA molecule. Source: [31].

1.2.3 Relative Biological Effectiveness

As previously mentioned, the physical dose alone is not sufficient to describe biological effects, as they depend on several parameters such as the radiation type, the irradiated tissue, and the dose fractionation. In radiobiology, the *Relative Biological Effectiveness* (RBE) is a dimensionless quantity defined as the ratio between the dose of a reference radiation (e.g. gamma-rays from ^{60}Co) and the dose of a given radiation, evaluated for the same biological effect [32]:

$$\mathrm{RBE} = \frac{D_\gamma}{D_{\mathrm{test}}}\Big|_{\mathrm{iso}} \tag{1.15}$$

The RBE is not a uniquely determined quantity; rather, it varies as a function of both physical parameters and biological parameters, such as the specific cell line, dose rate, tissue oxygenation, dose fractionation, and tissue radiosensitivity. The RBE depends on the LET: it increases up to a maximum value depending on the particle type, and then it decreases. If the ionisation density is such that the distance between two consecutive interactions is significantly smaller than the DNA double helix diameter, the RBE plateaus before decreasing and an overkill effect occurs, as the excess energy is deposited into already damaged molecules. On account of that, nuclear fragmentation is not the only reason why $Z > 8$ ions are not employed in hadrontherapy (see Section 1.1.5), as the outcome would not translate into a greater cell killing efficiency.

The RBE is conventionally assumed to be 1 for photons and set at 1.1 for protons [4], while the evaluation for carbon ions is more complicated due to the contribution of nuclear fragmentation, and it ranges between 3-4 in the SOBP region.

To link the physical and the biological aspects discussed above, another key quantity is introduced. The *biological dose* represents the tissue damage, it is defined as follows and it is measured in *Gray equivalent* (GyE):

$$D_{\text{bio}} = \text{RBE} \times D_{\text{phys}} \tag{1.16}$$

To guarantee that this quantity is as homogeneous and conformal as possible within the treatment plan, the physical dose has to be modulated to compensate for the LET variations along the beam track.

1.2.4 Survival Curve

An experimental evaluation of the RBE is derived from *cell survival curves*. In order to compare the biological effects of different radiation types, these curves describe the fraction of cells retaining their reproductive capacity as a function of the absorbed dose.

The *Survival Fraction* (SF) is defined by the *Linear-Quadratic model* (LQ) model as follows:

$$S(D) = \exp\left(-\alpha D - \beta D^2\right) \tag{1.17}$$

where the α and β parameters represent the intrinsic radiosensitivity of the considered tissue. More specifically, α determines the initial slope of the survival curve, and β its curvature [33]. The linear term is dominant when lethal cell damage is caused by a single ionisation event, whereas the quadratic component is dominant when two independent interactions lead to double strand breaks in DNA.

The α/β ratio is a measure of tissue radiosensitivity. While low α/β values ($\leq$ 4 Gy) identify *late-responding* tissues (such as prostate cancer), high α/β values ($\geq$ 10 Gy) correspond to *early-responding* tissues like skin, mucosa, and most fast-proliferating tumours [33].

These radiobiological responses justify dose-fractionation in clinical treatment planning,

as this method spares late-responding tissues from unnecessary radiation toxicity while keeping tumour control. Hence, the survival curve equation reads [34]:

$$S(n,d) = \exp\left(-\alpha d - \beta d^2\right)^n \tag{1.18}$$

where n is the overall number of fractions and d is the delivered dose per fraction.

To compute the RBE for clinical purposes, radiobiological models are required. Among these, the *Local Effect Model* (LEM) is a commonly adopted approach within the LQ framework [35]. It relies on the hypothesis that [32]:

1. The biological effect is entirely determined by the local dose distribution within the cell nucleus;
2. Biological damage depends solely on the expectation value of the local energy deposition;
3. The cell nucleus is assumed to be homogeneous, with constant density and radiosensitivity.

1.2.5 Oxygen Enhancement Ratio

An additional factor to account for is the oxygenation level in the clinical target volume, as the oxygen level in irradiated tissues influences their response to radiation. When a tumour grows, new capillaries form to oxygenate the mass; however, hypoxic regions may form in its innermost and central parts, reducing the overall tissue radiosensitivity. The influence of oxygen content on survival fraction curves for different radiation types, energies, and LET levels is depicted in Figure 1.10.

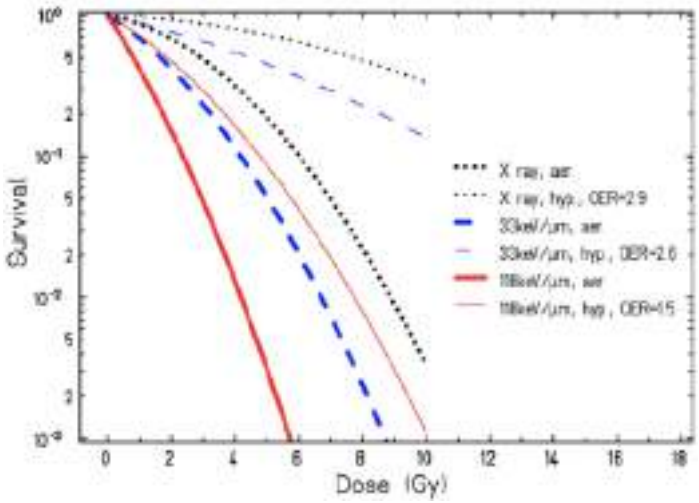

Figure 1.10: Secondary electrons produced by protons and ^{12}C ions with a schematic scale representation of a DNA molecule. Reproduced from [36].

The *Oxygen Enhancement Ratio* (OER) accounts for this phenomenon. It is defined as the ratio of the dose required under hypoxic conditions to that required under aerobic

conditions to achieve the same biological effect:

$$\mathrm{OER} = \frac{D_{\mathrm{hypoxic}}}{D_{\mathrm{aerobic}}}|_{\mathrm{iso}} \tag{1.19}$$

Since hypoxic tissues require higher deposited dose than aerobic ones to obtain the same biological effect due to damage being indirectly inflicted by hydroxyl free radicals, low-LET radiation is further identified by high-OER values. Conversely, high-LET radiation has lower OER values, as it causes mainly direct damage which is independent of oxygen.

1.3 Range Monitoring in Particle Therapy

Particle therapy is a highly selective treatment modality, aiming at targeting cancer tissue while sparing healthy tissue and organs at risk around it. To achieve such therapeutic precision, it is fundamental that the target volume is conformally and homogeneously irradiated. The greater precision of hadrontherapy compared to conventional radiotherapy is often exploited to treat deep-seated tumours and lesions, located close to organs at risk. However, this characteristic makes it more sensitive to spatial uncertainties in the SOBP positioning. Furthermore, the treatment planning has to account for many factors including biological uncertainties, possible inter-fractional morphological variations, nuclear fragmentation mechanisms, and spatial degradation of the pencil beam due to MCS interactions. Altogether, these factors may lead to a total spatial uncertainty of the irradiated area up to a few millimetres [37], resulting in unintended underdosage of the clinical target or an overdosage of surrounding organs at risk and healthy tissues.

Within this framework, range monitoring serves as a valid verification tool to mitigate the above-mentioned uncertainties and to develop accurate treatment plans tailored to each patient.

1.3.1 Treatment Planning System

The main purpose of the Treatment Planning System (TPS) is to build therapeutic plans adapted to the individual patient anatomy by combining their anatomical data (medical history, tumour location and volume, adjacent organs at risk) acquired through an imaging technique such as the Computed Tomography (CT) or Magnetic Resonance Imaging (MRI), with beam-delivery parameters available in clinical facilities, such as the quality of the radiation or particle species exploited.

In Report 50 (1993) and Report 62 (1999) [38], the International Commission on Radiation Units and Measurements (ICRU) defined the following conventional definitions of target volumes adopted in the TPS (see Figure 1.11):

- **Gross Tumour Volume** (GTV): the cancerous mass extent identified by imaging;
- **Clinical Target Volume** (CTV): the volume including the GTV and the surrounding area accounting for possible tumour growth as well as microscopic lesions;

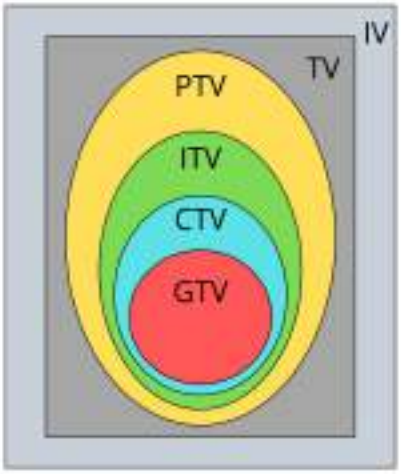

Figure 1.11: Clinical volumes defined by ICRU Report 50.

- **Internal Target Volume** (ITV): the volume consisting of the CTV and additional Internal Margins (IM) to include organ motion contributions (e.g. respiration or cardiac cycle);
- **Planning Target Volume** (PTV): a geometric concept that encompasses the CTV and safety Setup Margins (SM) due to instrumental uncertainties. Its purpose is to guarantee the appropriate amount of radiation, considering CT and dose delivery uncertainties, is delivered to the CTV;
- **Treated Volume** (TV): the volume within an isodose curve that leads to the achievement of the treatment goal;
- **Irradiated Volume** (IV): the volume receiving a dose level such that it could result in healthy tissue toxicity.

In radiotherapy, a treatment plan consists of several steps. To acquire patient specific anatomical data and assess the tumour position and volume, a planning CT scan is acquired a few days prior to the first treatment fraction. Moreover, information extracted from diagnostic imaging is fundamental both for the radiation oncologist, allowing target volume identification, and for the TPS to optimise the patient-specific treatment plan.

The CT image is divided into unit elements called voxels, each assigned a Hounsfield Unit (HU) value that represents the local tissue density. More specifically, the Hounsfield Units are defined as:

$$\mathrm{HU} = 1000 \times \frac{\mu - \mu_{\mathrm{water}}}{\mu_{\mathrm{water}} - \mu_{\mathrm{air}}} \qquad -1000 \leq \mathrm{HU} \leq 3500 \tag{1.20}$$

where μ_{water}, μ_{air}, and μ represent the linear attenuation coefficient of distilled water (at standard temperature and pressure conditions), air, and the traversed tissue, respectively.

Dose-Volume Histograms (DVH) represent a useful tool for the definition of the tumour control probability as well as for treatment-plan validation and verification.

Since it is not possible to irradiate malignant cells only while completely sparing surrounding healthy tissue, *dose constraints* are defined to achieve an optimal compromise. A minimum percentage threshold is established on the target to ensure it receives the prescribed dose; on the other hand, another percentage criterion is imposed on organs at risk to verify the dose deposited remains within the tolerance limits. One of the most commonly employed dose-constraints parameter is the *D50*. Geometrically identified with the tangent point corresponding to the 50% of the TCP curve, it evaluates the dose required to obtain a 50% tumour control probability.

Uncertainty sources such as CT artefacts, CT stoichiometric conversion from Hounsfield Units to tissue densities, patient mispositioning, intrinsic uncertainties due to instrumental resolution, and organ motion have to be carefully considered within the TPS. Their effects are accounted for by safety margins, the only exception being possible anatomical changes, as variations in tissue density result in an under- or over-dosage of therapeutic radiation and a degradation in dose delivery precision. Range monitoring aims to mitigate these uncertainties by detecting secondary particles produced during primary beam interactions with the target volume. Moreover, it serves as a fundamental practice to assess if an imaging re-evaluation is necessary, a decision currently established considering the treated pathology clinical history rather than patient-specific information. The possibility to monitor morphological variations is essential to decide whether a treatment re-planning is required.

Two different monitoring strategies are under investigation by the scientific community: *inter-fractional* monitoring and *intra-fractional* monitoring. While the first one compares different treatment fractions, the latter focuses on real-time range detection during dose delivery. Examples of secondary particles exploited for range monitoring include:

- β^+ **emitters:** Positron-emitting isotopes generated via target and projectile fragmentation. They produce pairs of back-to-back 511 keV photons by positron-electron annihilation, which are detected via Positron Emission Tomography (PET) [39];
- **Prompt γ-rays:** High-energy photons emitted after the de-excitation of target nuclei excited by nuclear interactions [40];
- **Charged fragments:** Secondary ions with $Z > 1$ and protons generated during projectile fragmentation [41];
- **Neutrons:** particles generated by nuclear interactions between the primary beam and the target [42].

The primary advantage of range monitoring in particle therapy resides in the high-efficiency tracking of secondary particles, despite the low event statistics. Moreover, secondary projectile charged fragments must be sufficiently energetic in order to traverse and exit the patient's body, leading to a particularly challenging detection in case of deep-seated tumours.

This thesis focuses on charged fragments emitted during projectile fragmentation, especially protons and light ions, as they are exploited by the Dose Profiler detector (see Chapter 2) for the range monitoring application described in Section 1.3.2.

1.3.2 Range Considerations

While nuclear fragmentation is a phenomenon occurring in proton therapy, it involves target fragmentation only. However, charged secondary fragments resulting from this mechanism are not suitable for range monitoring purposes, as their short range ensures their absorption within the patient's body. Conversely, in carbon-ion hadrontherapy projectile fragmentation commonly occurs, leading to the production of charged secondary particles with kinetic energy exceeding 100 MeV and velocities comparable to those of the impinging particle beam. Despite a small fraction of them being unable to escape the traversed medium, the majority of the produced projectile fragments are able to successfully reach external detectors, rendering them a valid range monitoring tool.

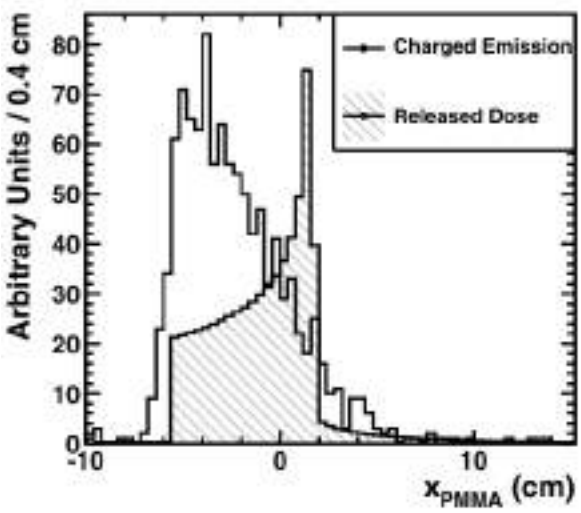

Figure 1.12: Charged secondary particles measured at 90° from the interaction of a ^{12}C-ion beam of 220 MeV/u impinging along the x direction on a PMMA target (solid line curve). The superimposed dashed area depicts the dose-depth distribution. Originally published in [43].

Charged secondary fragments are predominantly forward-peaked; nonetheless, a non-negligible fraction, mainly consisting of protons and light ions, is emitted at wider angles, as for example 60°, 90°, and even beyond, where the detection efficiency is limited by the steep drop in particle statistics. Despite spatial degradation due to multiple Coulomb scattering before exiting the target, the high tracking efficiency of a charged secondary particles detector and the straightforward discrimination of the neutron background represent fundamental assets for range verification due to the correlation between the position of the Bragg peak and the emission intensity of secondary fragments.

However, Figure 1.12 shows that the emission profiles of secondary protons along the beam axis and the released dose within the target are anti-correlated: as the penetration

depth of the primary beam increases, the deposited dose progressively rises while the measured fragmentation yield of secondary particles decreases. This results in higher detected statistics associated with lower-energy, superficially-emitted fragments.

Chapter 2

The Dose Profiler in the INSIDE System at CNAO

As discussed in Chapter 1, hadrontherapy is an advanced form of radiotherapy that employs charged particles such as protons and light ions to maximise the biological damage to tumour cells while sparing surrounding healthy tissues and organs at risk. These characteristics make it particularly effective in treating radio-resistant and surgically inoperable tumours. However, the potential of hadrontherapy is not yet fully exploited within clinical practice, due to large safety margins (2.5-3% of the range) that must be adopted to account for beam range uncertainties affecting the overall treatment effectiveness, as explained in Section 1.3. Research into methods to reduce safety margins, such as range monitoring techniques, is fundamental to maintain the superior precision and selectivity that characterise light-ion therapy compared to conventional X-ray radiotherapy.

Within this framework, the INSIDE (INnovative Solutions for In-beam Dosimetry in hadronthErapy) collaboration (see Section 2.2) has developed a dual-mode integrated monitoring system consisting of two online, inter-spill, planar PET scanners, and the Dose Profiler (DP), a charged secondary fragment tracker built for inline, in-beam range monitoring purposes. These devices have been installed and tested at the Centro Nazionale di Adroterapia Oncologica (CNAO, Pavia, Italy) described in Section 2.1.

This thesis evaluates the performance of the Dose Profiler detector for inter-fractional monitoring, analysing data from a cohort of carbon-ion therapy patients enrolled in a clinical trial at the CNAO facility (see Section 2.4.2), and comparing the results against Monte Carlo simulations (see Chapter 4).

2.1 CNAO Facility

The Centro Nazionale di Adroterapia Oncologica, located in Pavia, Italy, is a clinical and research foundation established in the spring of 2001. It is the only italian facility providing hadrontherapy with both proton and carbon ion beams. Located in a $1600\,\mathrm{m}^2$ bunker, the CNAO synchrotron (shown in Figure 2.1) circumference measures 80 m, and it is capable of

accelerating protons up to energies of 250 MeV and carbon ions up to 400 MeV/u.

Treatment delivery relies on an active pencil-beam scanning technique, where the dose is conformally distributed to the target volume by steering the beam with dipole magnets and adjusting its kinetic energy to precisely modulate the Bragg peak spatial depth.



Figure 2.1: The synchrotron accelerator at the CNAO facility. Ion sources within its ring create particle bunches of protons or carbon ions, which are selected via magnetic fields. After pre-acceleration, these bunches are injected into the synchrotron where are accelerated before delivery to three treatment rooms. Image from [44].

2.2 The INSIDE System

The INSIDE project developed the first bimodal system designed for in-vivo monitoring of carbon-ion and proton beams employed in hadrontherapy, exploiting secondary particles emitted during the interaction of the therapeutic beam with the patient's body.

Financed by MIUR (Ministero dell'Istruzione, dell'Università e della Ricerca) and first proposed in 2013, INSIDE is the result of a broad collaboration including the physics departments at the Universities of Turin, Pisa, Sapienza University of Rome, and the Polytechnic University of Bari, along with the Centro Fermi, INFN (Istituto Nazionale di Fisica Nucleare), and the CNAO foundation.

Both the identical planar PET heads (10×20 cm^2) and the DP are installed in treatment room 1 at the CNAO facility and held at a fixed position and distance from the patient by a cart, as shown in Figure 2.2. While the former aims to reconstruct the β^+ activity map by detecting the back-to-back-emitted photons produced [39], the Dose Profiler detector (whose characteristics will be further discussed in Section 2.3) is a scintillating fibres tracker designed to evaluate inter-fractional morphological variations by reconstructing the spatial emission profile of charged secondary particles.

This thesis centres on the Dose Profiler detector, whose data acquired during the clinical trial (see Section 2.4) are analysed in Chapter 4 following the methodological framework outlined in Chapter 3. Information regarding the DP presented in the following sections is derived from Traini et al. [46].

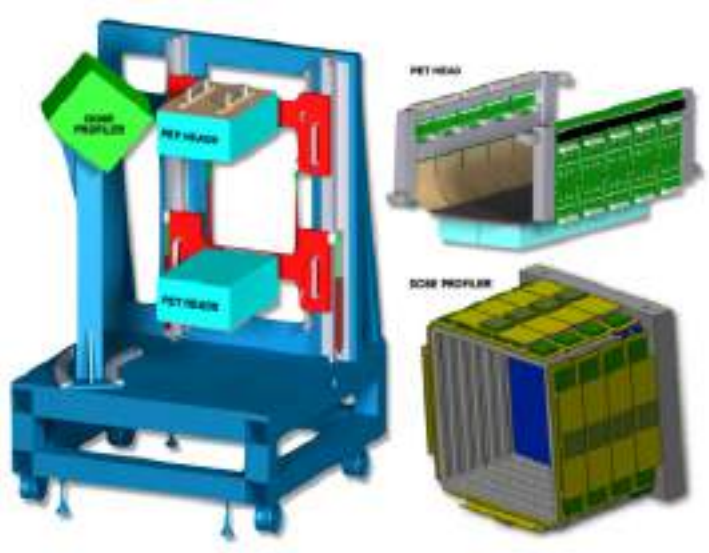

Figure 2.2: Schematic representation of the INSIDE system installed at the CNAO facility: in red the allowed movements of the PET heads (turquoise) are displayed, in green the Dose Profiler detector. On the right simulated prototypes of a PET head and the mechanical structure of the DP are shown. Image from [45].

2.3 Experimental Setup

The Dose Profiler was developed and built at the SBAI (Basic and Applied Sciences for Engineering) department of the Sapienza University of Rome for operation in clinical settings. Specifically, it aims to efficiently detect mainly protons and deuterons with kinetic energy ranging from 50 to 200 MeV/u, while simultaneously maximising the collectible statistics to achieve viable range monitoring requirements.

2.3.1 Dose Profiler Design

Completed in 2017, the Dose Profiler was designed to feature a tracker, aiming to detect charged fragments. More specifically, the tracking detector consists of eight subsequent planes contained within a light-tight aluminium frame (see Figure 2.3, right) and it is further covered by a 50 μm thick Tedlar (a polyvinyl fluoride film, PVF) layer on the entrance side. Each module comprises two orthogonal layers of square-sectioned (500×500 μm^2), double-cladding, Saint-Gobain BCF-12 plastic scintillator fibres with light yield $\approx$ 8000 ph./MeV, resulting in a total of 384 fibres per layer.

When a charged particle traverses the detector, a fraction of its deposited kinetic energy is converted into a light signal and transported by total internal reflection mechanisms with a 7.2% efficiency to the Silicon Photomultiplier (SiPM) read-out system located at the fibre ends. This allows the three-dimensional reconstruction of the impinging particle: the planar coordinates are given by the intersection of the orthogonal fibres identified at the interaction point, while the longitudinal coordinate is conventionally taken as the position of the fibre-plane centres along the primary beam direction.

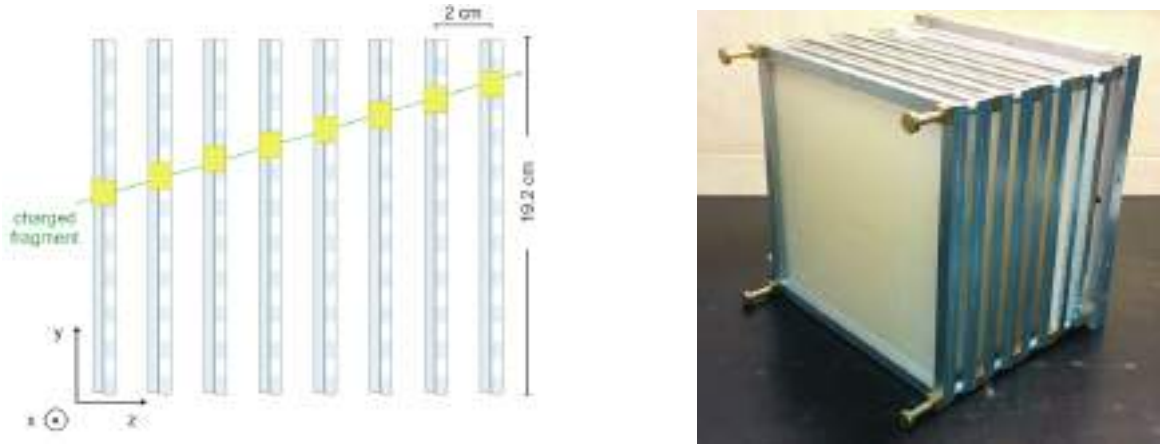

Figure 2.3: Working principle and structural layout of the Dose Profiler. Left: schematic diagram illustrating the fragment detection mechanics. Energy depositions within the scintillating fibre layers (light blue) are highlighted by yellow squares, while the reconstructed particle trajectory is depicted in green. Right: photograph of the DP detector planes during the assembly phase. Reproduced from [46].

To achieve the best trade-off between the mechanical constraints set by the PET-integrated system, the maximum angular acceptance, and the minimum back-tracking resolution, the inter-planar distance between consecutive modules is set to 2 cm. Hence, the total DP volume is $\approx 30 \times 30 \times 30\,\mathrm{cm}^3$, read-out system included, with an active detection area measuring $19.2 \times 19.2\,\mathrm{cm}^2$, as shown in Figure 2.3 (left). It is deployed at ≈ 50 cm from the room isocentre, with a tilt angle of 60° along the beam direction, enabling an angular coverage of ≈ 0.15 sr.

2.3.2 Read-out and DAQ System

As already mentioned in Section 2.3.1, the light signal generated through the interaction between a charged particle and the detector is captured by SiPMs situated at the fibre ends, thereby defining a "detector hit". More specifically, to reduce the inevitable dead space between the fibres where the sensor packaging is installed, 192 Hamamatsu S12571-050P SiPMs (characterised by an active detection area of $1\,\mathrm{mm}^2$) are housed on two rectangular boards, each coupled to ≈ 2 adjacent fibre pairs located on opposite ends. Four boards are required in total to read the x and y coordinates from two planes, the resulting module is referred to as a *bi-plane* unit. The complete detector coverage is provided by 16 boards, altogether resulting in 3072 read-out channels.

The SiPMs are read out by a 32-channel custom ASIC system known as BASIC32ADC, a CMOS (Complementary Metal-Oxide-Semiconductor) technology specifically designed for medical imaging applications. The boards house 96 BASIC32ADC units, connected with the central data acquisition system through 16 FPGAs (Field Programmable Gate Arrays), i.e. software-programmable integrated circuits. Moreover, the boards are surrounded by aluminium bars connected to a cooling water-circuit kept at 12° to dissipate heat and to

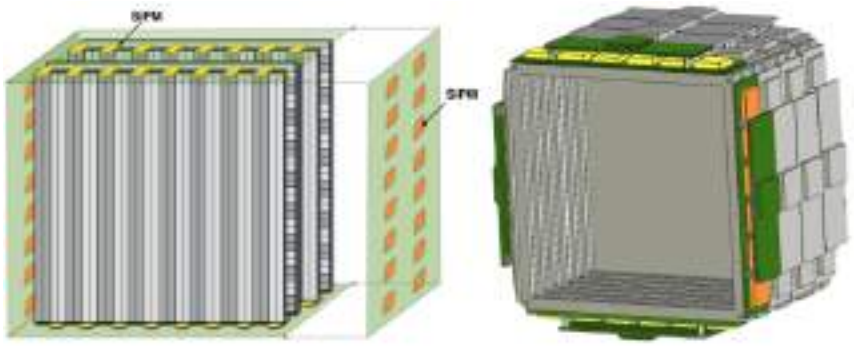

Figure 2.4: Dose Profiler read-out scheme and electronic architecture. Left: schematic view of the fibre read-out via SiPMs, with top and bottom sensor arrays highlighted in yellow and red, respectively. Right: layout of the read-out electronics for the initial bi-plane, displaying the BASICs for the x (yellow) and y (orange) tracking views, alongside the FPGA read-out boards (green). Adapted from [45].

maximise the signal-to-noise ratio. The overall power dissipation estimated under fully operational electronics conditions is ≈ 100 W. Figure 2.4 shows a schematic representation of the DP read-out scheme (left) and electronic architecture (right).

An additional SoC (System-on-Chip) device of the detector electronics is the FPGA-based concentrator board (see Figure 2.5). It provides the trigger signal as well as linking the data collected by the Dose Profiler to the external data-processing and storage units via Ethernet protocol. Its coupling to the DDS enables voxel-specific data recording during the treatment delivery, thereby facilitating *a posteriori* verification and analysis.



Figure 2.5: FPGA board. In yellow the FPGA component is highlighted, whereas the SiPM power supply module are shown in red. Taken from [47].

Two distinct trigger strategies have been implemented within the DP. The stand-alone trigger represents the standard mode utilised during clinical operation, as it combines information from each ASIC to determine whether an event is of interest, whereas the external trigger logic relies on external inputs to activate the read-out boards. The former method requires the time coincidence of over-threshold signals in at least one SiPM in both x and y direction within a bi-plane. Therefore, a valid signal in two bi-plane modules is required to select secondary particles crossing the detector. When a charged fragment satisfies the above-mentioned conditions, the data are sent to the concentrator, where it is temporarily stored during beam in-spill delivery and subsequently sent to the external storage system inter-spill. This system adopts the CNAO beam-time structure to optimise the data transfer efficiency up to a few μs per event.

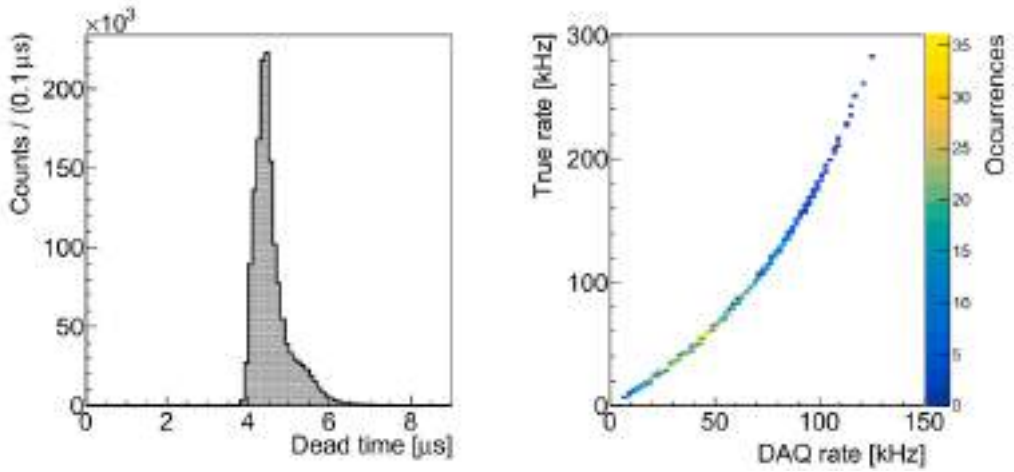

Figure 2.6: Left: dead time per event distribution for a carbon-ion treatment plan on a phantom target. Right: true event rate as a function of the DAQ rate. Source: [46].

2.3.3 Rate Capability and Dead Time

Characterising the detector dead time is crucial to evaluate the sustainable event rate and to guarantee compatibility with clinical conditions, as this parameter measures the time interval the detector requires to process data before enabling further acquisition. In particular, preliminary tests on a phantom target were performed at the CNAO facility prior to the beginning of the clinical trial, to verify stability under high-flux ($\approx 10^8$ ions per spill) environments. The measured reproducibility of the treatment delivery under identical target conditions validated the trigger performance within a 1% variation margin, with measured DAQ rates reaching ≈ 150 kHz (depending on the kinetic energy of the charged fragments impinging on the detector), as shown in Figure 2.6 on the right, and a measured dead time of ≈ 4 μs, reported in Figure 2.6 on the left, in agreement with expectations.

2.4 INSIDE Clinical Trial

The operational performance of the Dose Profiler was evaluated following its installation and commissioning in treatment room 1 at the CNAO facility in July 2019. This milestone marked the onset of the second phase of the INSIDE project, leading to the initiation of the first clinical trial in August 2019, whereas the second part began in November 2024 and ended in July 2026. The study, involving forty CNAO patients (twenty of whom were monitored with the DP) undergoing hadrontherapy for the treatment of meningiomas and head and neck tumours, was designed to assess the sensitivity of the INSIDE system in identifying inter-fractional morphological variations during the treatment's course.

2.4.1 Clinical Workflow

To adopt the INSIDE system (and the Dose Profiler specifically) within the CNAO standard clinical workflow, synchronisation with the patient setup and beam delivery protocols

represent a crucial step. The mobile structure housing the detector is manually aligned by a dedicated operator into the monitoring position (described in Section 2.3.1) the moment patient alignment is finalised. Prior to patient irradiation for a given field (i.e. the primary beam incoming direction), data acquisition is started from the control room by a member of the INSIDE collaboration. Due to the limited freedom in positioning the Dose Profiler caused by its holding structure, some fields cannot be monitored. Moreover, if intra-treatment X-ray verification is performed, the detector has to be temporarily moved and then repositioned, provoking a systematic uncertainty caused by the mechanical reproducibility of cart placement within $\approx 1\,\text{mm}$.

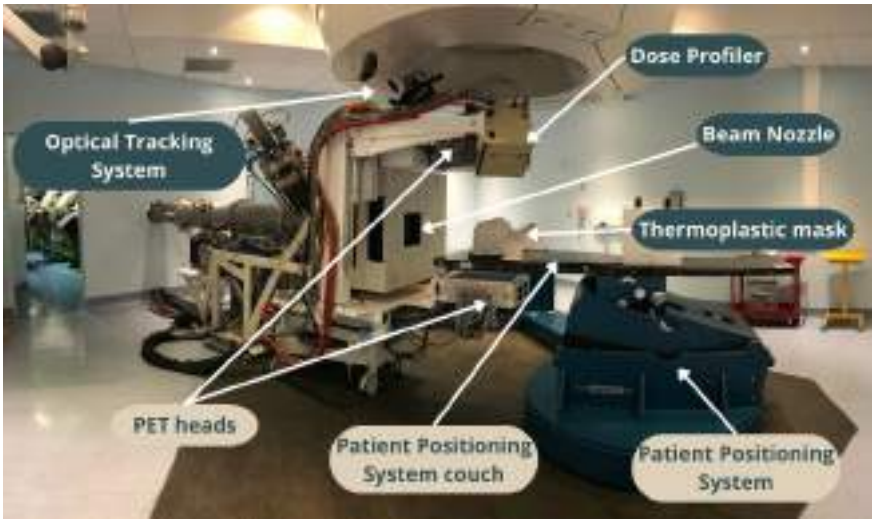

Figure 2.7: View of the INSIDE system installed in treatment room 1 at the CNAO facility. Adapted from [48].

The operational workflow is part of a broader therapeutic framework established during the preliminary treatment planning stage. Based on CT and MRI imaging data acquired with patient-specific immobilisation devices (such as thermoplastic masks), the TPS provides dose distributions according to constraints, as explained in Section 1.3.1. Irradiation typically begins one to two weeks after the TPS simulation, following different fractionation schedules depending on the therapeutic particle employed: carbon-ion treatments are delivered over four fractions per week (up to four weeks), whereas proton treatments last up to seven weeks including five fractions per week.

Patient positioning preceding beam delivery must be thoroughly checked, as rigorous spatial accuracy is a fundamental requirement in hadrontherapy as well as in range monitoring scopes. The positioning system adopted at the CNAO facility consists of the following stages. At first, the Patient Positioning System (PPS), including a carbon-fibre couch moved by a robotic arm, enables the roto-translation of the structure according to the coordinates previously determined by the Treatment Planning System. This enables the irradiation of different fields, where the adopted angular convention establishes that 0° corresponds to the beam impinging on the left side of the patient's head during a clockwise rotation. To limit the patient's mobility, the above-mentioned thermoplastic mask is placed on the treated

district and screwed to the couch. The mask features an Optical Tracking System (OTS) based on three infrared cameras to further check eventual movements occurring during irradiation. Ultimately, X-ray images via Patient Verification System (PVS) are acquired to evaluate positioning displacements by comparison with the CT data employed across treatment planning simulations. The co-registration is performed aligning fixed bone structures until translational and rotational accuracy margins, $\pm 0.3\,\text{mm}$ and 0.1° respectively, are satisfied [49].

Once target alignment is confirmed, the active pencil-beam scanning begins. The technique requires the division in longitudinal direction of the target volume in sections approximately receiving the same dose, the so-called *slices*. Each slice is irradiated, with scanning dipole magnets directing the monochromatic beam to the intended voxels, i.e. volume elements forming a slice. Changing fields via PPS repositioning takes two to three minutes, while beam delivery per each field lasts ≈ 3 minutes. Hence, the majority of the session time is dedicated to immobilisation and positioning verification rather than irradiation.

Figure 2.7 shows the INSIDE setup installed in treatment room 1 at the CNAO facility, with labeled annotations explaining each key element. Situated upstream of the patient, the beam nozzle is the terminal section of the Dose Delivery System. It serves to shape the delivered therapeutic beam, measure beam fluence, and provide real-time monitoring of the beam spatial coordinates and size via integrated ionisation chambers.

2.4.2 Trial Population

The cohort for the INSIDE clinical trial has been selected according to tumour-specific criteria: meningiomas and squamous cell carcinomas of the nasopharynx were selected for protontherapy, whereas adenoid cystic carcinoma (ACC), clival chordomas, and intestinal-type adenocarcinomas (ITAC), i.e. malignant neoplasms of the nasal cavities, were treated with carbon ions. The preference for head and neck tumours was dictated by the negligible tissue mobility compared to thoracic or abdominal areas, where anatomical motion impairs inter-fractional monitoring capabilities. Moreover, the selected case studies are expected to show morphological variations within cranial and sinonasal cavities due to tumour shrinking or treatment-induced mucosal inflammation and mucus accumulation.

A total of forty patients were enrolled in the clinical trial; the first half was treated during the first phase in 2019, while the remaining half was treated during the second phase in 2024. Each phase was equally divided in ten patients receiving protontherapy and ten other patients receiving carbon-ion therapy. Based on the treated pathology clinical histories, only a subset of the cohort was expected to display morphological variations.

When treating superficial neoplasms, a range shifter is placed downstream of the beam nozzle to attenuate the beam energy below the minimum threshold imposed by the synchrotron, thereby obtaining the Bragg peak at shallower depths. It consists of a 3 cm thick plate of tissue-equivalent material placed either on the carbon-fibre couch or at a fixed distance (typically 32 cm) from the primary beam nozzle. However, the energy loss is not the

only effect manifesting when the range shifter is employed, as the interaction between the range shifter and the pencil beam leads to the production of secondary particles that must be taken into account by the treatment planning system.

Chapter 3

Inter-Fractional Monitoring with the Dose Profiler

This chapter presents the data-processing methodology and analytical framework developed for inter-fractional monitoring using the Dose Profiler detector within the INSIDE project. The analysis pipeline encompasses acquired detector signals, three-dimensional secondary fragment emission map reconstruction and quantitative morphological evaluation.

In Section 3.1 the event reconstruction workflow is detailed, starting from pixel clustering algorithms (see Section 3.1.1) designed to mitigate optical cross-talk phenomena in the scintillating fibres. Secondary fragment track identification via the Hough transform is then described in Section 3.1.2, followed by the emission point vertex reconstruction algorithm based on the Point Of Closest Approach (POCA), as detailed in Section 3.1.4. Next, the post-processing and smoothing techniques implemented to generate 3D density distributions are presented.

To assess inter-fractional morphological variations, a three-dimensional gamma index algorithm is introduced in Section 3.2. The mathematical framework, local tolerance parameters, and rigid CT co-registration steps are discussed (see Sections 3.2.1, 3.2.2, and 3.2.3), as well as the performance metrics designed to balance detection sensitivity against statistical noise (see Section 3.2.4). In Section 3.3, computational validation through the FLUKA Monte Carlo simulation code is outlined, thereby defining the baseline required to evaluate the performance limits of the analysis workflow applied in this thesis.

3.1 Emission Point Reconstruction and 3D Emission Maps

The events corresponding to detector hits (see Section 2.3.2) recorded by the DAQ system, are first grouped into clusters prior to track reconstruction, which proceeds according to the data-processing pipeline outlined in the following paragraphs.

3.1.1 Pixel Clustering

As explained in Section 2.3.1, the scintillator fibres selected for the Dose Profiler design adopt a double-cladding technology. Although this choice mitigates the light loss within the fibre, optical cross-talk phenomena can occur: if the scintillation yield generated by a single event exceeds the SiPM read-out threshold, the signal produced by a single fibre might be collected by adjacent ones. Moreover, each SiPM is coupled to two adjacent fibre pairs on opposite boards, as highlighted in Section 2.3.2. The combination of these factors would result in a degradation of the proton emission point estimation.

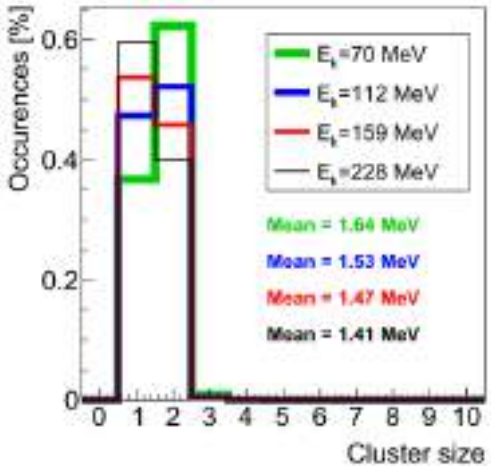

Figure 3.1: Cluster size measurements in self-triggering mode using protons of different kinetic energies at the Trento APSS centre. Reproduced from [46].

Pixel clustering is a required solution to group together spatially adjacent hits, i.e. pixels producing a signal exceeding the threshold. The energy dependence of average cluster size due to cross-talk phenomena was evaluated at the Trento APSS facility, thereby confirming the direct relation between the impinging proton energy (ranging from $\approx$ 45 MeV to $\approx$ 230 MeV) and the measured cluster size ($\approx$ 1.5 pixels per cluster), as shown in Figure 3.1. To reconstruct charged fragment emission points, cluster positions are estimated as the arithmetic average of pixels associated with individual hits [46].

3.1.2 Track Reconstruction

The Hough transform, a widely employed technique in computer graphics processing to detect straight lines in images, is the primary geometrical tool adopted for secondary fragment track reconstruction. The underlying idea behind the transform is to map the search for collinear points in the (x, y) plane onto the (ρ, θ) space, thereby identifying a mathematically-equivalent problem consisting of finding concurrent curves [50].

In the image (x, y) plane a straight line is given by the following equation:

$$x \cos\theta + y \sin\theta = \rho \tag{3.1}$$

where θ is the angle of the normal with respect to the origin and ρ is the distance from the origin (see Figure 3.2, left). Eq. (3.1) is expressed adopting the so-called *normal parametrisation*. By restricting θ to $[0, \pi]$, the parameters identifying an arbitrary line are uniquely determined; therefore, every straight line corresponds to a point in the parameter space.

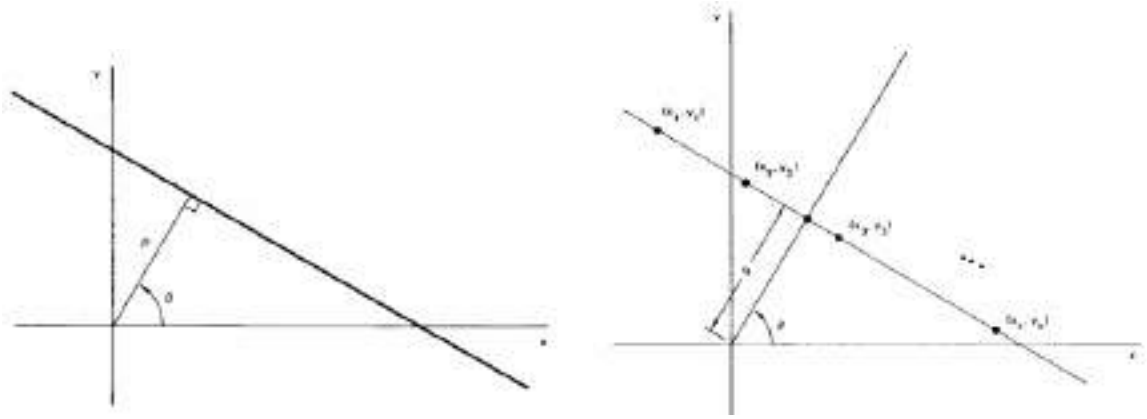

Figure 3.2: Left: normal parameters (ρ, θ) identifying a straight line in the image reference system. Right: collinear points laying on a common straight line in the image plane (x, y). Adapted from [50].

Extending this logic, let us suppose a set of points (x_i, y_i) can be identified in the original image; each one of them is mapped onto the parameter space by the sinusoidal curve:

$$x_i \cos\theta + y_i \sin\theta = \rho(\theta) \tag{3.2}$$

This equation represents the family of all the straight lines passing through the point (x_i, y_i). It can be shown that if multiple points of the original problem share a common line, the corresponding sinusoids intersect at a point (ρ_0, θ_0) uniquely identifying the line parameters (see Figure 3.2, right).

From a computational standpoint, the implementation of the Hough transform relies on partitioning the parameter space into discrete bins, thereby forming a two-dimensional accumulator array. Every reconstructed hit in the image plane votes for all parameter bins corresponding to candidate lines intersecting that point. Thus, bins representing trajectories with a high number of collinear points gather vote peaks, and line identification is translated into a maxima-finding problem in the accumulator matrix, which reveals the most probable track candidates.

The identification of straight lines within clusters revealed by the Dose Profiler relies on applying the Hough transform in the x-z and y-z planes independently, as shown in Figure 3.3. The quality of the parameters, estimated during the tuning phase with both Monte Carlo and acquired data, has been validated through a χ^2-test. Based on a comparative analysis of acquired and simulated data, a minimum of four aligned clusters across both the $x - z$ and $y - z$ projections are required to maximise detection efficiency while minimising

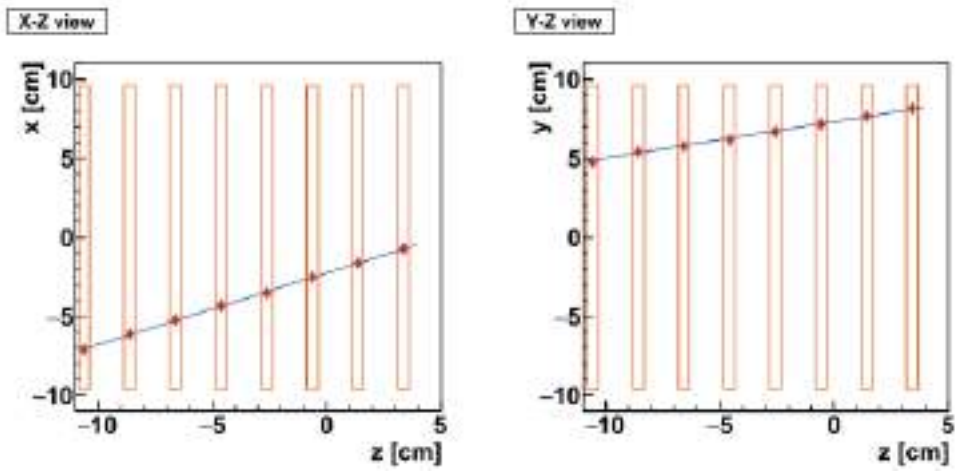

Figure 3.3: Charged fragment tracking within the Dose Profiler. The eight fibre planes are depicted as orange rectangles in the $x-z$ (left) and $y-z$ (right) views. Red markers indicate reconstructed clusters, and the reconstructed track trajectory is shown as a blue line. Taken from [46].

background tracks [46]. The combination of high measured cluster size and small inter-planar spacing results in a negligible contribution from multiple Coulomb scattering within the fibres.

3.1.3 Emission Point Evaluation

Following coordinate transformation into the treatment room reference frame, the track parameters determined via Hough transform, as detailed in the previous section, serve as inputs for back-tracking charged secondary fragments. The estimation of the three-dimensional emission point vertex is derived from the point of closest approach of the reconstructed track with respect to the primary beam axis. The latter is retrieved by combining information from the treatment plan system with real-time data from the dose delivery system, pinpointing the irradiated slices and voxels.

The primary source of uncertainty limiting track reconstruction accuracy stems from multiple Coulomb scattering interactions experienced by charged secondary fragments as they traverse the patient's body. The introduced effect may range from 5 mm to 10 mm depending on various factors such as tissue density and the emission point depth. The tracking spatial resolution, shown in Figure 3.4 was experimentally evaluated employing a 280 MeV/u carbon-ion beam hitting a 4 mm-diameter plastic sphere target placed at distances between 30 mm and 80 mm relative to the Dose Profiler [46]. A spatial resolution of 7 mm is achieved when the detector is positioned 50 cm away from the room isocentre (see Figure 3.2, left).

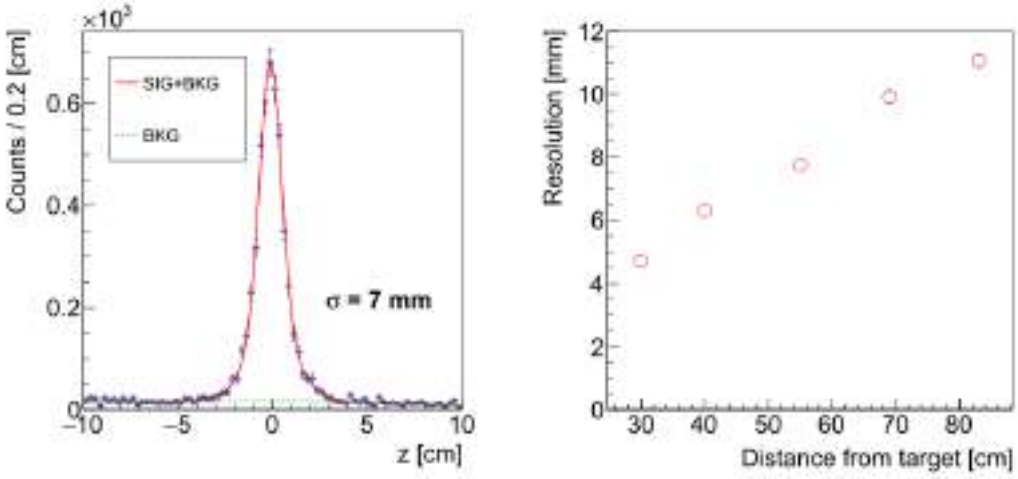

Figure 3.4: Spatial resolution performance of the Dose Profiler evaluated with a 280 MeV/u carbon-ion beam. The reconstructed z-coordinate distribution along the beam line for a target distance of 50 cm is shown on the left, while the overall spatial resolution as a function of target-to-detector distance is reported on the right. Source: [46].

3.1.4 3D Emission Maps Reconstruction

Prior to three-dimensional emission map generation, the first operational phase consists of processing the raw data acquired by the Dose Profiler to reconstruct the one-dimensional POCA spatial distributions stored in ROOT [51] files.

Direct co-registration of the fragment emission maps with the anatomical CT images, derived from clinical DICOM [52] (Digital Imaging and Communications in Medicine) files via conversion to the MetaImage .mhd format, is achieved by mapping the reconstructed POCA coordinates from the global reference frame into the patient CT coordinate system using the geometry transformation file relative to the specific irradiation field.

The resulting POCA density emission map is defined on a 3D voxel grid sharing the same dimension, origin, and voxel spacing with the input CT, where each accepted POCA spatial position increments the corresponding voxel count, forming a raw density map of the charged secondary fragment emission points. An example of a three-dimensional POCA emission map for the Monte Carlo simulation of a patient, identified by ID number 6, superimposed on the patient's CT is provided by Figure 3.5. This case study will be further analysed in Section 4.1.

MCS effects within the patient are further mitigated in the back-tracking process through a geometrical selection criterion based on the Distance Of Closest Approach (DOCA) between the track and the pencil-beam trajectory that has been implemented into the most recently developed pipeline. Tracks exceeding a distance of closest approach of DOCA > 1 cm are discarded to limit multiple scattering degradation contributions to the reconstructed emission map.

Map generation is followed by a two-stage post-processing sequence. First, a hotspot-cleaning method is applied to remove isolated, non-physical emission density artefacts from

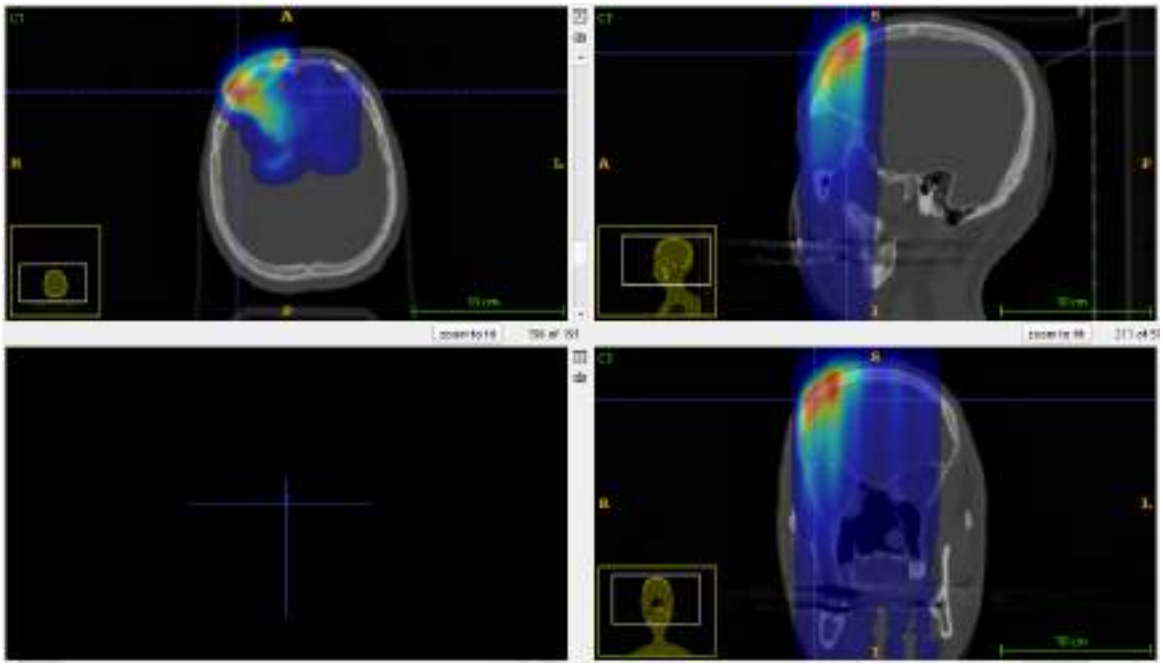

Figure 3.5: Reconstructed three-dimensional POCA emission maps from the simulation of patient 6 of the CNAO clinical trial based on and overlapped on the planning CT, visualised via ITK-SNAP [53, 54].

the reconstructed distributions. Each voxel value is compared against the average of its $3 \times 3 \times 3$ voxel neighborhood, and if a voxel exceeds the local mean by a factor of greater of 5, it is replaced by the mean value itself. This threshold factor was adopted from the existing analysis pipeline without further verification in this thesis. The second step aims to suppress statistical noise and account for the detector's intrinsic spatial resolution by applying a smearing algorithm. The final voxel content is then computed as the arithmetic mean over its neighboring points within a $7 \times 7 \times 7$ voxel volume. The selection was investigated in this thesis, and the adopted choice yields an optimal trade-off between spatial detail and noise attenuation for downstream evaluations.

3.2 Gamma Index Test

Inter-fractional tissue variations occurring throughout the treatment are investigated through a gamma index analysis, conducted by comparing the spatial emission maps reconstructed across different treatment fractions. Widely adopted for dosimetric verification and to assess agreement between dose distributions [55], the gamma index is here employed to evaluate the concordance between three-dimensional POCA density distributions. Specifically, the algorithm receives a reference map and an evaluation map, assigned according to the chronological sequence of data acquisition, alongside tolerance criteria discussed in Section 3.2.2. Within this framework, morphological variations inside the patient manifest as voxel discrepancies in the test output.

3.2.1 Gamma Index Definition

In the literature, the gamma index is formally defined as a dimensionless metric obtained by the simultaneous combination of dose difference and distance displacement evaluated on a voxel-by-voxel basis across the compared distributions [56]. In this work the gamma index is defined as follows:

$$\Gamma(\mathbf{r}_\mathrm{e}, \mathbf{r}_\mathrm{r}) = \sqrt{\frac{|\mathbf{r}_\mathrm{e} - \mathbf{r}_\mathrm{r}|^2}{r^2} + \frac{|D_\mathrm{e}(\mathbf{r}_\mathrm{e}) - D_\mathrm{r}(\mathbf{r}_\mathrm{r})|^2}{D^2}} \tag{3.3}$$

where:

- $\mathbf{r}_\mathrm{e}$, $\mathbf{r}_\mathrm{r}$ indicate a specific voxel belonging to the evaluation and reference map, respectively;
- $D_\mathrm{e}(\mathbf{r}_\mathrm{e})$, $D_\mathrm{r}(\mathbf{r}_\mathrm{r})$ represent the emission densities evaluated at positions $\mathbf{r}_\mathrm{e}$ and $\mathbf{r}_\mathrm{r}$, respectively;
- r, D stand for displacement and density tolerance parameters.

A one dimensional schematic representation of the gamma index test is displayed in Figure 3.6.

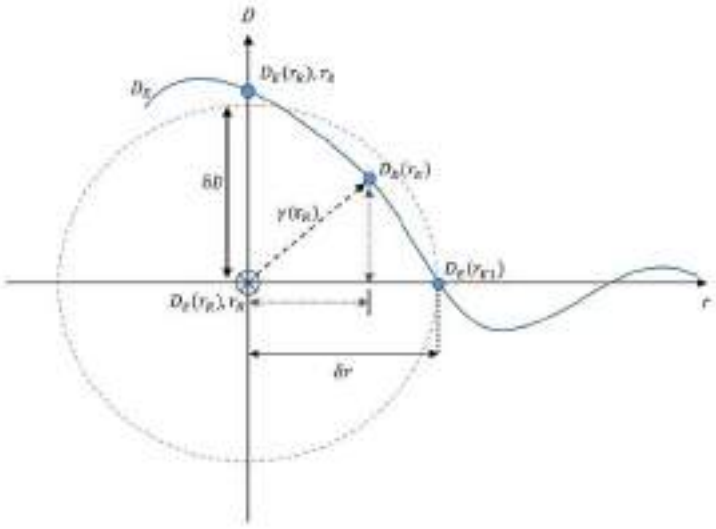

Figure 3.6: One-dimensional geometric schematic representation of the gamma index test. The evaluated voxel position and emission density is marked by the cross at the axis origin. The horizontal axis shows the spatial distance to sampled reference voxels, whereas the vertical one displays the corresponding emission density difference. The acceptance ellipse is defined by the tolerance parameters (r, D), and the test is passed ($\gamma \leq 1$) if the candidate points lying on the blue curve enter the tolerance ellipse. Image from [55].

From a computational standpoint, the analysis is executed through two nested loops: the outer loop iterates over each reference voxel $\mathbf{r}_{\mathrm{r,i}}$, whereas the inner one evaluates the gamma function $\Gamma(\mathbf{r}_{\mathrm{e,j}}, \mathbf{r}_{\mathrm{r,i}})$ across all points $\mathbf{r}_{\mathrm{e,j}}$ in the evaluation map. The definitive gamma

index value associated with each reference voxel $\mathbf{r}_{\mathrm{r,i}}$ is established by minimising the gamma function across the evaluation distribution:

$$\gamma(\mathbf{r}_{\mathrm{r}}) = \min_{\mathbf{r}_{\mathrm{e}}} \{\Gamma(\mathbf{r}_{\mathrm{e}}, \mathbf{r}_{\mathrm{r}})\} \tag{3.4}$$

The outcome of the test strictly depends on this value: $\gamma(\mathbf{r}_{\mathrm{r}}) > 1$ indicates a significant tissue density variation according to the tolerance thresholds set by r and D.

Moreover, r represents the distance-to-agreement criterion, defining the radius of a search sphere centred at the reference voxel $\mathbf{r}_{\mathrm{r}}$ that encompasses nearby candidate points $\mathbf{r}_{\mathrm{e}}$ belonging to the evaluation map. Its inclusion in the gamma index calculation via the term $\frac{|\mathbf{r}_{\mathrm{e}}-\mathbf{r}_{\mathrm{r}}|^2}{r^2}$ highlights that expanding the search volume with a larger acceptance threshold r increases the probability of finding at least one evaluated voxel that satisfies the passing condition $\Gamma(\mathbf{r}_{\mathrm{e}}, \mathbf{r}_{\mathrm{r}}) \leq 1$. Similarly, D sets the emission density tolerance parameter, against which the absolute difference $|D_{\mathrm{e}}(\mathbf{r}_{\mathrm{e}}) - D_{\mathrm{r}}(\mathbf{r}_{\mathrm{r}})|$ between corresponding voxels of the evaluation and reference distributions is compared. The test fails when this absolute difference exceeds D for all candidate voxels within the search volume. Consequently, increasing D renders the gamma index more permissive, allowing a larger number of voxels to satisfy the passing condition.

In Figure 3.7, the gamma index map is shown with two visualisation modalities: the *passrate mode* (Figure 3.7, top), which generates a binary map assigning a value of 0 to voxels that pass the test (displayed in red), and 1 to those that fail (visualised in green) and the *gamma mode* (see Figure 3.7, bottom), which assigns the exact gamma value to each voxel. Although the *gamma mode* provides valuable magnitude information, only passrate maps are presented in this work. This choice is motivated by the lower computational cost and the more immediate visual readability offered by the binary representation.

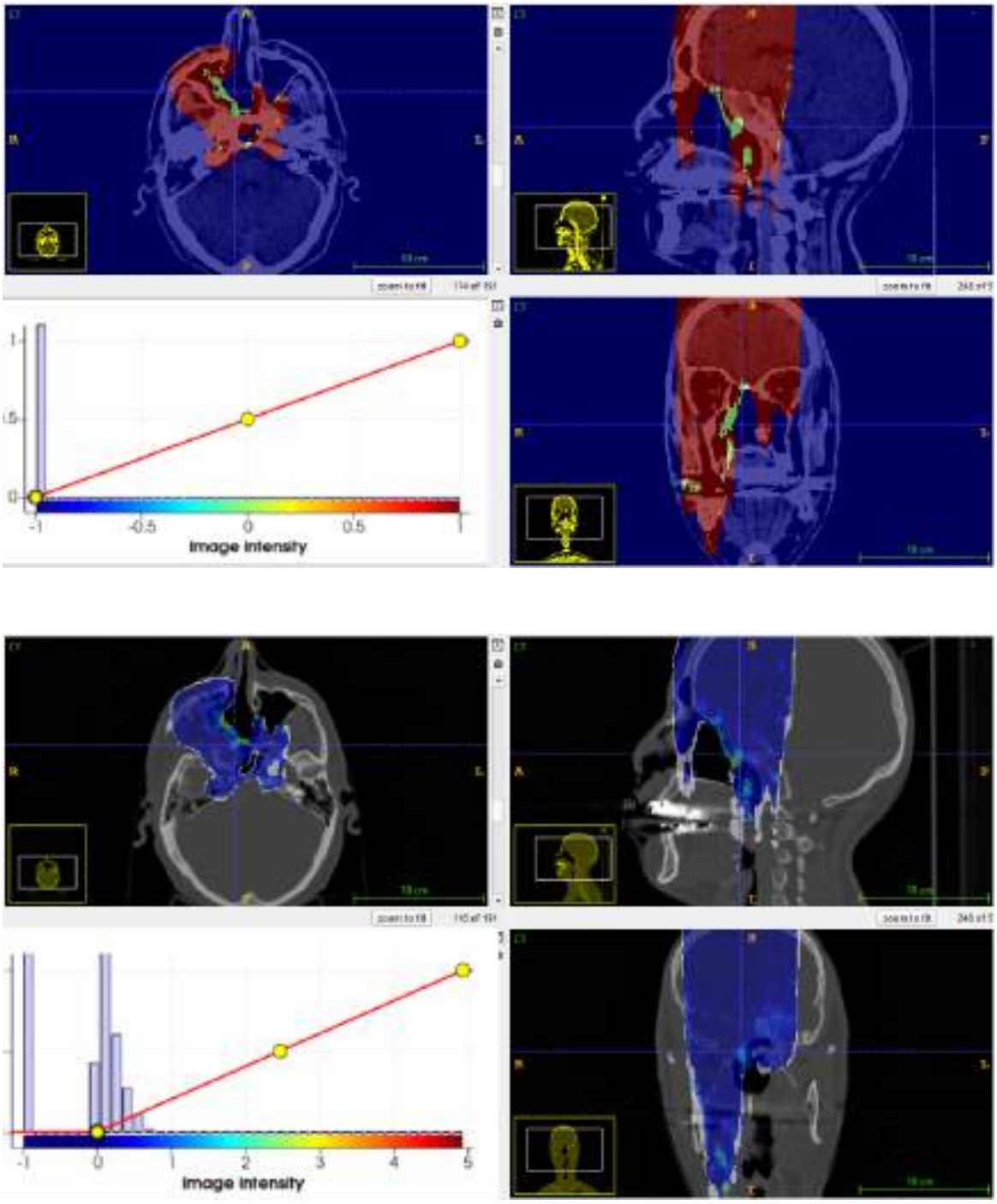

Figure 3.7: Gamma index map for patient 6 evaluated against the Monte Carlo simulation dataset, overlaid on the planning CT. Top: map shown in passrate mode, where passing voxels ($\gamma \leq 1$) are highlighted in red, failing voxels ($\gamma > 1$) in green, and non-evaluated voxels in blue. Bottom: corresponding gamma index distribution visualised in gamma mode, where only evaluated voxels are displayed.

3.2.2 Tolerance Parameters

As briefly mentioned in the introduction to Chapter 3, the implemented gamma index code depends on three tolerance criteria:

- Emission Density Difference (DD) [%]: corresponds to the D parameter described in Section 3.2.1; it is defined as percentage of the maximum emission density value in the reference map, defining the allowed emission density discrepancy between the reference and evaluation distributions. Classically, the global normalisation is defined as:

$$\mathrm{DD}_{\mathrm{global}} = \frac{D}{D_{\mathrm{r,max}}} \times 100\% \tag{3.5}$$

  A recently implemented revised definition [57] has been adopted in this work to account for local voxel intensity, thereby measuring the relative variation between the two emission density maps instead of an absolute global difference:

$$\mathrm{DD}_{\mathrm{local}} = \frac{D}{D_{\mathrm{r}}(\mathbf{r}_{\mathrm{r}})} \times 100\% \tag{3.6}$$

  The main advantage offered by the local approach over the global one resides in its enhanced sensitivity to relative discrepancies within profound, low-density regions, where global criteria often fail to detect clinically relevant variations. Therefore, an overall improvement in the detection of subtle tissue changes is achieved at the expense of a strict metric interpretation of the gamma index, as the emission density difference no longer represents a fixed distance measure but rather depends on the local value of the reference distribution;

- Distance-To-Agreement (DTA) [mm]: corresponds to the r parameter defined in Section 3.2.1;

- Density THreshold (DTH) [%]: restricts the evaluation to voxels with dose above this value with respect to the reference map maximum dose, thereby suppressing statistical noise.

The combination of these parameters establishes the strictness of the gamma index test. In this study, specific sets of DD, DTA and DTH values were selected to evaluate inter-fractional variations, balancing detection sensitivity against spurious signal. The visual and quantitative impacts of these configuration choices on the resulting passrate distributions will be detailed in Chapter 4.

3.2.3 Hounsfield Units Maps

As briefly introduced in Section 3.1.4, a crucial phase in the data analysis pipeline relies on the co-registration of the CT images corresponding to the compared treatment fractions, especially in the Monte Carlo simulation analysis. Due to variations in patient positioning

across acquisition dates, a perfect overlap between the two CT scans cannot be achieved directly. Therefore, manual rigid co-registration was performed using the ITK-SNAP Image Registration tool to determine the roto-translation transformation matrix (with six degrees of freedom) mapping the evaluation CT onto the reference CT geometrical frame. However, because this approach relies heavily on visual inspection, operator sensitivity to distinguish subtle anatomical displacements, and minor posture differences adopted by the patient (e.g. neck tilt), this time-consuming procedure presents intrinsic uncertainties and requires further investigation and automation, which was not carried out in this work.

The POCA distributions, and consequently the gamma index outcome, are mapped onto the reference CT coordinate system. The evaluation CT is used to create the ΔHU map defined as the voxel-wise difference between the two CT acquisitions $|\mathrm{HU_{ref}} - \mathrm{HU_{eval}}|$. Figure 3.8 provides an example of a ΔHU map for patient 6 evaluated against the Monte Carlo simulation dataset and overlaid on the planning CT. A threshold value equal to thr = 500 has been adopted to reduce the visualisation of uncoregistered voxels and to enhance robustness of the analysis.

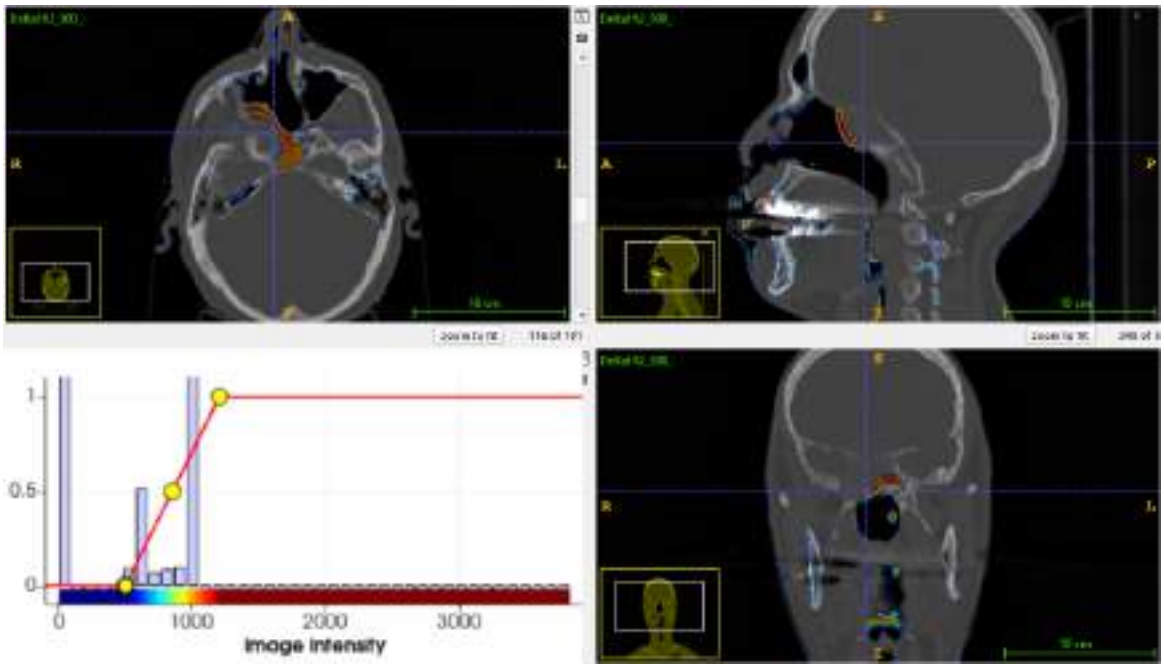

Figure 3.8: Hounsfield Units difference map for patient 6 evaluated against the Monte Carlo simulation dataset, overlaid on the planning CT, showing voxels with $|\mathrm{HU_{ref}} - \mathrm{HU_{eval}}| > 500$.

The ΔHU map aims to display the possible anatomical changes that occurred within the patient over the course of treatment, and it is here employed alongside the gamma index map to assess the detector's sensitivity in highlighting morphological variations under proper parameter optimisation, as detailed in the following section.

3.2.4 Parameter Optimisation

The optimisation of the DD, DTA, and DTH parameters is essential to enable a clear and reliable visualisation of morphological variations occurring within the patient's body via constructed gamma index maps. The tuning process is supported by the introduction of two fundamental metrics: efficiency and purity.

The *efficiency* (ε) is defined as:

$$\varepsilon = \frac{\text{number of voxels with } \gamma > 1 \text{ and } \Delta\text{HU} > thr}{\text{number of voxels with } \Delta\text{HU} > thr} \tag{3.7}$$

where the numerator denotes the count of voxels simultaneously satisfying $\gamma > 1$ and exhibiting a Hounsfield Unit difference ΔHU between the two CT scans that exceeds the specified threshold; the denominator consists of all voxels whose ΔHU exceeds that same threshold. The efficiency measures the fraction of truly discrepant voxels correctly detected by the gamma index.

Purity (δ) reads:

$$\delta = \frac{\text{number of voxels with } \gamma > 1 \text{ and } \Delta\text{HU} > thr}{\text{number of voxels with } \gamma > 1} \tag{3.8}$$

Sharing both the numerator and value range with the efficiency metric, purity indicates the proportion of gamma-failing voxels that are truly driven by anatomical changes, thereby measuring the test's purity.

These two metrics have been analysed in previous studies [58]. The results demonstrate that while gamma index maps obtained by maximising efficiency alone are vulnerable to statistical noise, enhancing purity at the expense of efficiency yields overly selective maps that lack sensitivity to subtle variations. These considerations highlight the need to balance the weight assigned to each metric, thereby achieving a reliable trade-off between noise robustness and sensitivity to clinically relevant anatomical variations.

To further expand the information extracted from the gamma analysis, three additional criteria were integrated alongside the aforementioned metrics. However, their full potential remains to be fully explored in future studies, as the current work exclusively relies on purity and efficiency for the optimisation of DTA and DD parameters. Nonetheless, the values for these additional metrics will be reported in the analysis presented in Chapter 4.

The *error* (η) is defined as:

$$\eta = \frac{\text{number of voxels with } \gamma < 1 \text{ and } \Delta\text{HU} > thr}{\text{number of voxels with } \gamma < 1} \tag{3.9}$$

It quantifies the proportion of voxels where a true anatomical variation, exceeding the Hounsfield Unit difference threshold, is incorrectly classified as non-discrepant by the gamma index test.

The *false positive rate* (ρ) reads:

$$\rho = \frac{\text{number of voxels with } \gamma > 1 \text{ and } \Delta\text{HU} < thr}{\text{number of voxels with } \Delta\text{HU} < thr} \tag{3.10}$$

As the name itself suggests, false positives represent the fraction of voxels incorrectly flagged as discrepant by the gamma evaluation despite exhibiting no morphological variation in the Hounsfield Units difference map.

This parameter accounts for the proportion of true morphological variations that are overlooked by the gamma index test.

All the metrics defined above ($\varepsilon, \delta, \eta, \rho$) range from a minimum value 0 to a maximum of 1, where the physical meaning of values approaching either extreme of the domain depends on whether the parameters measure test accuracy or error rates.

3.3 Validation via Monte Carlo Simulation

To evaluate the accuracy of the range verification methodology and quantify the sensitivity of the analysis pipeline, Monte Carlo simulations were performed alongside patient data analysis. Contrary to experimental datasets, Monte Carlo simulations provide outcomes devoid of clinical setup uncertainties. In this work, simulations were conducted using the FLUKA code to compare the reconstructed POCA distributions against known anatomical variations. This computational validation establishes the baseline for the gamma index performance metrics.

3.3.1 FLUKA Code

FLUKA (*FLUktuierende KAskade*) is a fully integrated Monte Carlo code employed in several fields, including medical physics, cosmic ray studies, shielding, dosimetry, radiation protection, detector simulations, and more [59–62]. This FORTRAN software, developed through the collaboration between CERN (Conseil Européen pour la Recherche Nucléaire) and INFN (Istituto Nazionale di Fisica Nucleare), is mainly used to simulate the transport of over sixty types of particles and their interactions with matter. Furthermore, photons and electrons with energy ranging from 1 keV to thousands of TeV, and hadrons with energy up to 20 TeV can be accurately modelled. Figure 3.9 provides a schematic representation of the implemented electromagnetic interactions.

In the FLUKA framework, spatial setup modelling relies on basic geometric *bodies* (i.e. spheres and parallelepipeds), which are combined to build complex *regions*. Every region possesses a unique identifier and is linked to a specific material or chemical composition. Monte Carlo tracking is structured into *events*, where each event corresponds to the life cycle of an individual primary beam particle. This includes its initial generation, its propagation through the setup, and all subsequent interactions, along with the transport of secondary fragments through the experimental setup. The primary mechanism for recording charged

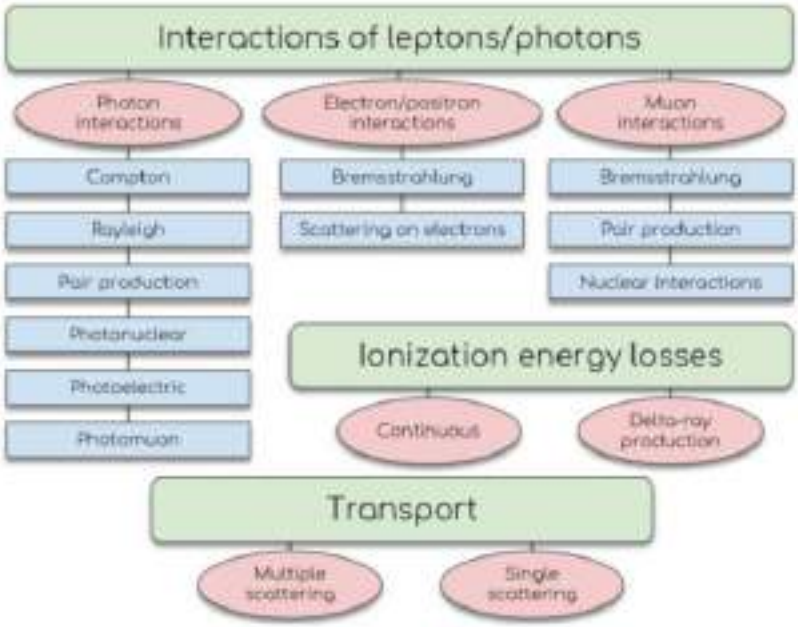

Figure 3.9: Schematic representation of the electromagnetic interactions implemented in FLUKA code [63].

particle transport is the *hit*, defined as the energy loss occurring over a step within a sample volume, it corresponds here to the individual scintillating fibres.

3.3.2 Patient Simulation

The CNAO experimental setup, including the accelerator nozzle and detector geometries, was visualised and managed within FLAIR (FLUKA Advanced Interface) [64] as depicted in Figure 3.10. FLUKA enables the comprehensive simulation of a treatment plan by taking into account both the clinical environment (including the DP detector) and patient-specific data such as the DICOM CT files and beam delivery specifics. The latter are converted through a built-in stoichiometric calibration from Hounsfield Units to tissue density, while information regarding the energy, position and particle fluence per pencil beam are retrieved from the facility's Dose Delivery System.

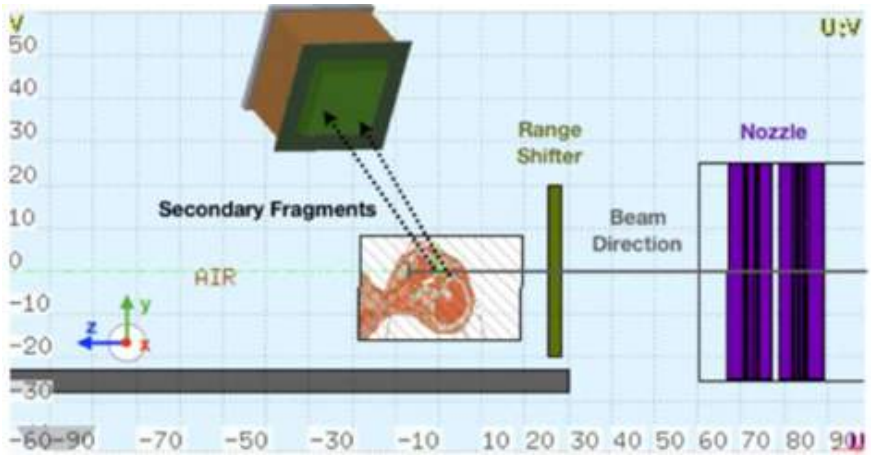

Figure 3.10: Cross-sectional view in the $y-z$ plane of the CNAO clinical setup implemented in FLUKA, showing the patient CT, the Dose Profiler (green and brown structure placed above the patient), the Range Shifter (green), and the nozzle (violet and black) delivering the primary ion beam (coming along the z axis from right to left direction). Adapted from [65].

The analysis of the simulated data mirrors the procedure established for the experimental datasets. The processing begins from the ROOT output file provided by FLUKA, POCA distributions are subsequently constructed according to the methodology outlined in Section 3.1.4 and compared through the gamma index algorithm to assess morphological variations, according to Section 3.2.

Chapter 4

Results of Patient Data Analysis

This chapter presents the results of the patient data analysis following the pipeline outlined in Chapter 3, comparing the simulations performed with the FLUKA Monte Carlo code (as described in Section 3.3.2) against the experimental data acquired with the Dose Profiler detector described in Chapter 2. Specifically, patient 6 from the first cohort of the clinical trial, alongside patients 15 and 18 from the second part of the trial, were selected for this study. First, the patients' CTs were reconstructed from DICOM files, manually co-registered, and used to generate the ΔHU map to highlight potential anatomical changes (see Section 3.2.3). Geometry reconstruction files for each irradiated field were then generated to build the three-dimensional POCA distributions for each treatment fraction. These distributions were initially compared by generating voxel-wise difference and relative percentage difference maps, and then using the gamma index test (described in Section 3.2), which was evaluated over a specific region defined by a voxel mask that excludes voxels receiving dose values below a selected threshold. Finally, the ε and δ parameters defined in Section 3.2.4 were evaluated within a rectangular Region of Interest (ROI) surrounding the possible anatomical change, and plotted to determine the optimal triplet of DD, DTA, and DTH values that maximises the visualisation of potential morphological variations in the gamma index maps.

Table 4.1 shows a general overview of the three patients analysed in the present thesis.

ID	**Pathology**	**#fractions**	**Dose[Gy(E)]**	**Re-evaluation CT**	**Replanned**
6	ITAC	16	65.6	7th fraction	yes
15	clivus chondrosarcoma	15	45	15th fraction	no
18	MMM	9	41	4th fraction	yes

Table 4.1: General overview for the patients enrolled in the CNAO clinical trial and analysed in this thesis.

4.1 Patient 6

Patient 6 was diagnosed with intestinal-type adenocarcinoma (ITAC), the second most frequent type of sinonasal adenocarcinoma [66]. The prescribed carbon-ion treatment plan comprised sixteen fractions, delivering a total dose equal to 65.6 Gy(E) (see Table 4.1). Table 4.2 shows the irradiation fields and the number of primary particles.

Field	Irradiation angle (°)	Number of Primary Particles
B1	**15**	$\mathbf{7.41 \times 10^8}$
B2	195	7.15×10^8
B3	**270**	$\mathbf{5.98 \times 10^8}$

Table 4.2: Patient 6 parameters of the irradiation fields prescribed in the treatment plan.

Although experimental data were acquired with the DP for both the B1 and the B3 fields (highlighted in bold in Table 4.2), only the B3 data was analysed in this thesis.

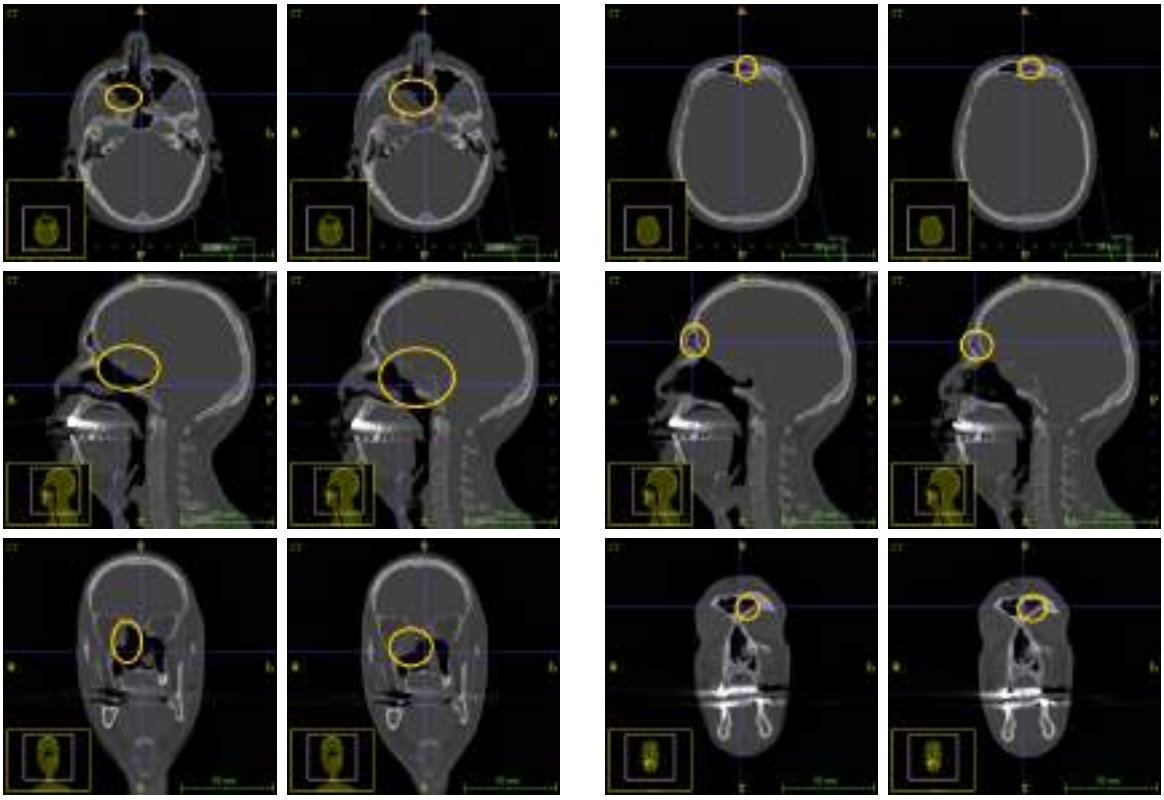

(a) (b)

Figure 4.1: Comparison between the planning CT (left column: transverse, sagittal, and coronal views) against the control CT (right column: transverse, sagittal, and coronal views), displaying two distinct anatomical variations (a) and (b) circled in yellow.

The planning CT was acquired approximately twenty days prior to the beginning of treatment (06/11/2019), and a second CT scan was scheduled on the day of the seventh fraction (13/11/2019). Since morphological variations were detected (see the areas high-

lighted within the yellow circles in Figures 4.1a and 4.1b), the latter was employed to re-plan the treatment; however, this study focuses exclusively on the data collected during the first part of the treatment plan.

The ΔHU map enables a clearer visualisation of the anatomical variations occurred within the patient: the turquoise areas in Figure 4.2 highlight voxels exhibiting a Hounsfield Units difference greater than 500 HU between the planning and the control CT scans. As detailed in Section 3.2.3, a co-registration uncertainty margin due to the slightly different patient positioning during the scan is reflected in Figure 4.2 by the sparse turquoise voxels visible around the patient's head contour and oral cavity in the sagittal and coronal views.

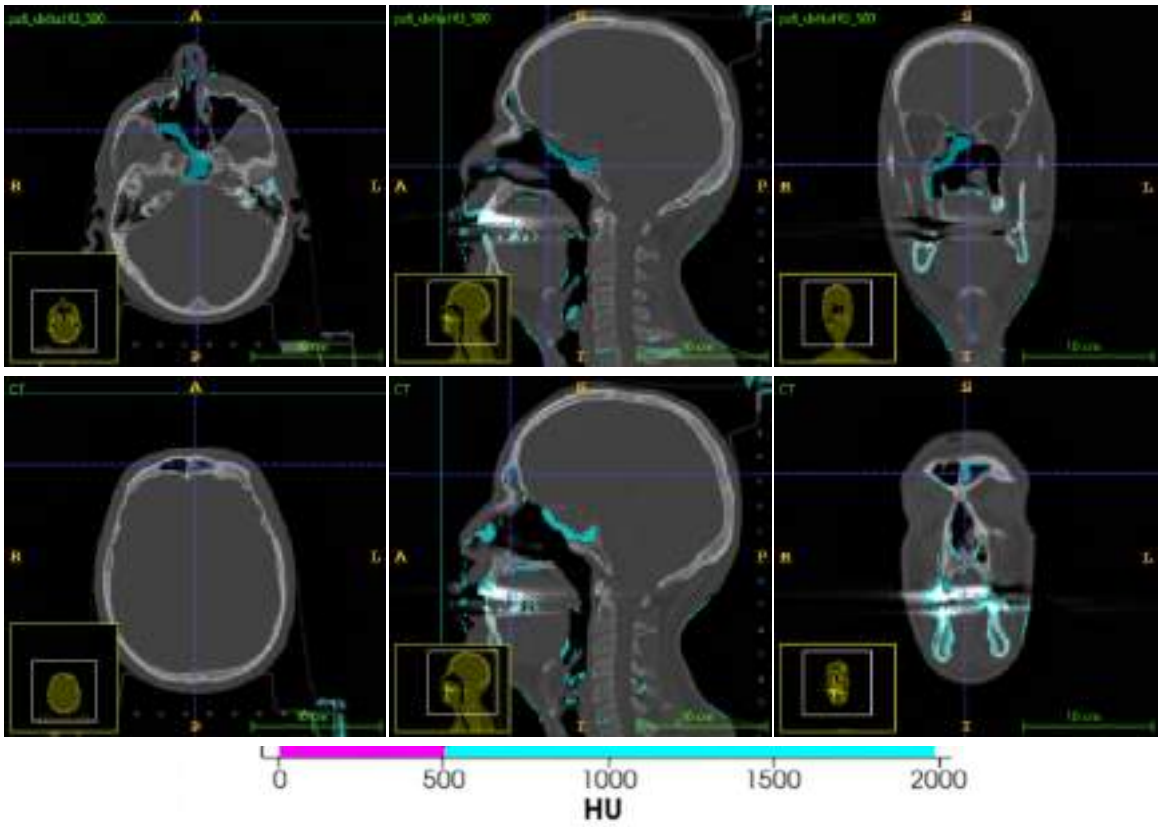

Figure 4.2: Patient 6 ΔHU > 500 map between the planning and control CT scans visualised superimposed on the former. Top row and bottom row turquoise areas display anatomical variations occurred within the first part of the treatment plan (see Figure 4.1).

Figure 4.3 shows the prescribed dose distribution (RTdose) overlaid on the planning CT. The coronal view (see Figure 4.3, right) clearly highlights the beam entry directions for the B1 (15°), B2 (195°), and B3 (270°) irradiation fields. A comparison between the reconstructed POCA distributions obtained from the experimental dataset and the Monte Carlo reconstruction for both the first and seventh treatment fractions reveals a spatial displacement in the experimental reconstruction (Figure 4.4). Specifically, Figures 4.4a and 4.4b compare the same corresponding slice across the transverse, sagittal, and coronal views for the experimental POCA distribution (left column) against the MC simulation

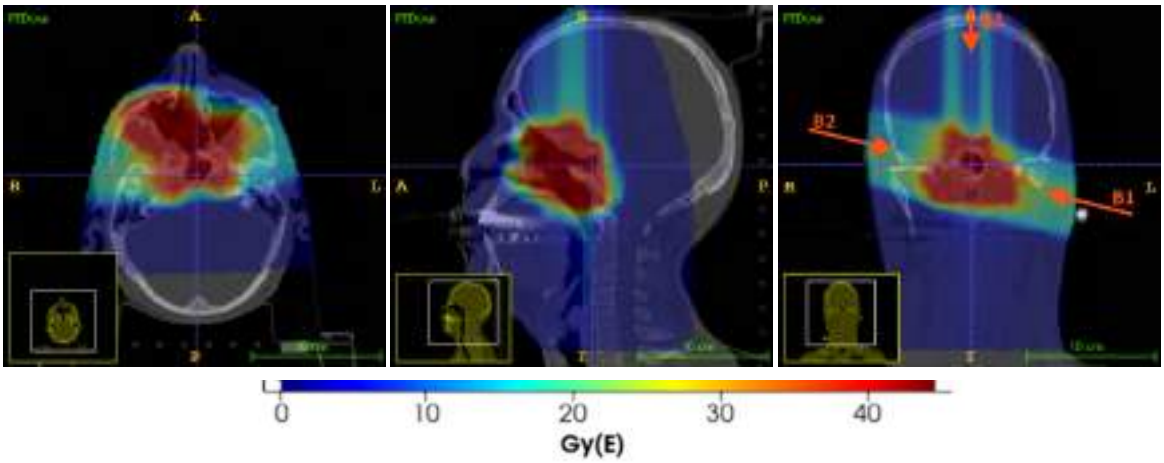

Figure 4.3: Prescribed dose distribution for patient 6 for the B1, B2, and B3 irradiation fields overlaid on the planning CT. The delivered dose is displayed using a colour gradient map ranging from blue (low-dose regions), to red (high-dose regions).

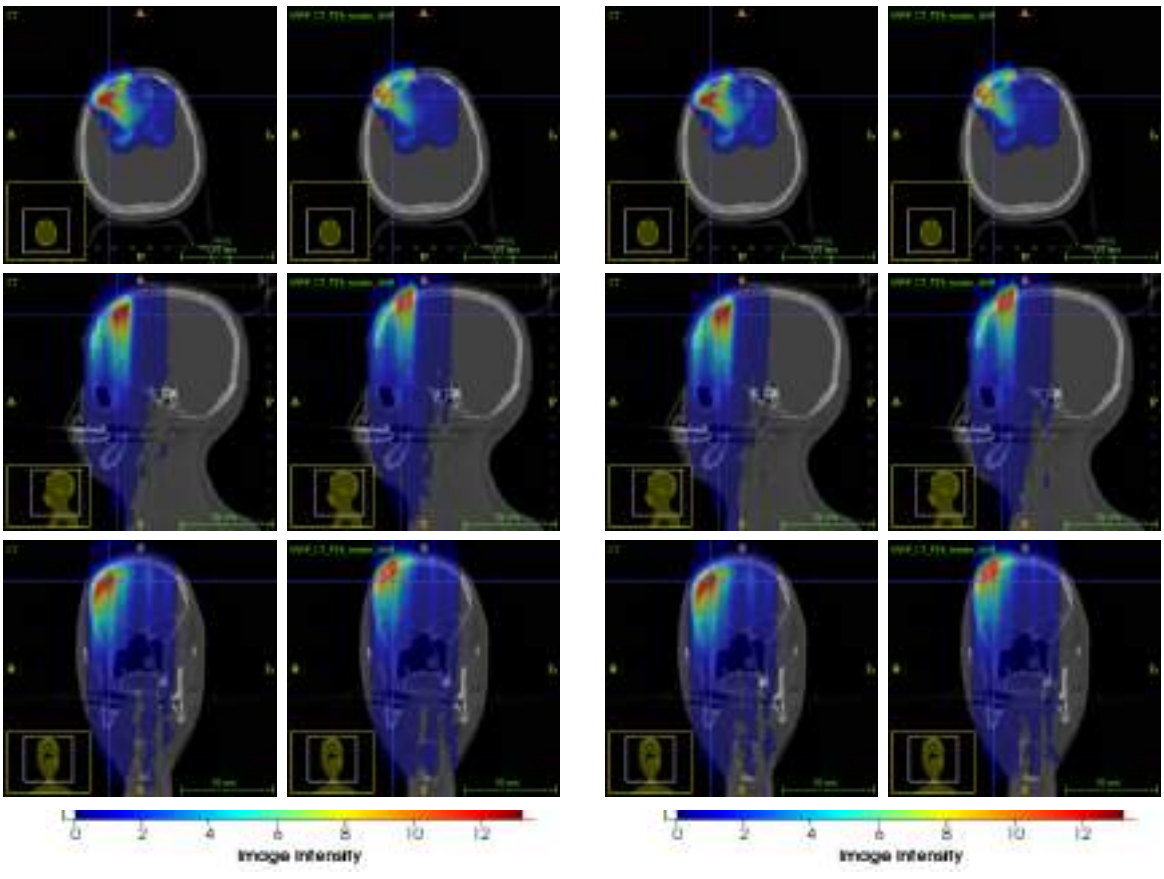

(a) (b)

Figure 4.4: Comparison between the same slice across the transverse, sagittal, and coronal views of the experimental POCA distribution (left column) against the Monte Carlo simulation (right column) for the first (a) and seventh (b) fractions. The image intensity colour scale is normalised to the experimental distributions.

(right column) for the first and seventh treatment fractions, respectively. Quantitatively, the maximum emission densities for the experimental reconstruction and MC simulation are 13.207 and 16.496 in the first fraction, compared to 13.140 and 16.329 in the seventh fraction. The POCA density emission is displayed using a colour gradient map ranging from blue (low-density regions), to red (high-density regions). Although the gamma index

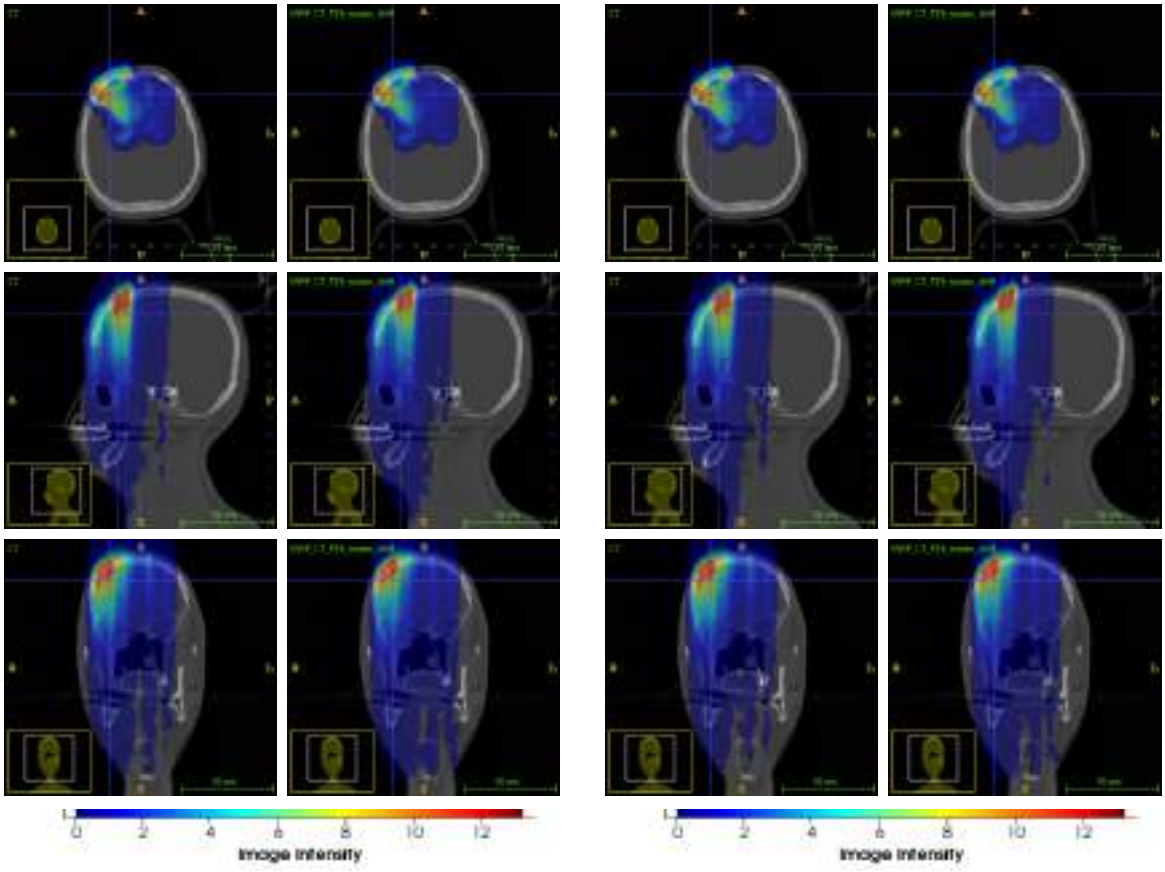

(a) (b)

Figure 4.5: Comparison between the same slice across the transverse, sagittal, and coronal views of the co-registered experimental POCA distribution (left column) against the MC simulation (right column) for the first (a) and seventh (b) fractions. The image intensity colour scale is normalised to the experimental distributions.

test could still be performed because both experimental POCA distributions exhibited the same systematic spatial displacement relative to the Monte Carlo simulated data and similar emission density maxima, these maps were co-registered with respect to the MC simulations prior to gamma index evaluation. The experimental POCA map from the first fraction was manually co-registered to its corresponding Monte Carlo simulation, and the experimental distribution from the seventh fraction was co-registered to the newly aligned first-fraction experimental map. This step introduced a smearing factor due to the linear interpolation required during co-registration to prevent voxel edge artefacts. An overall reduction in the emission density peak was observed, decreasing from 13.207 to 12.938 and from 13.140 to 12.490 for the first and seventh fractions, respectively. Figure 4.5 extends the comparison

presented in Figure 4.4 to the co-registered experimental POCA distributions.

Figures 4.6 and 4.7 display two additional maps that were generated from the POCA distributions. The top row represents the voxel-wise difference between the first and last fraction POCA distributions, defined as $\text{map}_1[i] - \text{map}_2[i]$ (where the index i indicates the i-th voxel). Therefore, blue areas (negative values) denote a density increment corresponding to anatomical filling, whereas red regions (positive values) indicate decreased density over time corresponding to anatomical emptying. The second map (bottom row) represents the relative percentage difference, evaluated as $|\text{map}_1[i] - \text{map}_2[i]|/\text{map}_1[i] \times 100$.

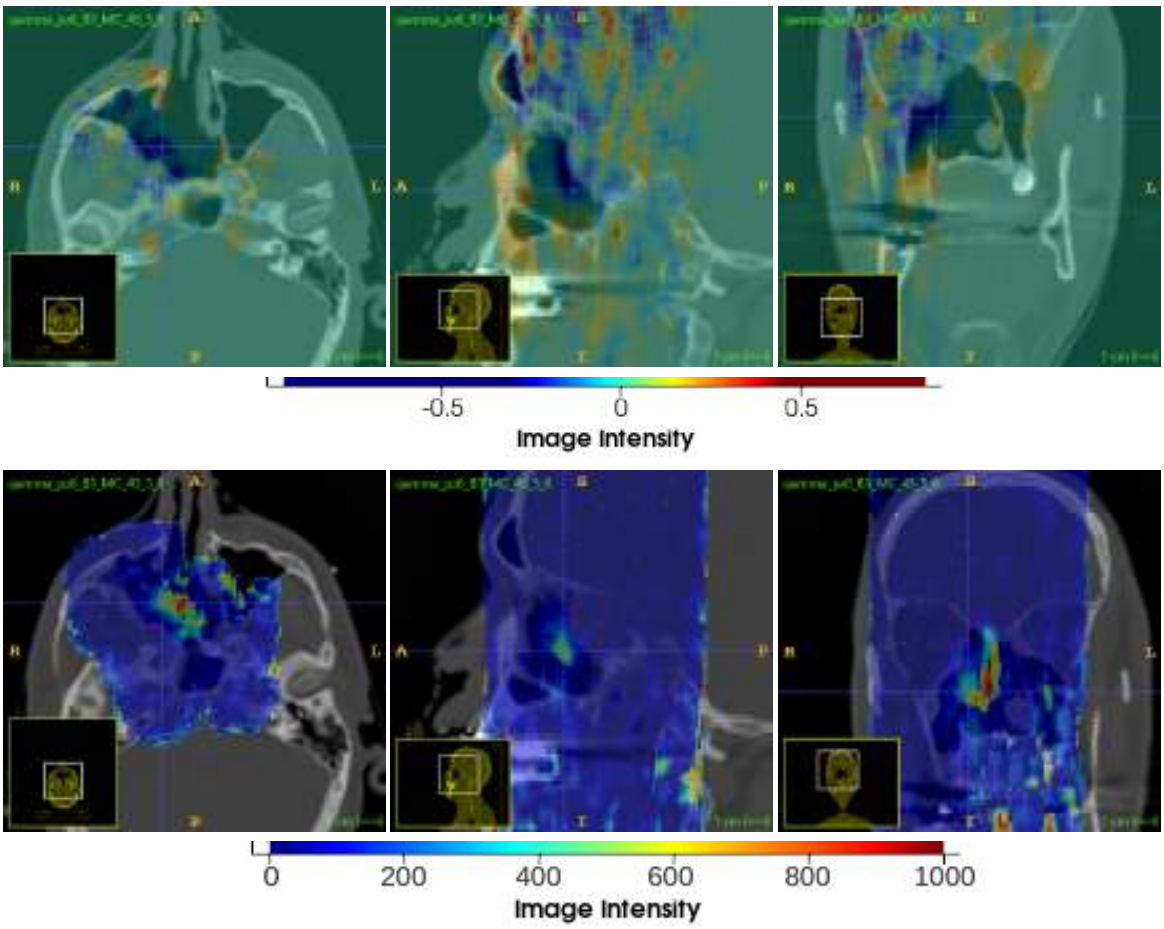

Figure 4.6: Patient 6 POCA difference (top row) and relative percentage difference maps (bottom row) for MC simulated data.

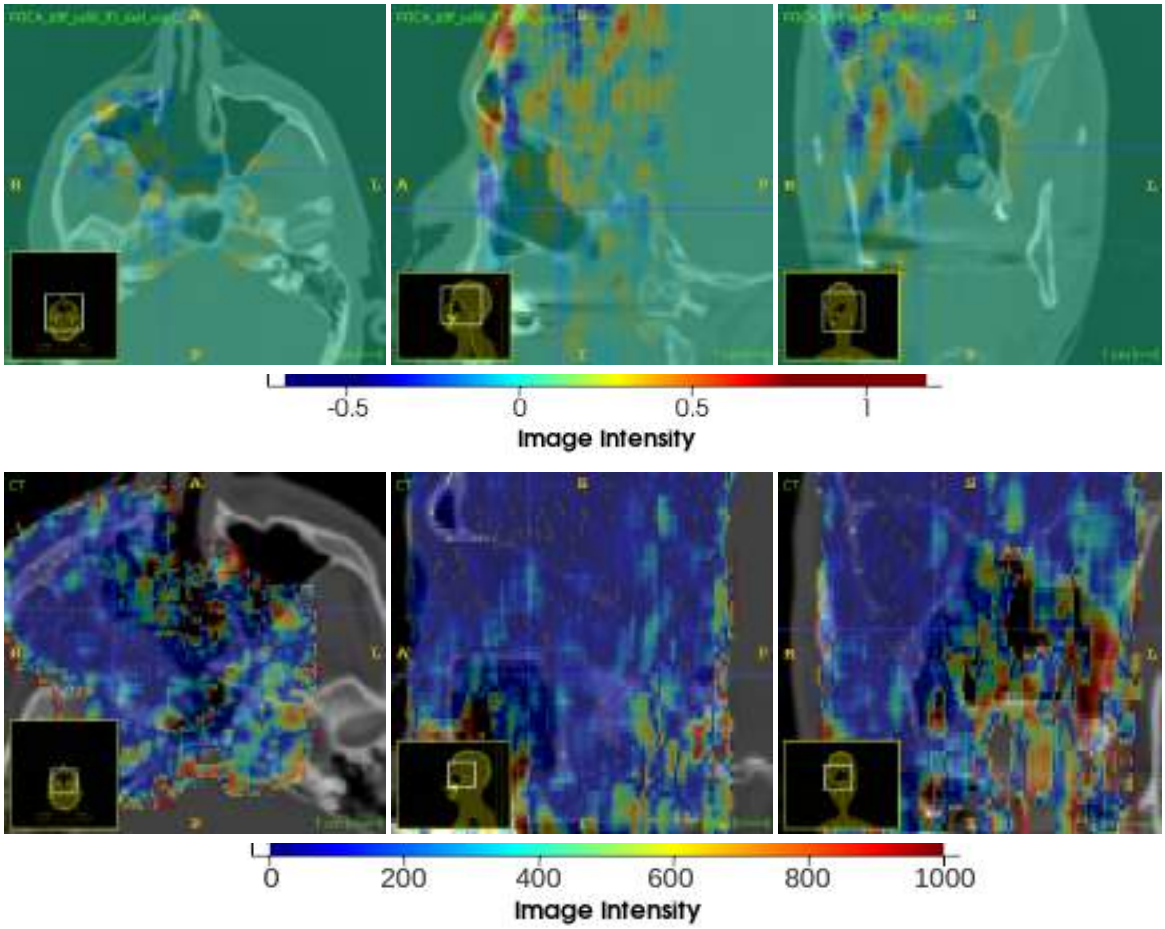

Figure 4.7: Patient 6 POCA difference (top row) and relative percentage difference maps (bottom row) for experimental dataset.

Following the construction of the POCA distributions, the gamma index analysis (see Chapter 3.2) was performed first on the MC dataset and then on the experimental data. Parameter optimisation was conducted by evaluating distance-to-agreement (DTA) values from 2 mm to 8 mm in steps of 2 mm (with an additional intermediate value of 5 mm), the emission density difference (DD) values from 20% to 55% in increments of 5%, and dose threshold (DTH) values from 0.1% to 0.5% in steps of 0.1%. The metrics described in Section 3.2.4 have been evaluated inside a region of interest (ROI) rectangular area containing the morphological variation emerged from the ΔHU > 500 map (see Figure 4.2), as shown in Figure 4.8. The decision to focus exclusively on the primary morphological variation was driven by its greater overlap with the high-dose treatment region (see Figure 4.3).

Figure 4.9 displays the MC dataset efficiency and purity trends as a function of DD across the evaluated DTA values (colour-coded according to the legend). Only the curves for DTH = 0.1% (Figure 4.9, top row), 0.3% (Figure 4.9, middle row), and 0.5% (Figure 4.9, bottom row) are presented to illustrate the trend behaviour of both metrics: efficiency is higher for lower values of DD, DTA, and DTH and decreases monotonically with increasing DD, whereas purity improves with higher DTH values and exhibits a monotonic increase for

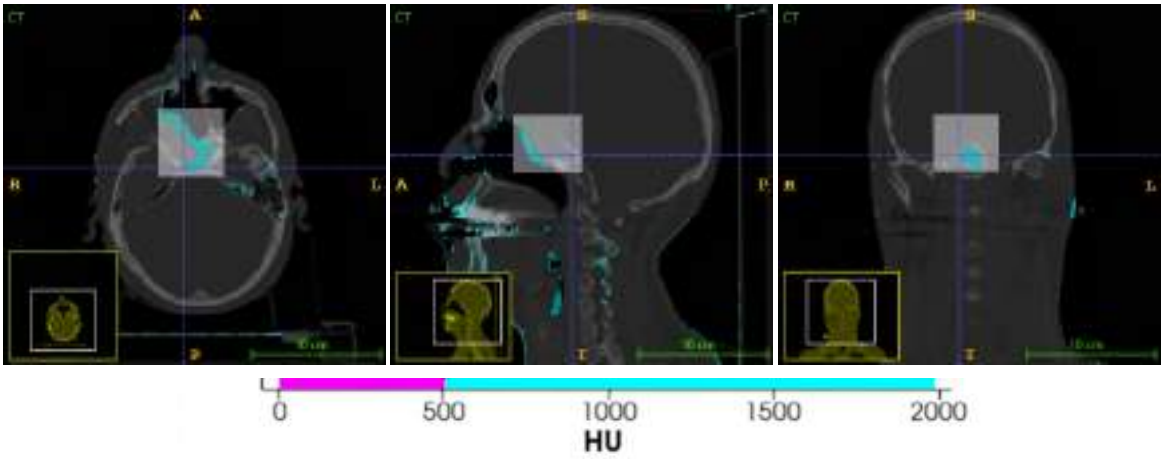

Figure 4.8: ROI (white transparent box) area overlaid on the planning CT and on the ΔHU > 500 map (turquoise).

higher DD and DTA values. Additionally, while purity exhibits a steeper decline at lower DTH values, the slope of the efficiency curve increases with higher DTH values.

Figure 4.10 extends the analysis presented in Figure 4.9 to the experimental dataset. In contrast to the MC simulation data, increasing DTH values results in an overall decrease in both purity and efficiency. The latter, in particular, exhibits a distinct behaviour at DTH $= 0.5\%$ (Figure 4.10, bottom row): its curve initially displays a positive slope, reaches a maximum at DD $= 35\%$, and then declines.

As mentioned in Section 3.2.4, maximising purity significantly reduces noise contribution in gamma maps, highlighting true anatomical variations at the expense of sensitivity to subtler morphological changes. Conversely, efficiency maximisation enhances the detention of anatomical variations, but it introduces noisy false-positives regions that may be misleading when assessing the morphological variations without *a priori* information about their location. Optimal parameter configurations are therefore chosen to balance efficiency and purity. This equilibrium increases the possibility to detect significant anatomical changes while filtering out noise, thereby preserving the overall accuracy of the gamma index maps.

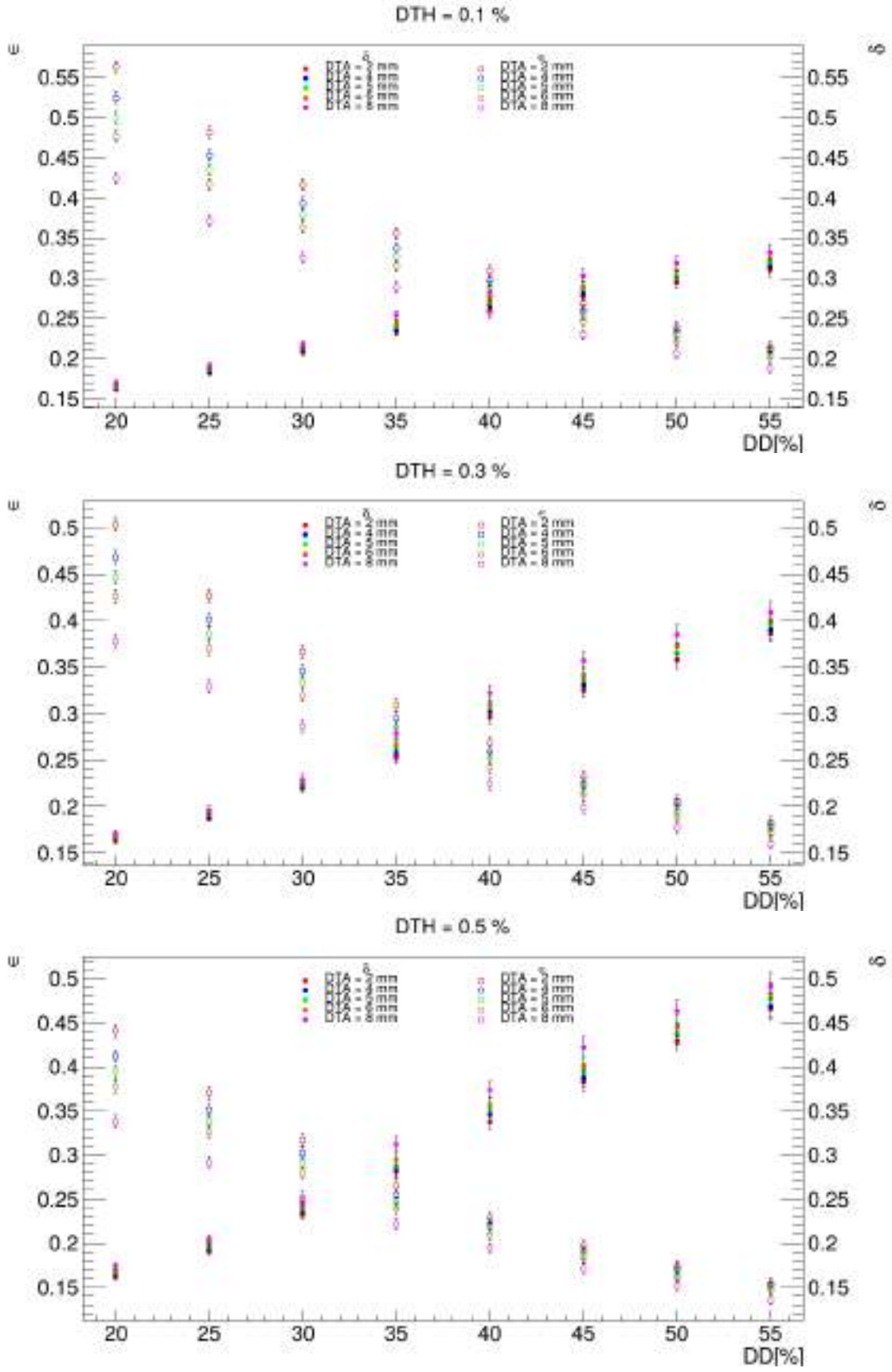

Figure 4.9: Efficiency and purity trends for MC data as a function of DD across the evaluated DTA values for DTH = 0.1% (top row), 0.3% (middle row), and 0.5% (bottom row).

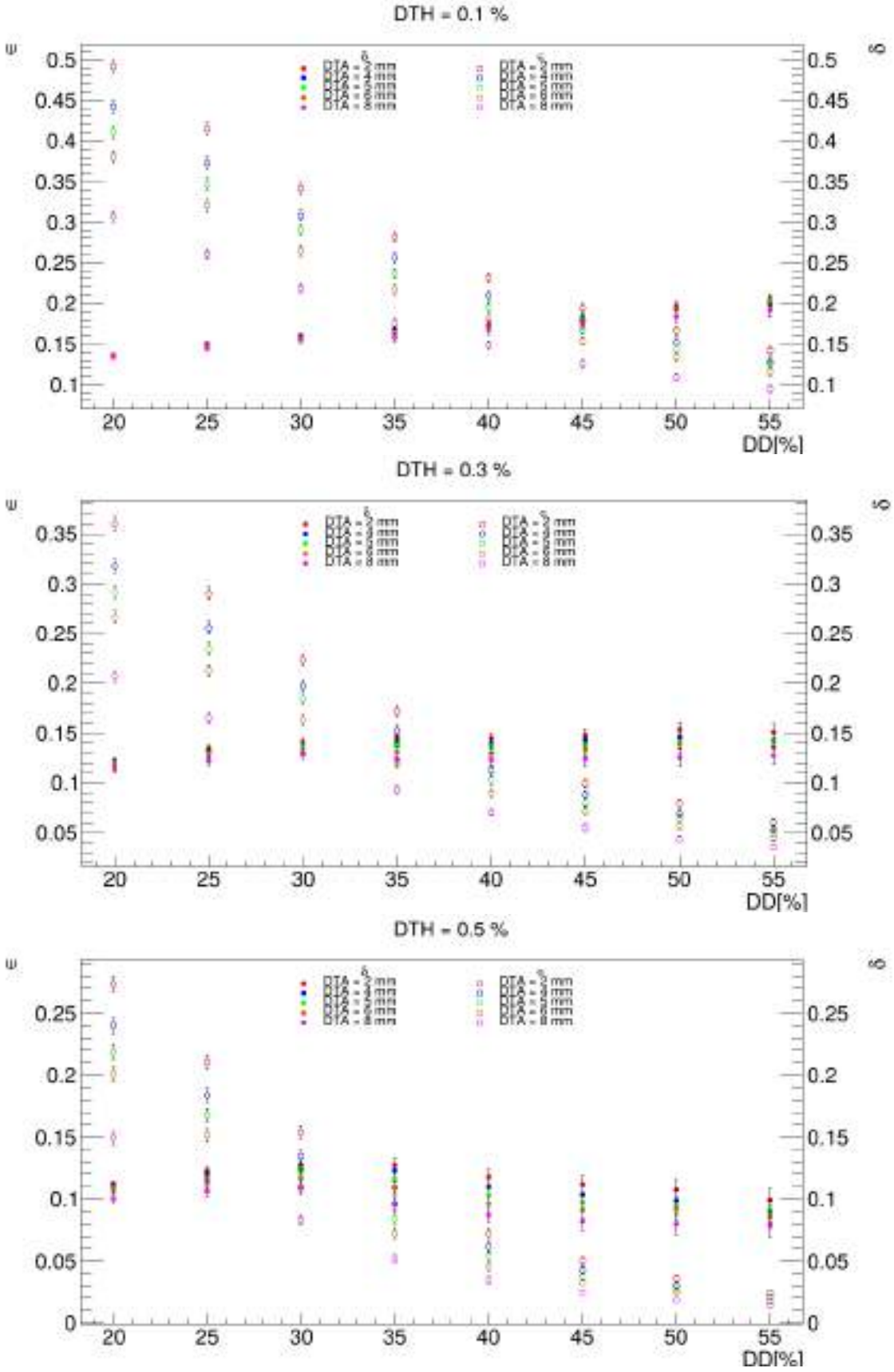

Figure 4.10: Efficiency and purity trends for experimental dataset as a function of DD across the evaluated DTA values for DTH = 0.1% (top row), 0.3% (middle row), and 0.5% (bottom row).

To minimise false positives within gamma index maps, purity optimisation was prioritised over efficiency enhancement. An intermediate value of DD = 45% was selected. Paired with DTA = 5 mm and DTH = 0.3%, this configuration yields a higher efficiency than larger distances, which, despite further improving purity, would compromise sensitivity. The resulting distributions, illustrated in Figure 4.11 in passrate mode (see Section 3.2.1), achieve an effective trade-off between image clarity and the identification of morphological changes. However, only the deeper and more pronounced anatomical variation is partially identified. Table 4.3 shows the precise values for each evaluated metric. Specifically, with the selected parameters choice an efficiency of $\approx 21\%$ and a purity roughly equal to 37% are achieved.

ε	δ	η	ρ
0.212 ± 0.006	0.370 ± 0.009	0.779 ± 0.001	0.375 ± 0.001

Table 4.3: Patient 6 metric values for the DD = 45%, DTA = 5 mm and DTH = 0.3%. triplet (MC data).

As for the experimental data, a gamma index map (see Figure 4.12) built with optimal triplet values of DD = 45%, DTA = 5 mm and DTH = 0.1% was selected following the same criteria applied for the MC simulated dataset (see Figure 4.10). A dose threshold of DTH = 0.1% was selected because higher values inappropriately excluded voxels corresponding to the morphological variation from the analysis. The metrics values are shown in Table 4.4. A comparison with the results obtained for the MC simulations (Table 4.3) highlights an overall reduction in the metrics values.

ε	δ	η	ρ
0.167 ± 0.005	0.208 ± 0.006	0.087 ± 0.001	0.066 ± 0.001

Table 4.4: Patient 6 metric values for the DD = 45%, DTA = 5 mm and DTH = 0.1%. triplet (experimental data).

In this case, only a small fraction of the morphological variation identified in the Monte Carlo simulated data is detected. Furthermore, without *a priori* knowledge regarding the positioning of the anatomical variation, it would not be possible to distinguish it from the spurious green voxel clusters nearby due to their similar spatial extent. The primary reason behind the detection inefficiency lies in the location of the morphological variation itself, where the POCA emission density is scarce. Charged secondary fragments generated in the innermost regions have to cross a significant thickness of tissue before being detected by the Dose Profiler, and this leads to an attenuation of the detected statistics. Moreover, the acquisition of the planning CT twenty days prior to the start of treatment may also contribute to the observed degradation in the DP performance in the experimental data analysis: morphological variations may have naturally resolved within the time interval between the planning CT and the first treatment fraction, therefore limiting the magnitude of any true structural changes occurring between the first and seventh fractions when the

control CT was acquired. To address this problem, an additional CT scan has been acquired for each patient on the day of the first treatment fraction in the second part of the clinical trial.

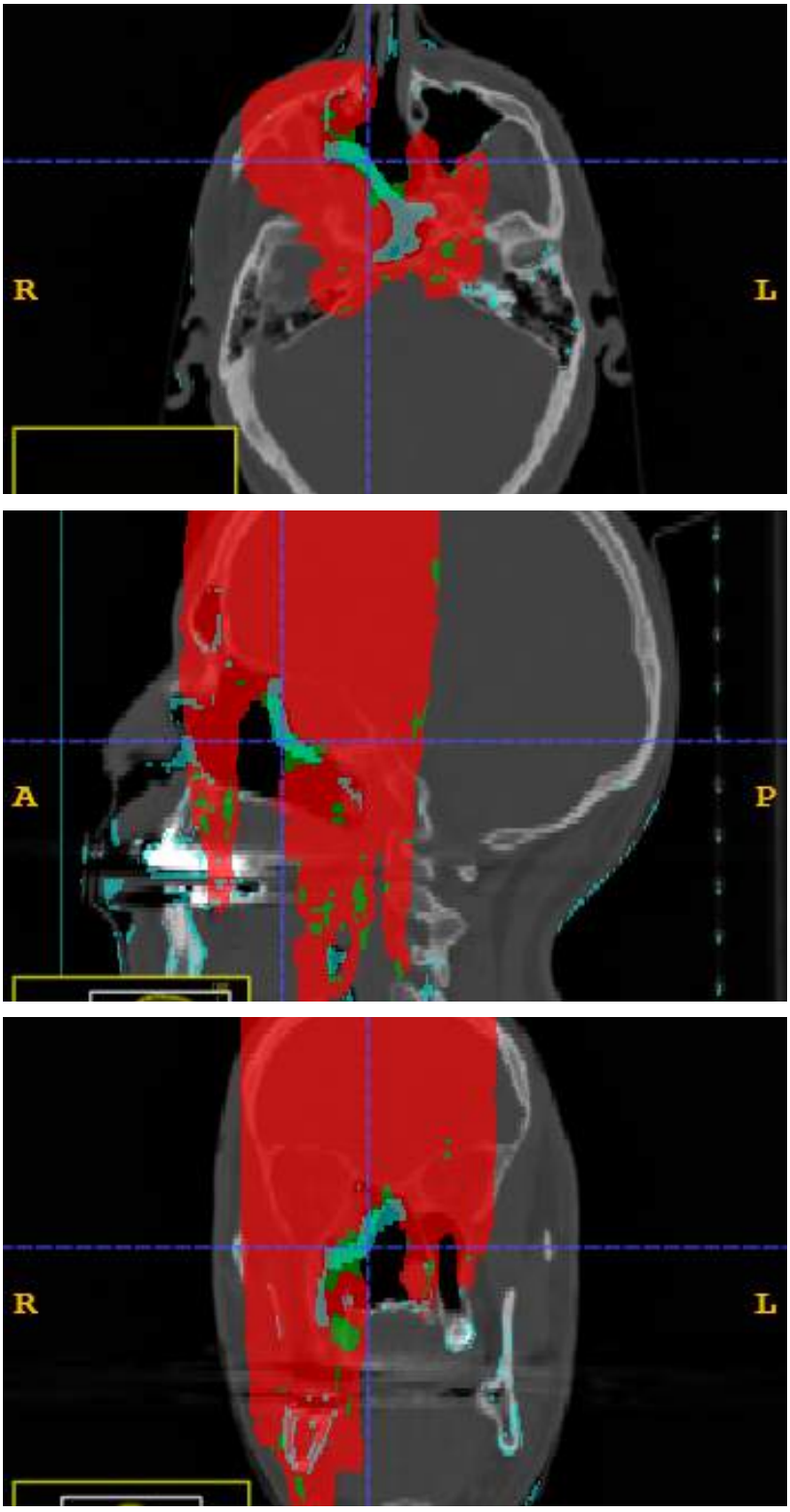

Figure 4.11: MC simulated data passrate map for DD = 45%, DTA = 5 mm, DTH = 0.3% in transverse (top row), sagittal (middle row), and coronal (bottom row) views, overlaid on the planning CT and on the ΔHU > 500 map.

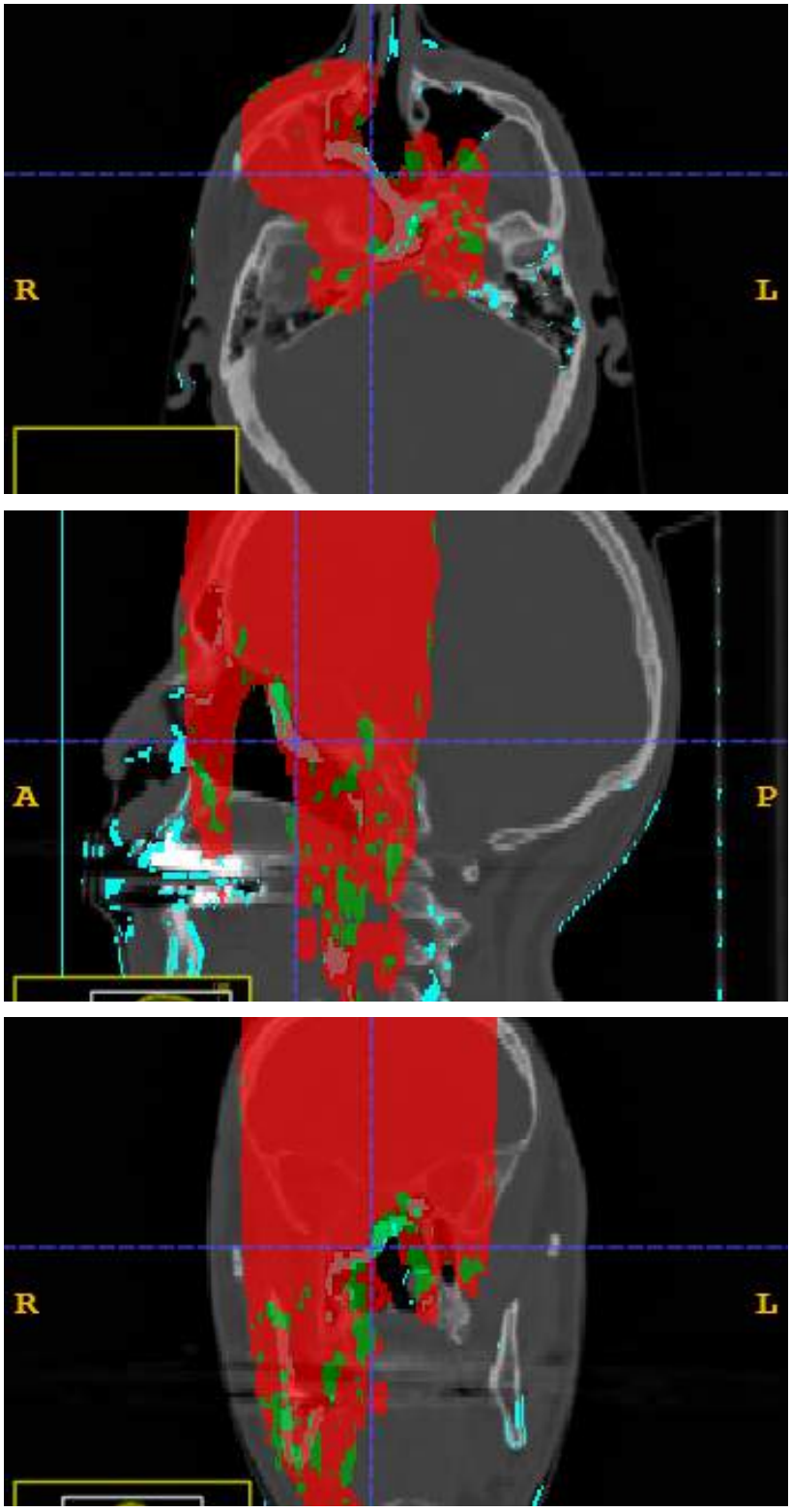

Figure 4.12: Experimental data passrate map for DD = 45%, DTA = 5 mm, DTH = 0.1% in transverse (top row), sagittal (middle row), and coronal (bottom row) views, overlaid on the planning CT and on the ΔHU > 500 map.

4.2 Patient 15

Patient 15 was diagnosed with clivus chondrosarcoma. The prescribed carbon-ion treatment plan comprised fifteen fractions, delivering a total dose equal to 45 Gy(E) (see Table 4.1). Table 4.5 details the irradiation fields and the corresponding number of primary particles; the A1 field acquired by the Dose Profiler is highlighted in bold.

Field	Irradiation angle (°)	Number of Primary Particles
A1	**0**	$\mathbf{2.24 \times 10^8}$
A2	180	2.04×10^8

Table 4.5: Patient 15 parameters of the irradiation fields prescribed in the treatment plan.

A CT scan (referred to as the planning CT) was acquired on the day of the first treatment fraction (16/03/2026), as shown in the left column of Figure 4.13, while a control CT was performed on the day of the final treatment fraction (03/04/2026), reported in the right column of Figure 4.13.

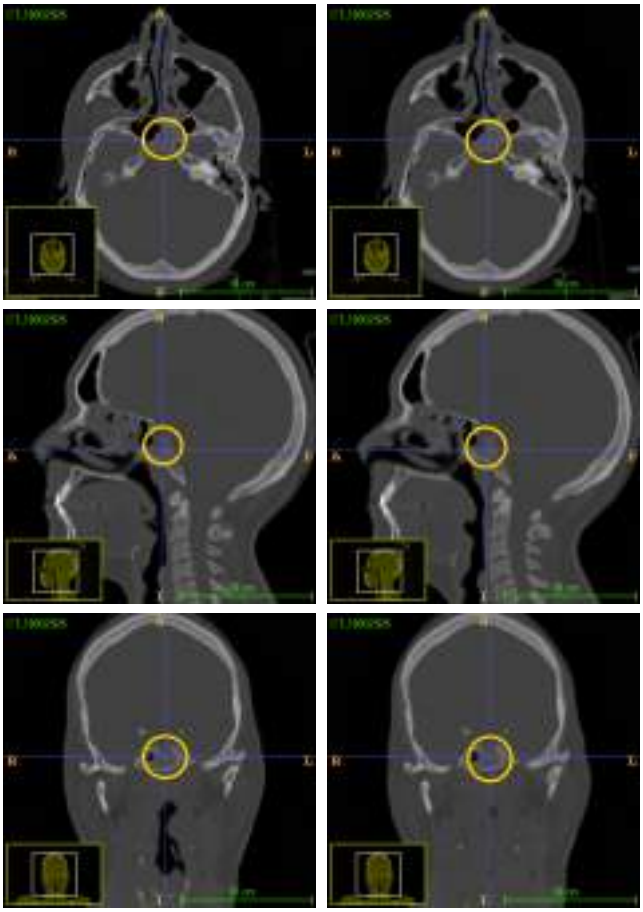

Figure 4.13: Comparison between the planning CT (left column) and the control CT (right column). The target tumour area is circled in yellow.

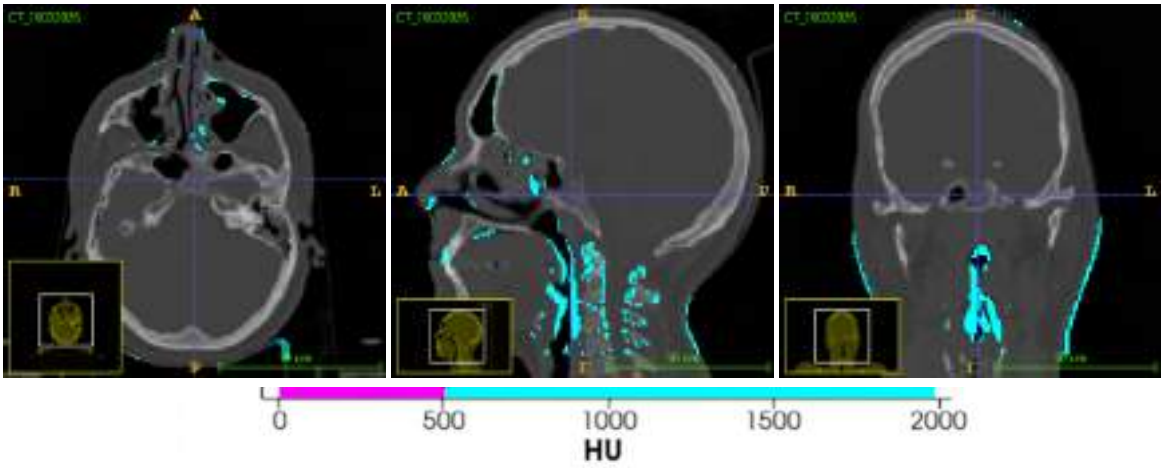

Figure 4.14: ΔHU $>$ 500 map between the planning and control CT scans overlaid on the former (left column). Turquoise areas represent the anatomical variations occurred within the patient.

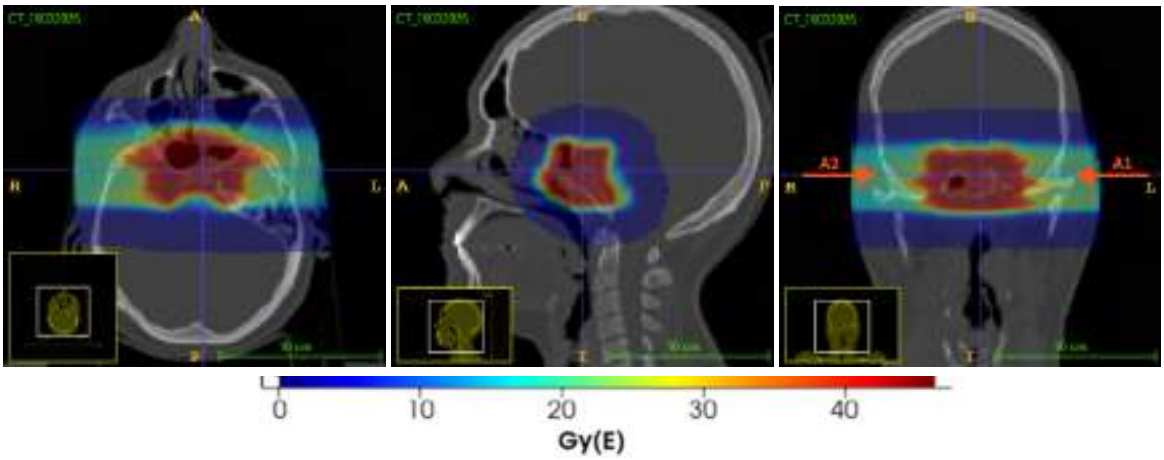

Figure 4.15: Patient 15 prescribed dose distribution for the A1 and A2 irradiation fields superimposed on the planning CT.

This patient did not undergo treatment replanning due to the absence of significant anatomical variations within the target tumour volume. Nonetheless, the ΔHU $>$ 500 map (see Section 3.2.3) reveals minor morphological changes as displayed in Figure 4.14. However, because these variations are either located outside the regions irradiated by the RTdose or within low-RTdose margins, they could not be detected by the Dose Profiler, thereby motivating the decision of maintaining the initial treatment plan without replanning. The prescribed dose distribution is displayed in Figure 4.15 using a colour gradient map ranging from blue (low-dose regions) to red (high-dose regions). The orange arrows in the coronal view (Figure 4.15, right) highlight the beam entry directions for the A1 (0°) and the A2 (180°) irradiation fields.

Figure 4.16 compares the same slice of the experimentally reconstructed POCA distributions for the first (top row) and last (bottom row) treatment fractions, superimposed on

the planning CT scan, for the A1 irradiation field. The lack of Monte Carlo simulation data for patient 15 implies that the spatial accuracy of the reconstructed POCA maps (see Section 3.1.4) cannot be independently validated; a spatial positioning error analogous to that characterised in patient 6 (see Section 4.1) cannot be therefore *a priori* excluded. Due to the limited event statistics (see Table 4.5), the POCA distributions exhibit inconsistent spatial profiles across all views, rendering it difficult to run a robust gamma index analysis. Quantitatively, the maximum emission density values recorded for the first and final fractions are 0.988 and 1.052, respectively.

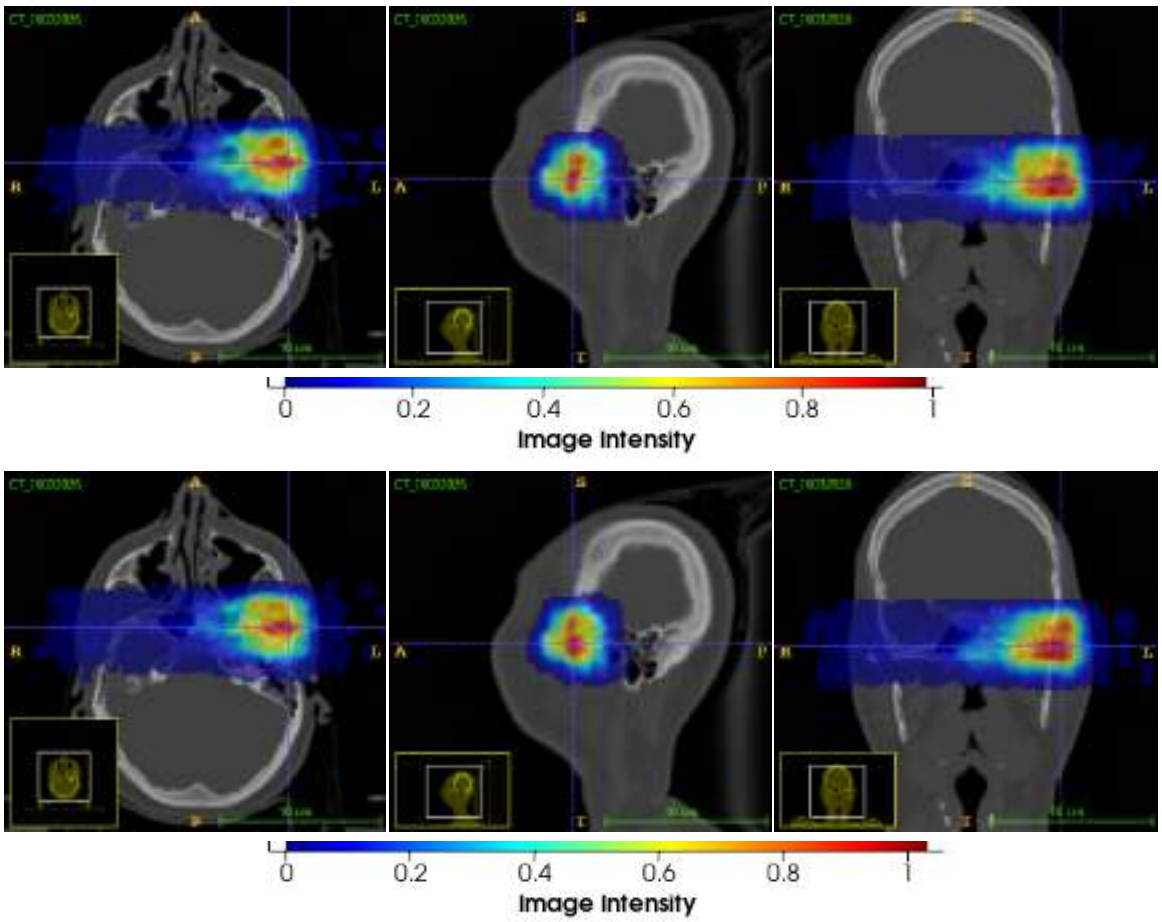

Figure 4.16: Comparison between the same slice across the transverse, sagittal, and coronal views of the experimental POCA distribution for the first (top row) and last (bottom row) treatment fractions.

The POCA difference and relative percentage difference distributions, defined in Section 4.1, are presented in Figure 4.17. While the POCA difference map detects a small region of increased emission corresponding to an anatomical emptying within the target tumour volume (see Figure 4.13), this effect is masked in the relative percentage difference map due to low emission values in the peripheral tails that inflate the relative percentage differences, generating spurious high-value voxels.

The absence of a Monte Carlo simulation dataset also precludes the use of gamma index metrics optimisation to determine the ideal DD, DTA, DTH triplet. Because this tuning procedure strongly relies on spatial fidelity within the reconstructed POCA distributions, positional errors may cause discrepancies between the gamma index output (see Section 3.2) and actual morphological variations identified via the $\Delta HU > 500$ map (see Section 3.2.4). The gamma index maps were evaluated across parameter ranges similar to those established for patient 6: the DTA parameter was investigated from 2 mm to 10 mm in steps of 2 mm (including an intermediate value of 5 mm), DD from 15% to 55% in 5% increments, and DTH from 0.1% to 0.5% in 0.1% steps. To select the optimal parameter triplet, the gamma index distributions were first evaluated at a fixed threshold of DTH = 0.1% to avoid cutting any relevant voxels, across extreme permutations of $DTA_{min} = 2\,mm$, $DTA_{max} = 10\,mm$, $DD_{min} = 15\%$, and $DD_{max} = 55\%$, as depicted in Figure 4.18. Intermediate parameter permutations were therefore explored to identify the triplet yielding the best agreement with the POCA difference and relative percentage difference maps (see Figure 4.17).

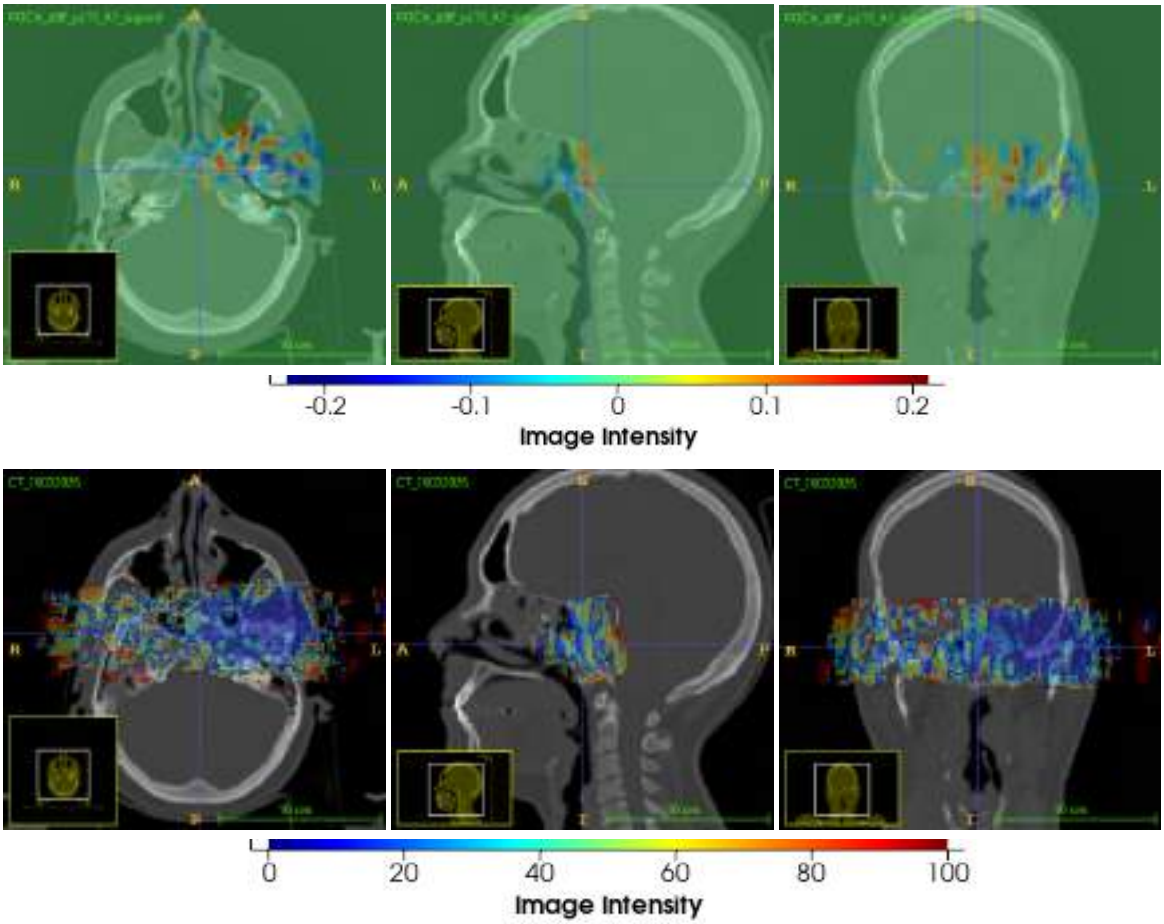

Figure 4.17: Patient 15: absolute POCA difference (top row) and relative percentage difference (bottom row) maps.

Finally, Figure 4.19 shows the gamma index distribution for the selected parameter triplet (DD = 55%, DTA = 10 mm, and DTH = 0.5%). Considering that no significant

anatomical changes occurred inside the target volume covered by the RTdose according to the ΔHU map (see Figure 4.14), expanding the DTA and DD acceptance criteria trivially inflates the amount of voxels classified as non-discrepant by the test towards progressively higher passrate percentages. Under these conditions, a quantitative parametric analysis loses its physical relevance.

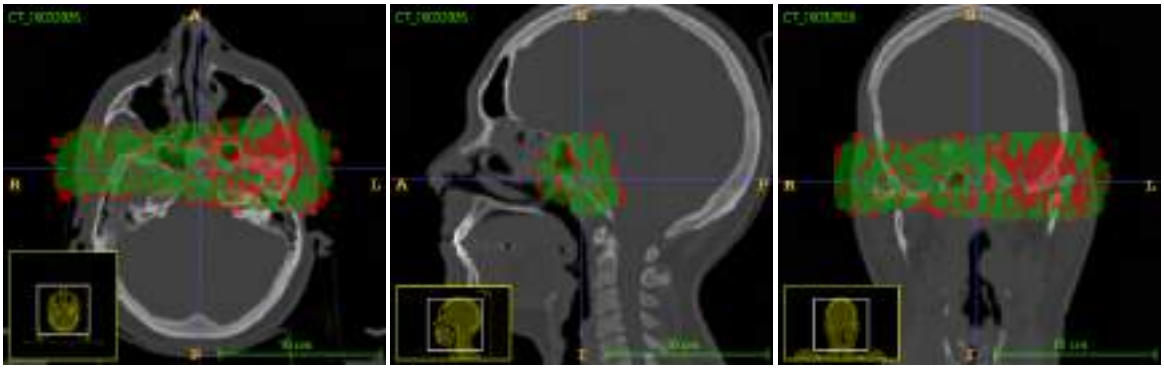

(a)



(b)



(c)



(d)

Figure 4.18: A1 field passrate gamma index maps for fixed DTH = 0.1% and $DD_{min} = 15\%$, $DTA_{min} = 2\,mm$ (a), $DD_{max} = 55\%$, $DTA_{min} = 2\,mm$ (b), $DD_{min} = 15\%$, $DTA_{max} = 10\,mm$ (c), $DD_{max} = 55\%$, $DTA_{max} = 10\,mm$ (d) overlaid on the planning CT.

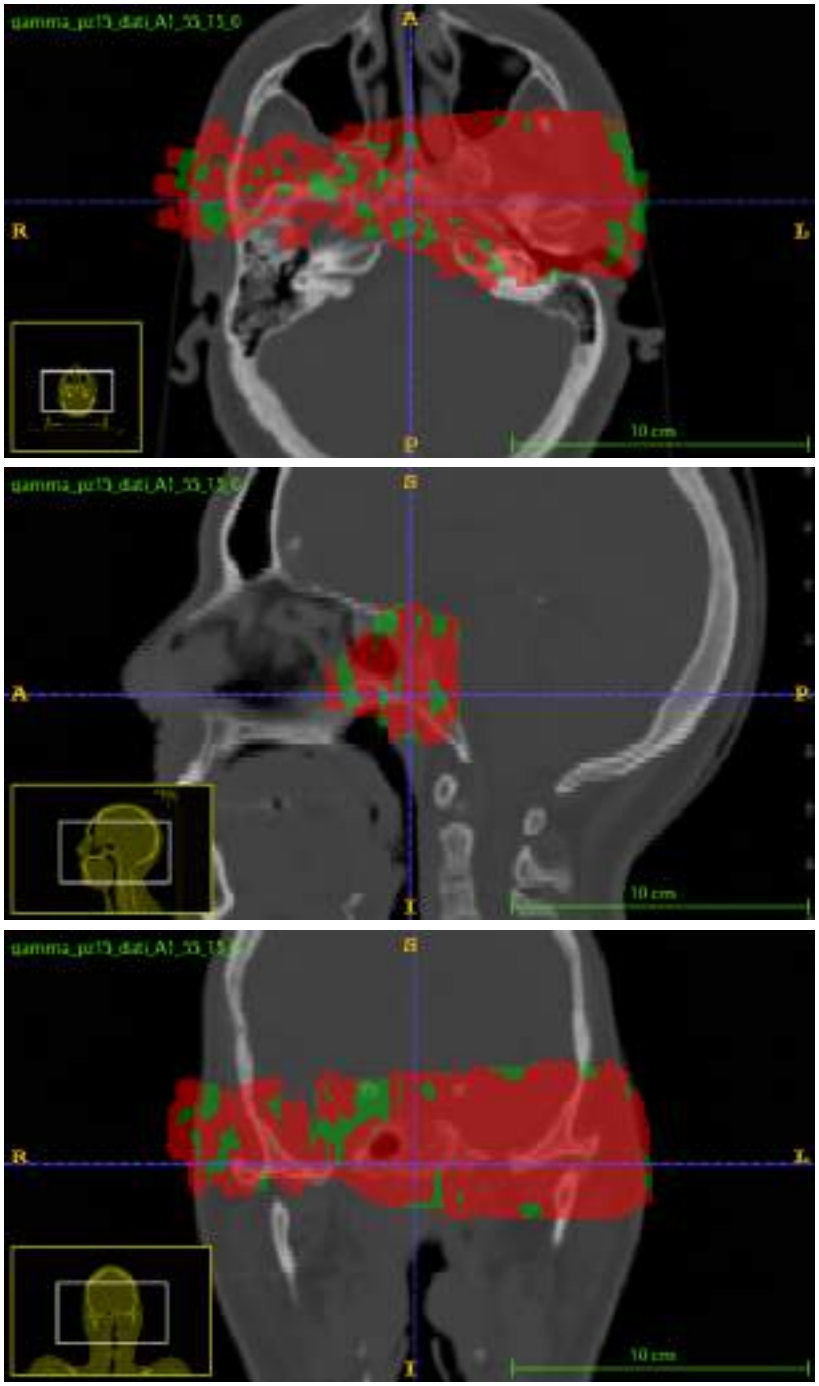

Figure 4.19: A1 field passrate gamma index map for DD = 55%, DTA = 10 mm, and DTH = 0.5% superimposed on the planning CT.

4.3 Patient 18

Patient 18 was diagnosed with Malignant Mucosal Melanoma (MMM). This patient underwent treatment replanning: the first carbon-ion plan comprised three fractions, while the second one comprised six fractions, delivering a total dose equal to 41 Gy(E) (see Table 4.1). Following the ninth fraction the patient received a boost, i.e. an additional radiation dose targeting the residual tumour volume. Tables 4.6, 4.7, and 4.8 detail the irradiation fields and corresponding number of primary particles for the first, second treatment plans, and the boost, respectively. The fields acquired by the Dose Profiler are highlighted in bold.

Field	Irradiation angle (°)	Number of Primary Particles
A1	**350**	**28.19 × 10^8**
A2	**300**	**13.40 × 10^8**
A3	**180**	**15.07 × 10^8**

Table 4.6: Patient 18 parameters of the irradiation fields prescribed in the first treatment plan (first - third fractions).

Field	Irradiation angle (°)	Number of Primary Particles
B1	**350**	**28.77 × 10^8**
B2	**300**	**18.47 × 10^8**
B3	**180**	**14.18 × 10^8**

Table 4.7: Patient 18 parameters of the irradiation fields prescribed in the second treatment plan (fourth - ninth fractions).

Field	Irradiation angle (°)	Number of Primary Particles
C4	**350**	**16.92 × 10^8**
C5	**300**	**14.43 × 10^8**
C6	**180**	**9.19 × 10^8**

Table 4.8: Patient 18 parameters of the irradiation fields prescribed in the boost (from the tenth fraction onwards).

The planning CT (see Figure 4.20, left columns) was acquired on the first day of the treatment (03/06/2026) and used to outline the second treatment plan. Moreover, a control CT scan was scheduled on the day of the ninth fraction (18/06/2026), as shown in the right columns of Figure 4.20, revealing morphological variations within the patient's anatomy (highlighted by the yellow circles in Figure 4.20 and by the matching turquoise areas in the ΔHU > 500 map in Figure 4.21). Since the initial treatment plan comprised only three fractions without significant anatomical changes occurring, only the second treatment plan's analysed data is presented in this thesis, according to the structure outlined for patient 6 in Section 4.1.

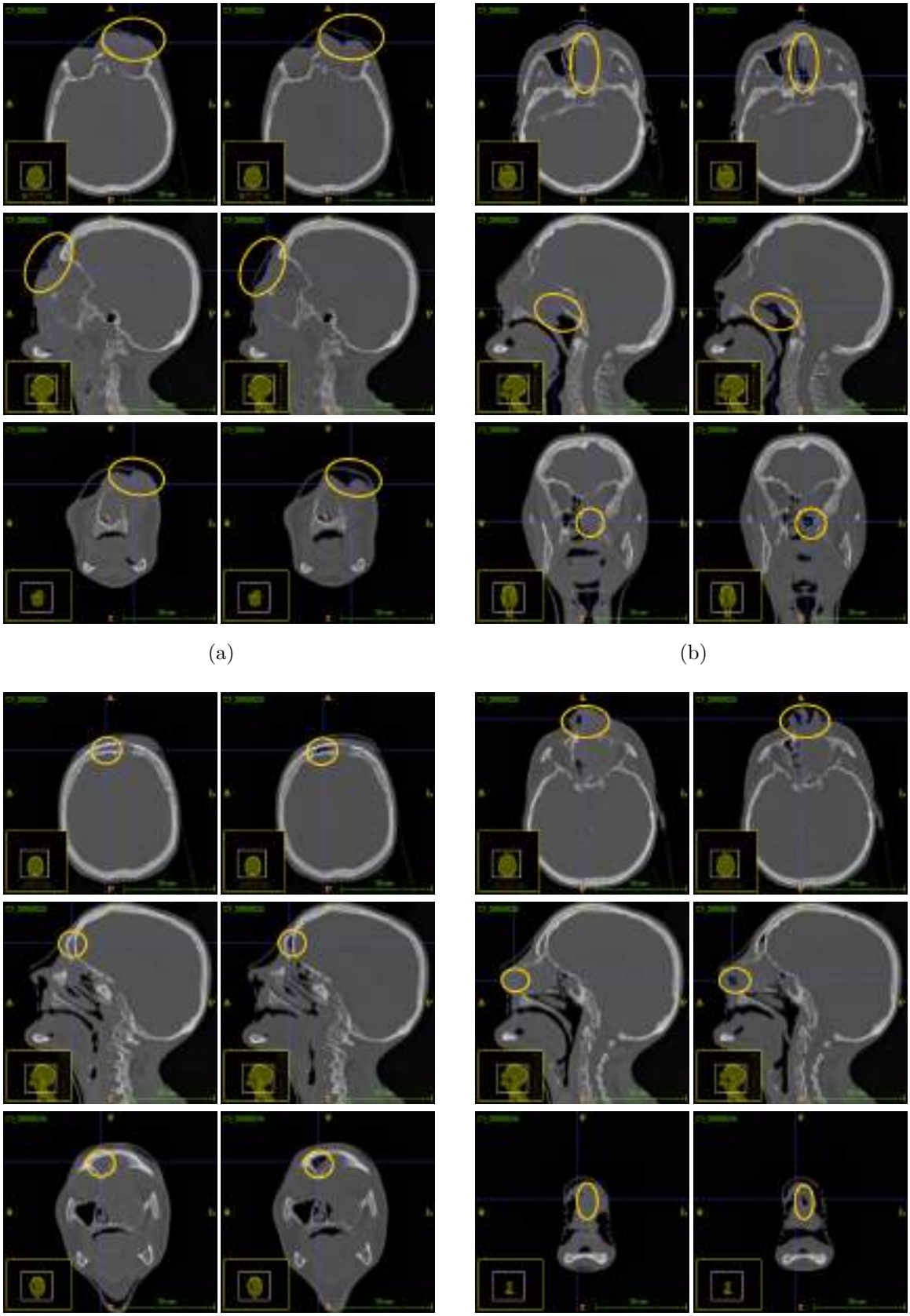

Figure 4.20: Comparison between the planning CT (left column: transverse, sagittal, and coronal views) against the control CT (right column: transverse, sagittal, and coronal views), displaying four distinct anatomical variations (a), (b), (c), and (d) circled in yellow.

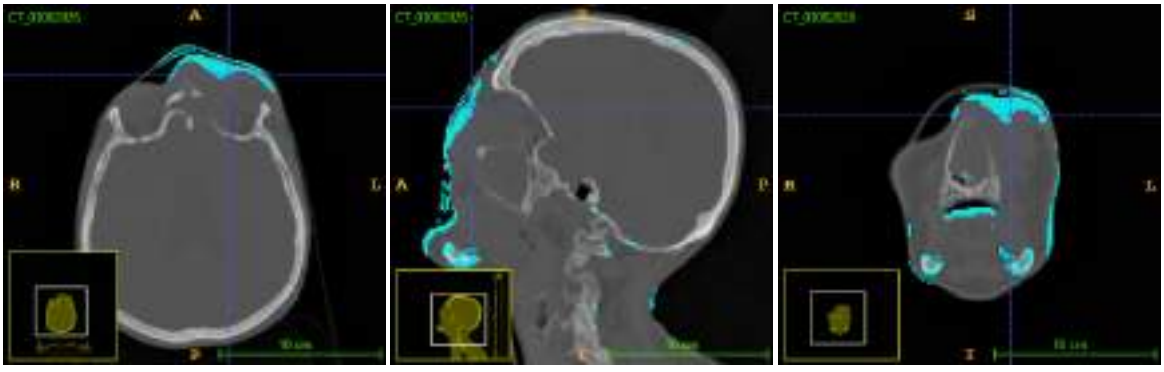

(a)

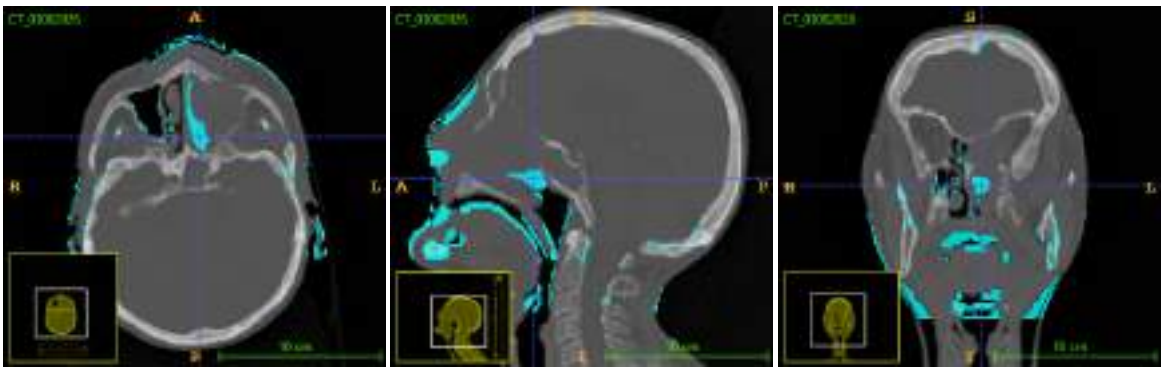

(b)

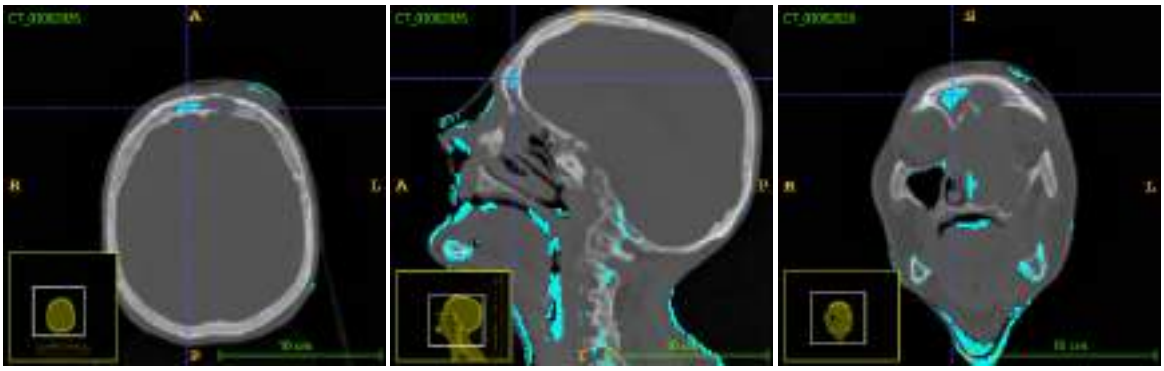

(c)

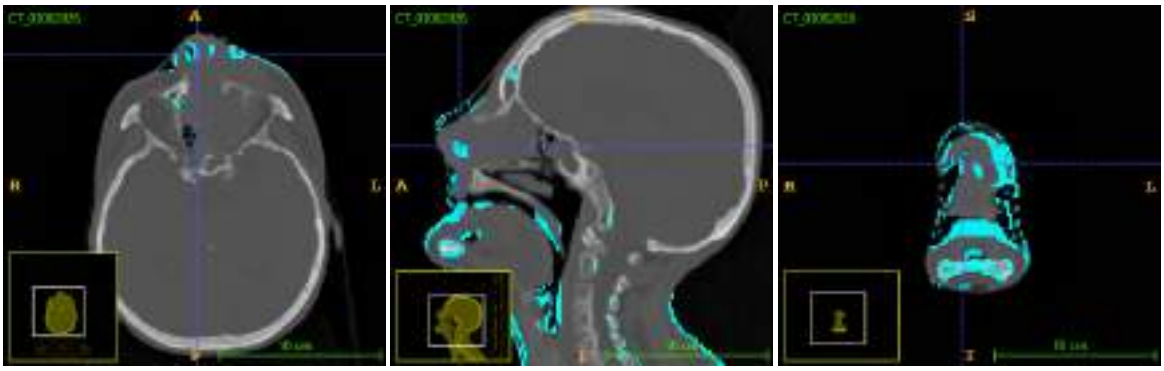

(d)



Figure 4.21: Patient 18 ΔHU > 500 map between the planning and control CT scans visualised superimposed on the former. Turquoise areas display anatomical variations occurred within the patient, as highlighted in Figure 4.20 (a) to (d).

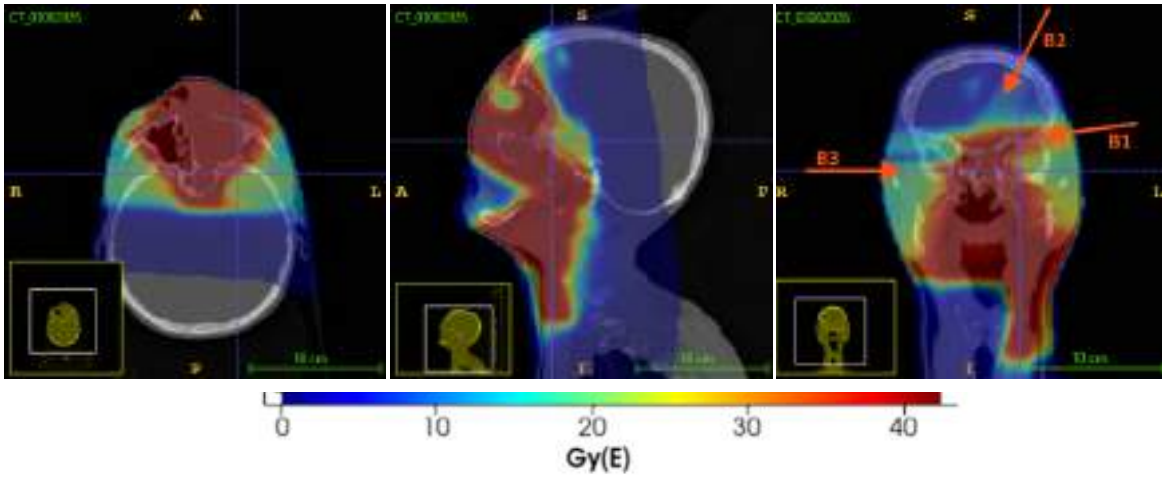

Figure 4.22: Prescribed dose distribution for patient 18 for the B1, B2, and B3 irradiation fields overlaid on the planning CT. The delivered dose is displayed using a colour gradient map ranging from blue (low-dose regions), to red (high-dose regions).

Figure 4.22 enables the visualisation of the prescribed dose distribution overlaid on the planning CT scan. The orange arrows in the coronal plane (Figure 4.22, right) show the beam entry directions for each irradiation field (see Table 4.7).

Figure 4.23 compares the experimentally reconstructed POCA distributions for the fourth (left column) and ninth (right column) treatment fractions, superimposed on the planning CT scan, for the B1 (a), B2 (b), and B3 (c) irradiation fields. Similarly to patient 15, the lack of Monte Carlo simulation data for patient 18 implies that the spatial accuracy of the reconstructed POCA maps (see Section 3.1.4) cannot be independently validated; consequently, a spatial positioning error analogous to that characterised in patient 6 (see Section 4.1) cannot be excluded. Nonetheless, the compared fractions appear to be mutually co-registered, rendering the gamma index analysis (see Section 3.2) possible. Quantitatively, the B1 field exhibits maximum values of 12.567 and 14.117, the B2 field 14.862 and 13.705, and the B3 field 4.300 and 4.127.

The POCA difference and relative percentage difference maps, defined in Section 4.1, are presented in Figures 4.24 and 4.25. Specifically, Figure 4.24 illustrates the POCA difference between the fourth and ninth treatment fractions for the B1 (top row), B2 (middle row), and B3 (bottom row) irradiation fields, reflecting the anatomical changes (see Figures 4.20 and 4.21). Figure 4.25 (top and middle row) displays two distinct slice views for the B1 field, partially highlighting the morphological variations shown in Figure 4.21 top and bottom row, respectively. In contrast, Figure 4.25 (bottom row) shows the relative percentage POCA difference for the B2 field, which highlights the anatomical variation depicted in Figure 4.21 (top row).

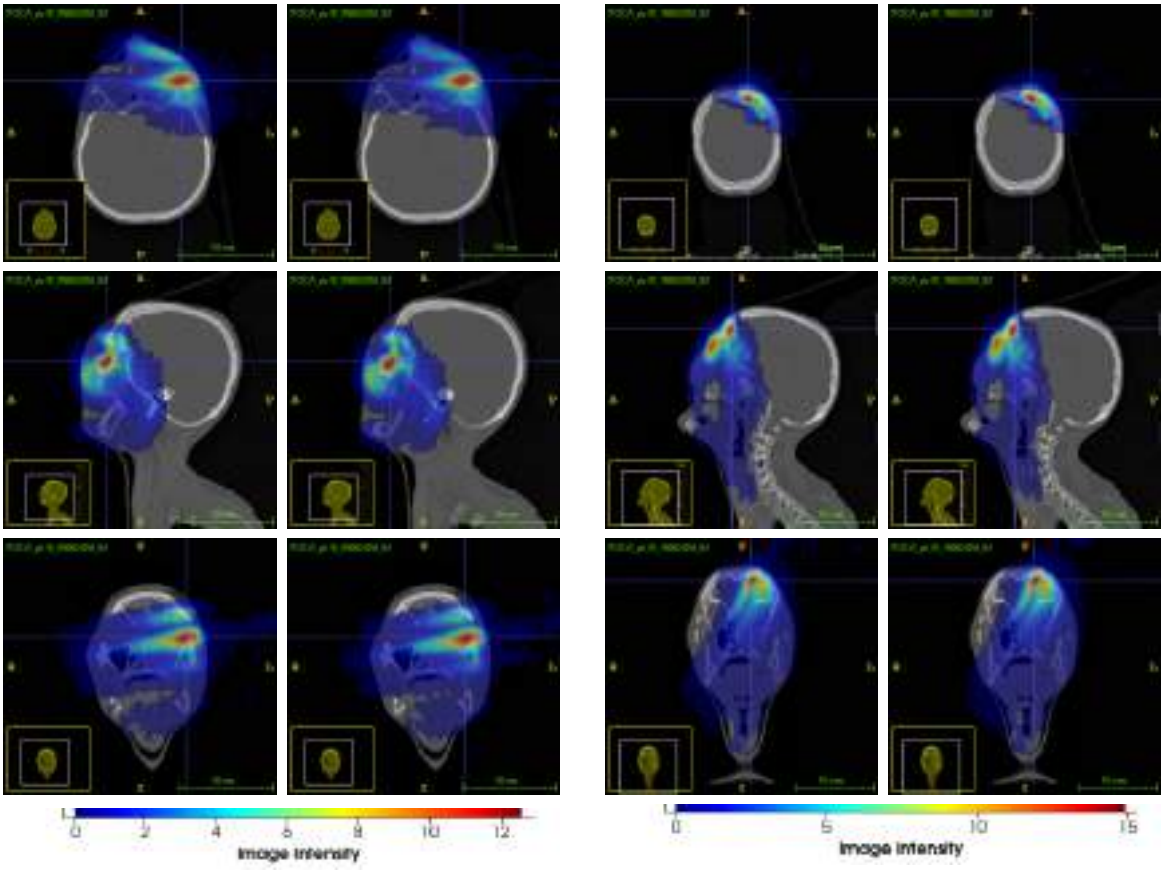

(a) (b)

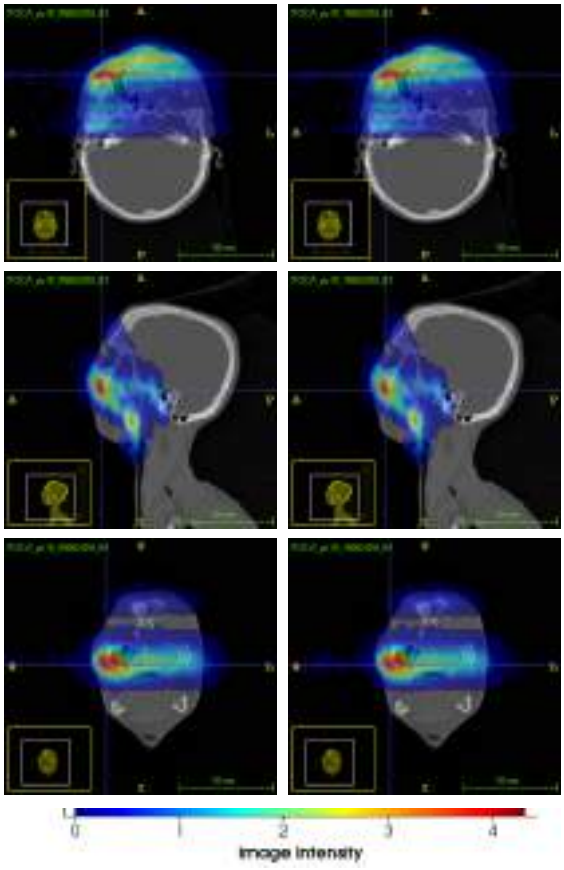

(c)

Figure 4.23: Comparison between the same slice across the transverse, sagittal, and coronal views of the experimental POCA distribution for the fourth (left column) and ninth (right column) fractions for the B1 (a), B2 (b), and B3 (c) irradiation fields.

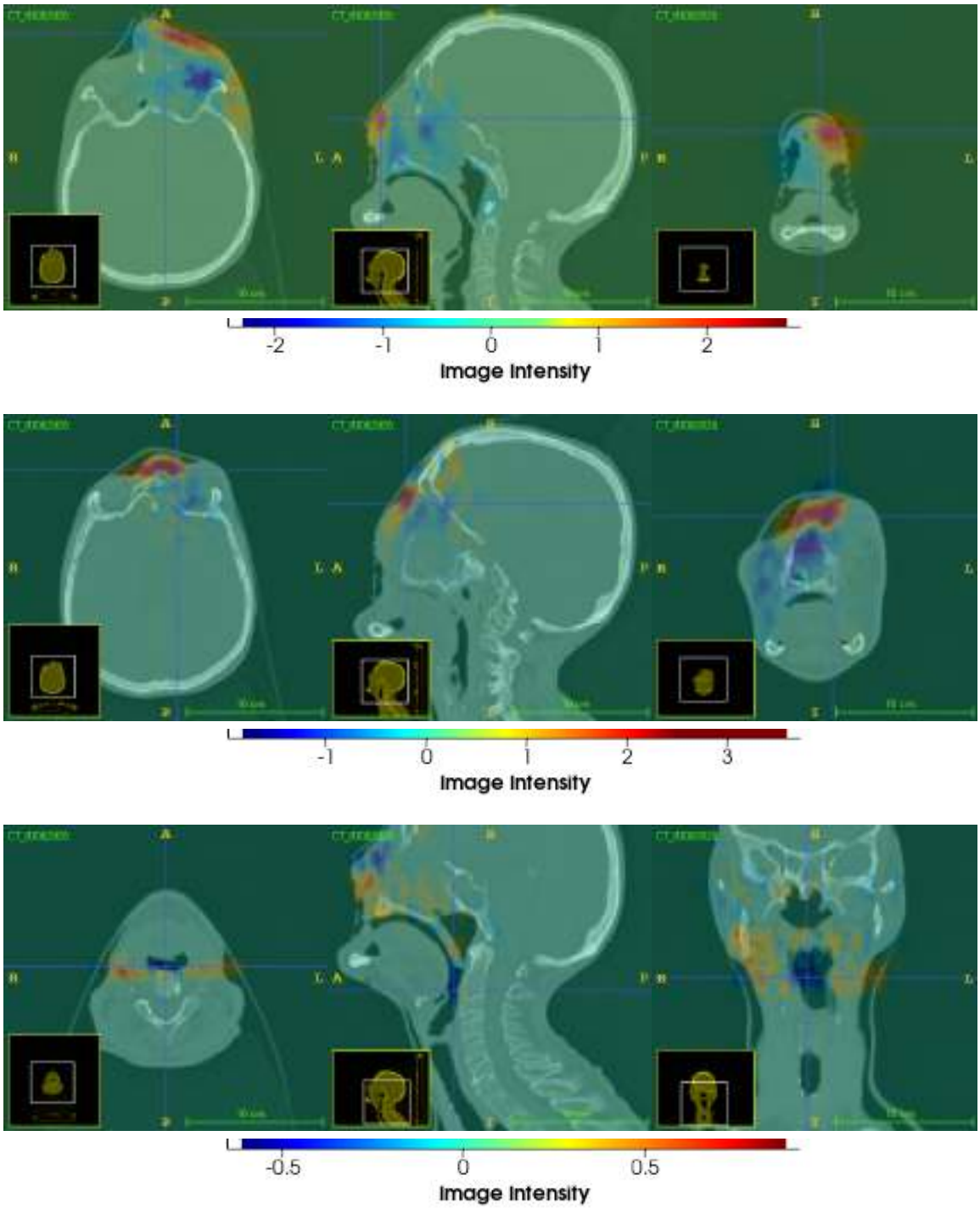

Figure 4.24: Patient 18 experimental data POCA difference between the fourth and the ninth treatment fractions for the B1 (top row), B2 (middle row), and B3 (bottom row) irradiation fields.

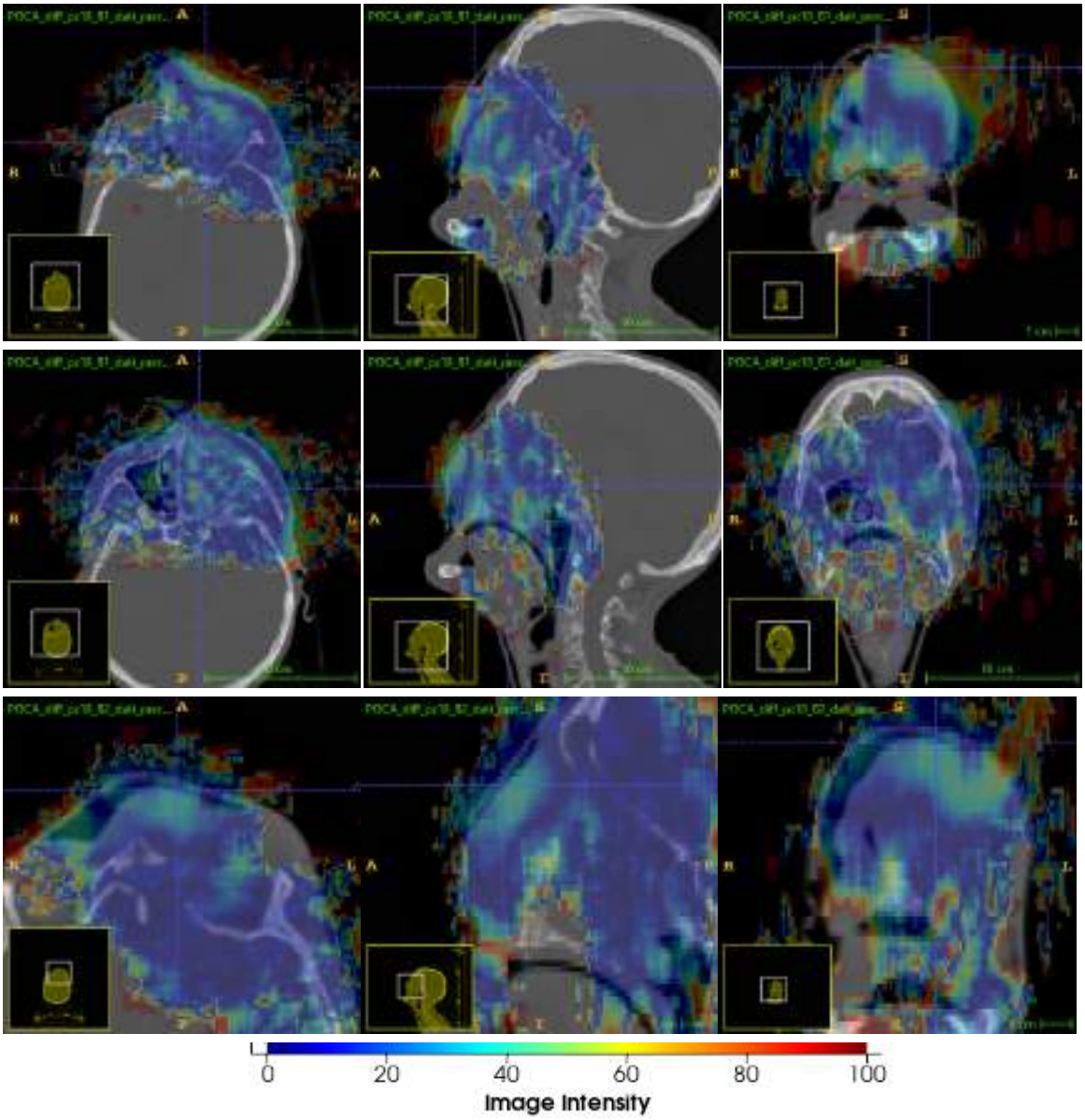

Figure 4.25: Patient 18 experimental data POCA relative percentage difference between the fourth and the ninth treatment fractions for the B1 (top row), (middle row), and B2 (bottom row) irradiation fields.

Analogously to patient 15, the absence of a Monte Carlo simulated dataset results in the inability to rely on gamma index parameter optimisation to select the optimal (DD, DTA, DTH) triplet. This optimisation process requires guaranteed spatial accuracy in the reconstructed POCA distributions; otherwise, the morphological variations flagged by the gamma index test may not align with the true anatomical changes identified in the ΔHU map (see the metrics definition in Section 3.2.4). The gamma index maps were evaluated across parameter ranges similar to those established for Patient 6: the DTA parameter was investigated from 2 mm to 10 mm in steps of 2 mm (including an intermediate value of 5 mm), DD from 15% to 55% in 5% increments, and DTH from 0.1% to 0.5% in 0.1%

steps. To select the optimal parameter triplet, the gamma index maps were first evaluated at a fixed threshold of DTH = 0.1%, to avoid cutting any relevant voxels, across extreme permutations of $\mathrm{DTA}_{\mathrm{min}} = 2\,\mathrm{mm}$, $\mathrm{DTA}_{\mathrm{max}} = 10\,\mathrm{mm}$, $\mathrm{DD}_{\mathrm{min}} = 15\%$, and $\mathrm{DD}_{\mathrm{max}} = 55\%$, as depicted in Figures 4.26, 4.28, and 4.30 for the B1, B2, and B3 irradiation fields, respectively. Intermediate parameter permutations were therefore explored to identify the triplet yielding the best agreement with the POCA difference and relative percentage difference maps (see Figures 4.24 and 4.25).

This process led to the selection of the parameter triplet DD = 45%, DTA = 5 mm, and DTH = 0.3% for the B1 field, as highlighted in Figure 4.27: the left column displays the partially identified superficial anatomical variation matching Figure 4.21a, whereas the right column marginally matches the morphological change shown in Figure 4.21c.

Inspection of the maps corresponding to the B2 field motivated an extended parameter evaluation across additional values of DTA = 12, 15 mm and DTH = 0.6%, 0.7%, 0.8%. Figure 4.29 illustrates the gamma index distribution corresponding to the final selected triplet of DD = 25%, DTA = 15 mm, and DTH = 0.8% for the B2 irradiation field. This choice enables a partial visualisation and identification of the most superficial anatomical change (see Figure 4.21a) while suppressing misleading, spurious green voxel clusters. An exception occurs in the coronal view, which displays a fictitious anatomical variation. This apparent morphological change arises from an increased concentration of reconstructed charged secondary fragments emission vertexes along the primary beam path: due to the reduction in tumour tissue density between the compared fractions, the primary beam traversed less mass before stopping, thereby increasing its range, and shifting the charged secondary fragment production region downstream.

The gamma index maps for the B3 field demonstrated poor sensitivity in detecting the deep morphological changes occurring in the pharyngeal region, shown in Figure 4.21c in the sagittal view (middle). This reduced performance is mainly due to the low secondary statistics inherent to deep-seated targets, in contrast to the higher statistics collected for the B1 and B2 fields, which targeted more superficial anatomical structures, as reflected by the maximum emission values in the POCA reconstructions listed above. Hence, no gamma index distribution is shown for the optimal triplet configuration of the B3 field.

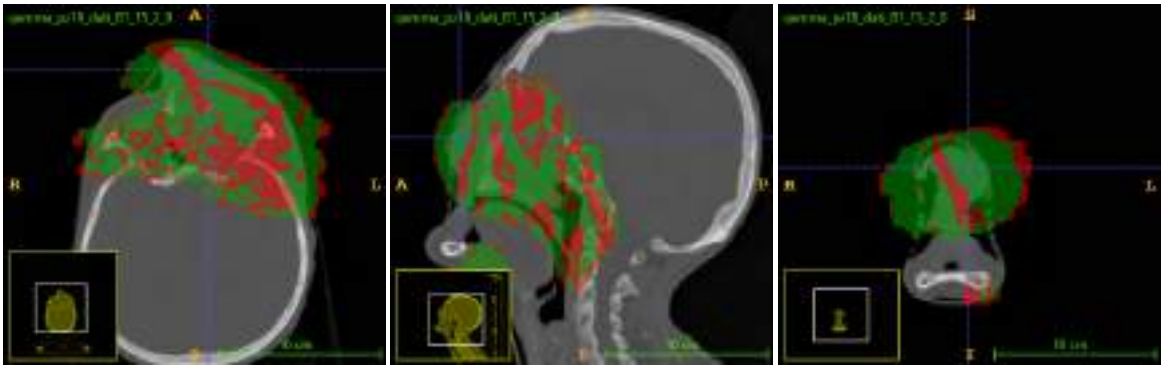

(a)

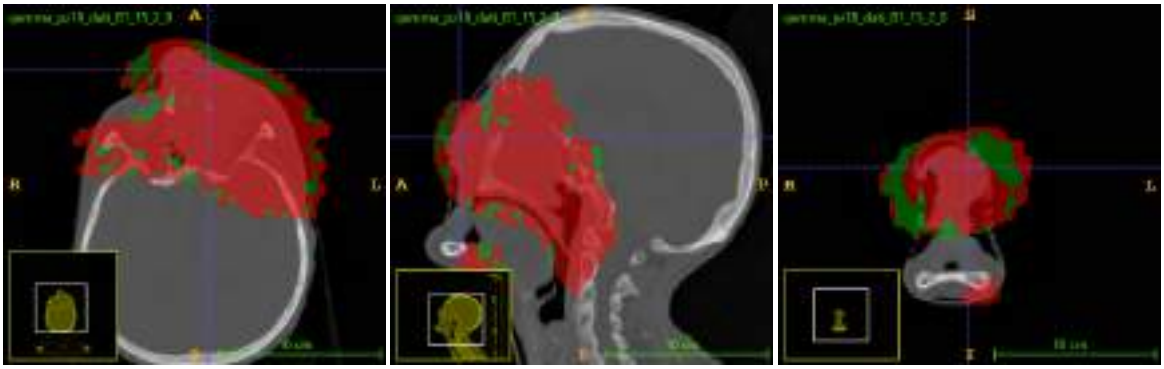

(b)

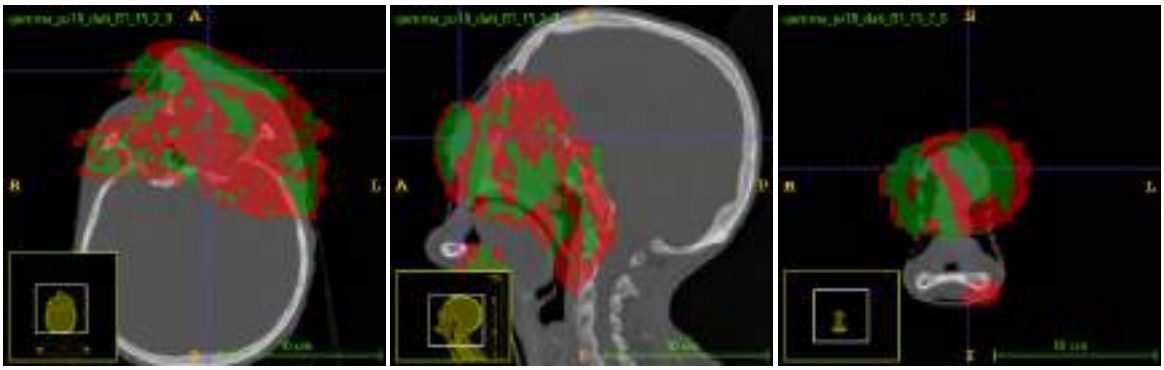

(c)

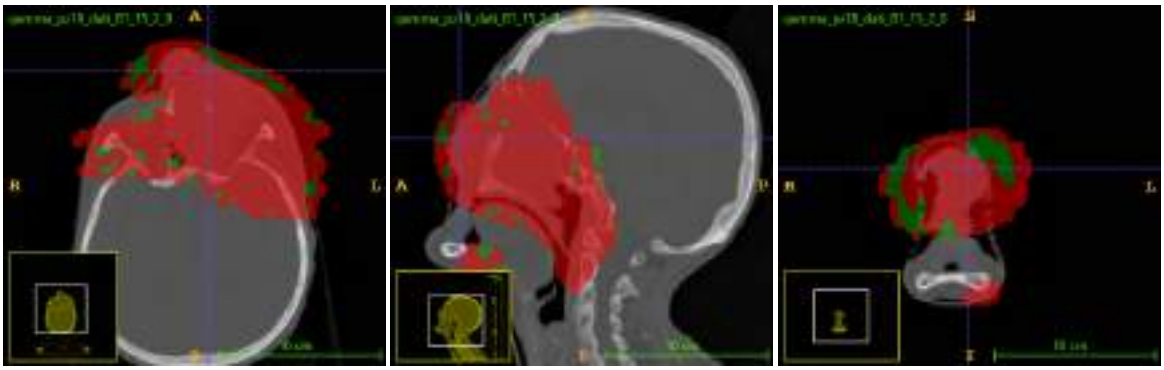

(d)

Figure 4.26: B1 field passrate gamma index maps for fixed DTH = 0.1% and $DD_{min} = 15\%$, $DTA_{min} = 2\,mm$ (a), $DD_{max} = 55\%$, $DTA_{min} = 2\,mm$ (b), $DD_{min} = 15\%$, $DTA_{max} = 10\,mm$ (c), $DD_{max} = 55\%$, $DTA_{max} = 10\,mm$ (d) overlaid on the planning CT.

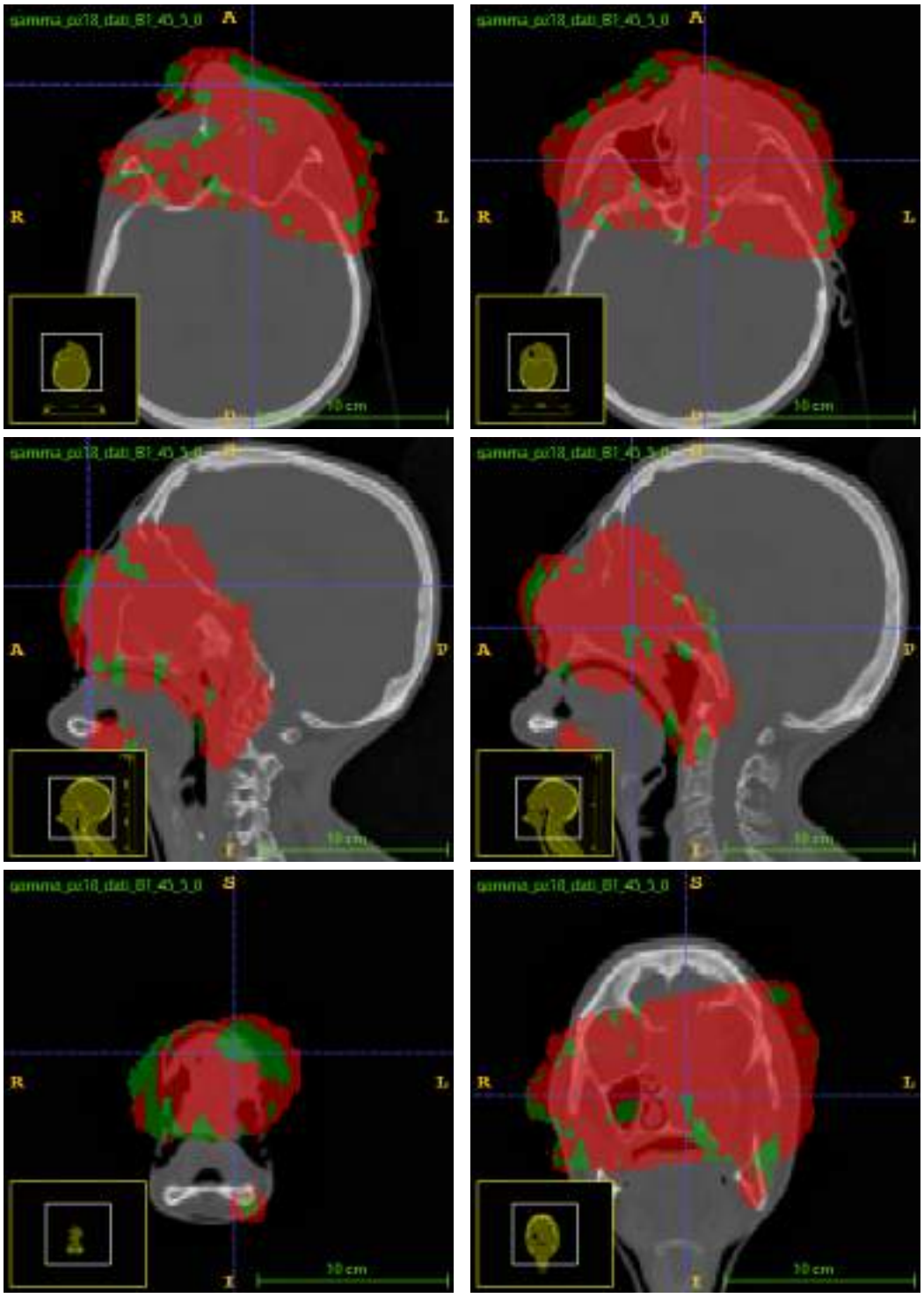

Figure 4.27: B1 field passrate gamma index map for DD = 45%, DTA = 5 mm, and DTH = 0.3% superimposed on the planning CT. The left column displays the partially identified superficial anatomical variation matching Figure 4.21 (a), whereas the right column marginally matches the morphological change shown in Figure 4.21 (c).

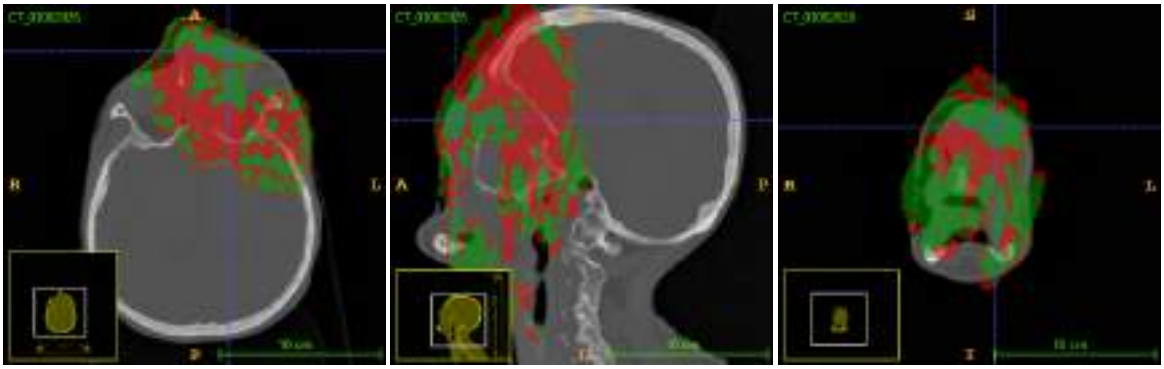

(a)

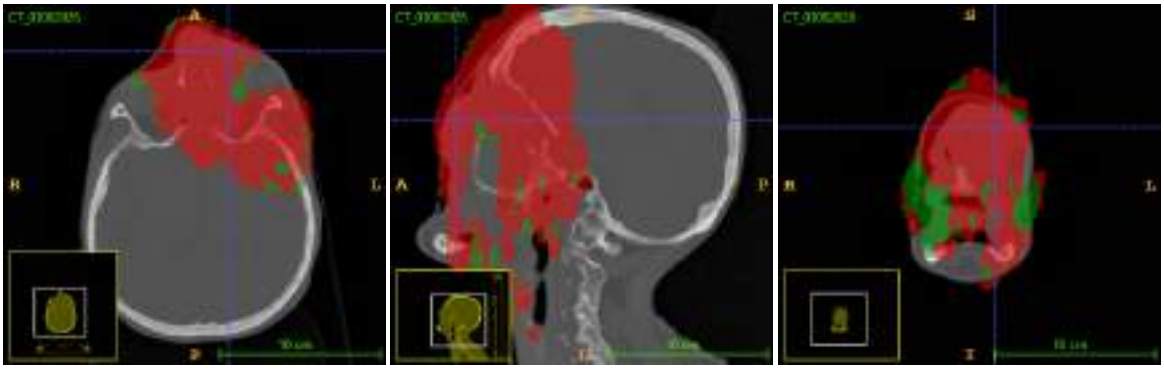

(b)

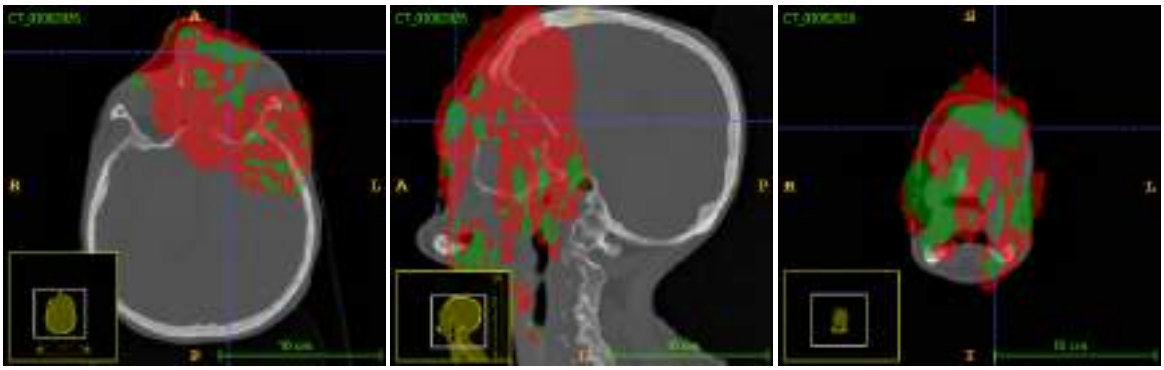

(c)

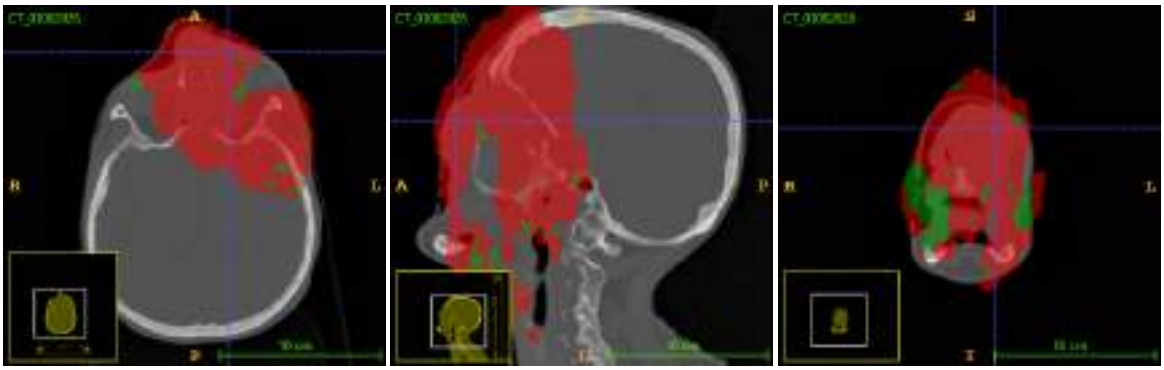

(d)

Figure 4.28: B2 field passrate gamma index maps for fixed DTH = 0.1% and $DD_{min} = 15\%$, $DTA_{min} = 2\,mm$ (a), $DD_{max} = 55\%$, $DTA_{min} = 2\,mm$ (b), $DD_{min} = 15\%$, $DTA_{max} = 10\,mm$ (c), $DD_{max} = 55\%$, $DTA_{max} = 10\,mm$ (d) overlaid on the planning CT.

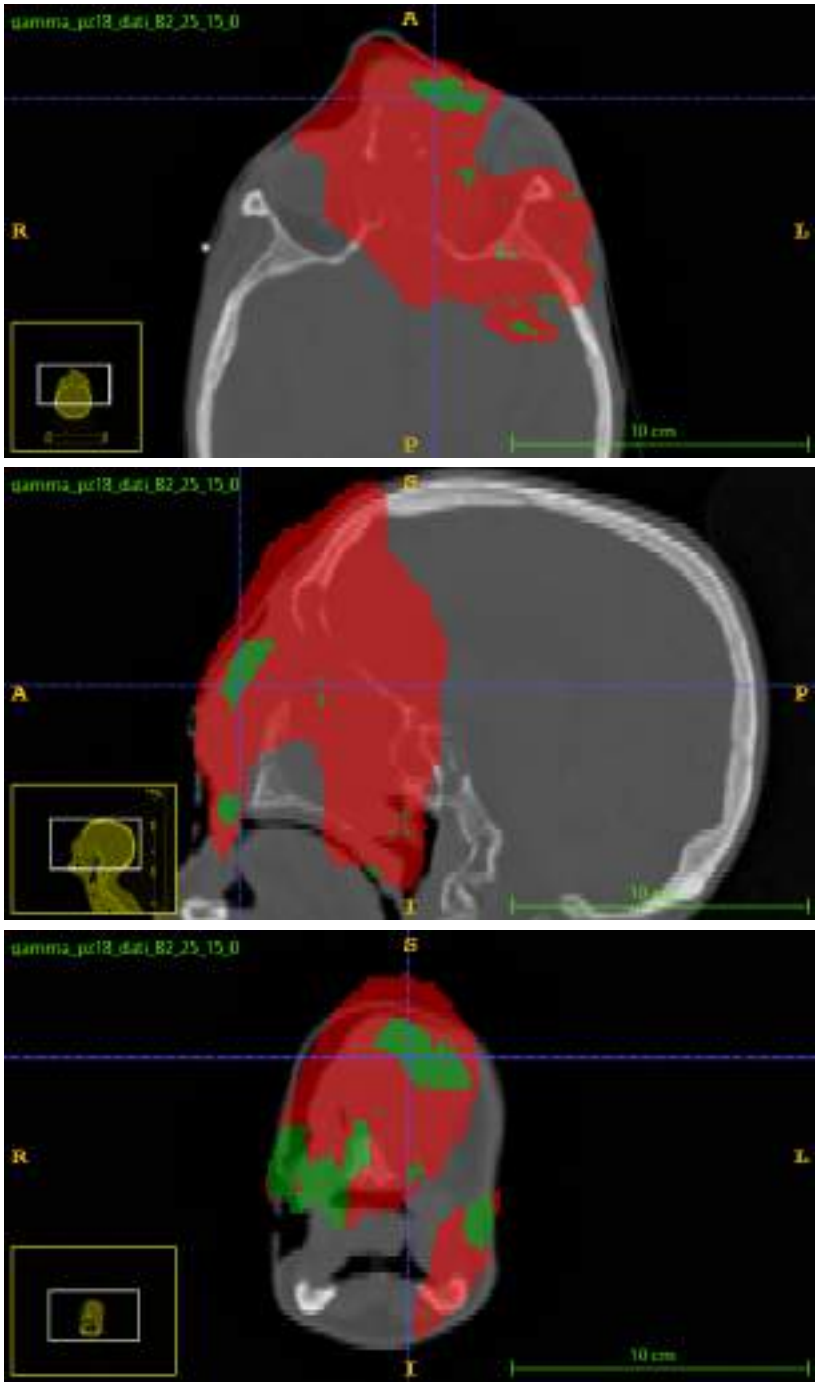

Figure 4.29: B2 field passrate gamma index map for DD = 25%, DTA = 15 mm, and DTH = 0.8% superimposed on the planning CT. The most superficial anatomical change (see Figure 4.21a) is partially identified.

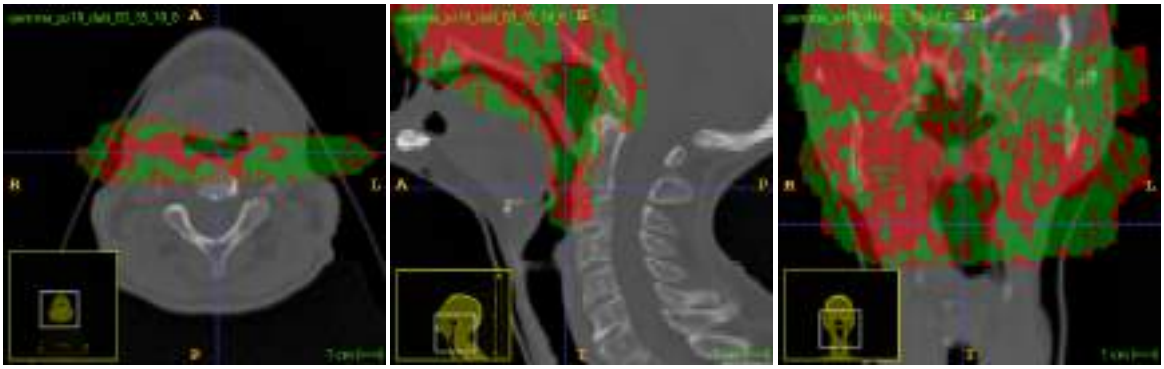

(a)



(b)

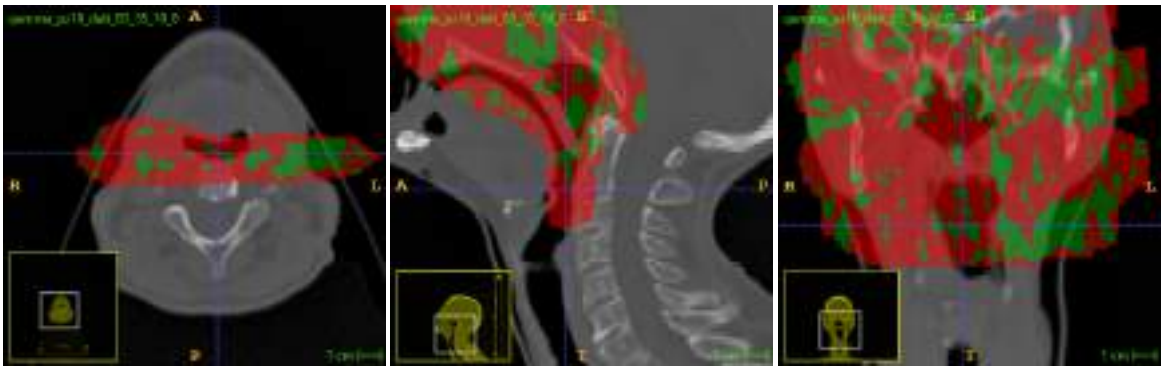

(c)



(d)

Figure 4.30: B3 field passrate gamma index maps for fixed DTH = 0.1% and $DD_{min} = 15\%$, $DTA_{min} = 2\,mm$ (a), $DD_{max} = 55\%$, $DTA_{min} = 2\,mm$ (b), $DD_{min} = 15\%$, $DTA_{max} = 10\,mm$ (c), $DD_{max} = 55\%$, $DTA_{max} = 10\,mm$ (d) overlaid on the planning CT.

Conclusions

This thesis has studied the potential, current challenges and limits of three-dimensional inter-fractional range monitoring in carbon-ion therapy, focusing on the clinical performance of the Dose Profiler detector developed within the INSIDE collaboration and installed in treatment room 1 at the CNAO facility in Pavia. By analysing experimental data from three selected case studies (patients 6, 15, and 18) enrolled in a clinical trial, this work aimed to evaluate whether charged secondary fragment tracking can detect inter-fractional morphological changes occurring during the treatment's course.

The data analysis pipeline, beginning with pixel clustering and Hough transform track reconstruction, to point of closest approach three-dimensional emission distributions and statistical gamma index evaluation, partially demonstrated the feasibility of reconstructing charged secondary particle trajectories to map morphological variations within the patient's anatomy. The implementation of optimisation metrics, specifically efficiency (ε) and purity (δ), provided quantitative information to balance detection sensitivity against statistical noise, yielding optimised parameter triplets (DD, DTA, DTH) that minimised false positives within the gamma index passrate distributions. The absence of Monte Carlo simulated datasets for patients 15 and 18 precluded the use of gamma index parameter optimisation to determine the optimal $(\mathrm{DD}, \mathrm{DTA}, \mathrm{DTH})$ configuration. To mitigate this restriction, the emission density difference between two compared treatment fractions and relative percentage difference distributions were incorporated into the data analysis workflow.

In the Monte Carlo analysis, the gamma index test partially highlighted the deep-seated morphological change in patient 6, yielding an efficiency of $\approx 21\%$ and a purity of $\approx 37\%$. The comparison between experimental data and MC simulations in the case study of patient 6 revealed the impact of geometrical setup and procedural uncertainties: small variations in the patient's positioning result in a less efficient evaluation of the purity and efficiency metrics, therefore affecting the choice of best gamma index triplet parameters, while temporal gaps between planning CT acquisition and the start of treatment may allow spontaneous anatomical changes to resolve prior to the first treatment fraction. These results justified the motives behind the acquisition of an additional control CT scan on the day of the first fraction in the second phase of the CNAO clinical trial.

However, several physical and methodological limitations arose from the analysis of the selected patients: detection sensitivity is limited by the spatial distribution of charged secondary fragments, as particles generated in deep-seated areas undergo significant attenuation

and multiple Coulomb scattering as they traverse large thicknesses of tissue before exiting the patient and reaching the detector. Consequently, the monitoring of deep neoplasms, such as those evaluated in patient 6, 15, and in the B3 field of patient 18, is impaired by low event statistics, making it challenging to isolate true anatomical variations from statistical fluctuations without prior quantitative and spatial knowledge of the variation. In the specific case of patient 15, this constraint is further aggravated by the low number of primary particles prescribed by the treatment plan, which intrinsically reduces the production of charged secondary fragments. For patient 18, the Dose Profiler partially captured inter-fractional anatomical changes matching the Hounsfield Units difference maps when dealing with fields characterised by favourable geometry and superficial morphological variations, such as B1 and B2. In contrast, the B3 field suffered from severe statistical limitations, preventing the detection of deep-seated anatomical changes.

The results obtained in this work suggest that future developments should focus on refining the gamma index optimisation criteria, supported by Monte Carlo simulations, to allow more accurate and precise identification of local density variations. Moreover, extending the analysis pipeline to a broader patient cohort will enable better understanding regarding the possibility to establish standardised gamma index parameters for clinical applications.

In conclusion, while range monitoring with the Dose Profiler is constrained by low statistics and systematic patient positioning uncertainties, this thesis contributes to bridging the gap between purely research environments and routine clinical workflows. As charged particle therapy continues to develop toward higher-precision results, tools like the Dose Profiler represent a step forward in the efforts to support clinicians in delivering safer treatments individually tailored to cancer patients.

Bibliography

[1] Robert R. Wilson. "Radiological Use of Fast Protons". In: *Radiology* 47.5 (1946), pp. 487–491. DOI: 10.1148/47.5.487.

[2] World Health Organization. https://www.who.int/health-topics/cancer.

[3] Marco Durante, Roberto Orecchia, and Jay S. Loeffler. "Charged-particle therapy in cancer: clinical uses and future perspectives". In: *Nature Reviews Clinical Oncology* 14.8 (2017), pp. 483–495. DOI: 10.1038/nrclinonc.2017.30. URL: https://doi.org/10.1038/nrclinonc.2017.30.

[4] H. Paganetti. "Relative biological effectiveness (RBE) values for proton beam therapy: Variations as a function of biological endpoint, dose, and linear energy transfer". In: *Physics in Medicine and Biology* 59.22 (Nov. 2014). Epub 2014 Oct 31, R419–R472. DOI: 10.1088/0031-9155/59/22/R419.

[5] F. Tommasino, E. Scifoni, and M. Durante. "New ions for therapy". In: *International Journal of Particle Therapy* 2.3 (2016). Epub 2016 Feb 9, pp. 428–438. DOI: 10.14338/IJPT-15-00027.1.

[6] Jac Nickoloff. "Photon, light ion, and heavy ion cancer radiotherapy: paths from physics and biology to clinical practice". In: *Annals of Translational Medicine* 3.21 (2015). ISSN: 2305-5847.

[7] Timothy D. Malouff et al. "Carbon Ion Therapy: A Modern Review of an Emerging Technology". In: *Frontiers in Oncology* 10 (Feb. 2020), p. 82. DOI: 10.3389/fonc.2020.00082.

[8] Frank Herbert Attix. "Charged-Particle Interactions in Matter". In: *Introduction to Radiological Physics and Radiation Dosimetry*. John Wiley & Sons, Ltd, 1986. Chap. 8, pp. 160–202. ISBN: 9783527617135. DOI: 10.1002/9783527617135.ch8.

[9] DONALD E. GROOM, NIKOLAI V. MOKHOV, and SERGEI I. STRIGANOV. "MUON STOPPING POWER AND RANGE TABLES 10 MeV–100 TeV". In: *Atomic Data and Nuclear Data Tables* (2001). DOI: https://doi.org/10.1006/adnd.2001.0861.

[10] Niels Bohr. "On the Theory of the Decrease of Velocity of Moving Electrified Particles on Passing through Matter". In: *The London, Edinburgh, and Dublin Philosophical Magazine and Journal of Science*. 6th ser. 25.145 (1913), pp. 10–31. DOI: 10.1080/14786440108634359.

[11] Hans A. Bethe. "Zur Theorie des Durchgangs schneller Korpuskularstrahlen durch Materie". In: *Annalen der Physik* 397.3 (1930), pp. 325–400. DOI: 10.1002/andp.19303970303.

[12] Felix Bloch. "Zur Bremsung rasch bewegter Teilchen beim Durchgang durch Materie". In: *Zeitschrift für Physik* 81 (1933), pp. 363–376. DOI: 10.1007/BF01339455.

[13] W. Leo. *Techniques for Nuclear and Particle Physics Experiments: A How-to Approach*. Berlin, Heidelberg: Springer-Verlag, 1987.

[14] Michael Plum. "Interceptive Beam Diagnostics-Signal Creation and Materials Interactions". In: *AIP Conference Proceedings* (2004). DOI: 10.1063/1.1831132.

[15] W. Ulmer. *The role of electron capture and energy exchange of positively charged particles passing through matter*. 2011. arXiv: 1109.2509 [physics.med-ph]. URL: https://arxiv.org/abs/1109.2509.

[16] Harald Paganetti and Thomas Bortfeld. *Proton Beam Radiotherapy – The State of the Art*. AAPM 2005 Annual Meeting Syllabus. Massachusetts General Hospital, Boston, MA, USA. 2005.

[17] C. Stengl. "In-phantom dosimetry study for target and organs at risk during breathing induced motion: Improving pancreatic cancer treatment by combining carbon ion and mini-beam irradiation". In: *PhD thesis* (2020). DOI: 10.11588/heidok.00036762.

[18] N. J. Carron. *An Introduction to the Passage of Energetic Particles through Matter*. 1st ed. CRC Press, 2006. Chap. 4. DOI: 10.1201/9781420012378.

[19] C.-A. Reidel. "Applications for CMOS pixel sensors in ion-beam therapy". In: *Ecole Doctorale de Physique et Chimie-Physique, Institut Pluridisciplinaire Hubert Curien. PhD thesis. Strasbourg, France: Universite de Strasbourg* (2016).

[20] Gerald R. Lynch and Orin I. Dahl. "Approximations to multiple Coulomb scattering". In: *Nuclear Instruments and Methods in Physics Research Section B: Beam Interactions with Materials and Atoms* 58.1 (1991), pp. 6–10. ISSN: 0168-583X. DOI: https://doi.org/10.1016/0168-583X(91)95671-Y.

[21] R. L. Workman et al. "Review of Particle Physics". In: *Progress of Theoretical and Experimental Physics* 2022 (2022), p. 083C01. DOI: 10.1093/ptep/ptac097.

[22] Schardt Dieter and Elsasser Thilo. "Heavy-ion tumor therapy: Physical and radiobiological benefits." In: *Reviews of modern physics* (2010).

[23] E Haettner et al. "Experimental study of nuclear fragmentation of 200 and 400 MeV/u12C ions in water for applications in particle therapy". In: *Physics in Medicine & Biology* (2013). DOI: 10.1088/0031-9155/58/23/8265.

[24] R. Serber. “Nuclear Reactions at High Energies”. In: *Phys. Rev.* 72 (11 Dec. 1947), pp. 1114–1115. DOI: 10.1103/PhysRev.72.1114.

[25] K. Gunzert-Marx et al. “Secondary beam fragments produced by 200 MeV/u 12C ions in water and their dose contributions in carbon ion radiotherapy”. In: *New Journal of Physics 10.7* (2008). DOI: 10.1088/1367-2630/10/7/075003.

[26] J. D. Harrison and C. Streffer. “The ICRP protection quantities, equivalent and effective dose: their basis and application”. In: *Radiation Protection Dosimetry* 127.1-4 (Nov. 2007), pp. 12–18. ISSN: 0144-8420. DOI: 10.1093/rpd/ncm248.

[27] B. Milborne et al. “The use of biomaterials in internal radiation therapy”. In: *Recent Progress in Materials 2* (2020). DOI: 10.21926/rpm.2002012.

[28] Peggy L. Olive. “The Role of DNA Single- and Double-Strand Breaks in Cell Killing by Ionizing Radiation”. In: *Radiation Research* 150.5 (1998), S42–S51. ISSN: 00337587, 19385404.

[29] H. Rodney Withers. “The Four R’s of Radiotherapy”. In: *Advances in Radiation Biology*. Ed. by John T. Lett and Howard Adler. Vol. 5. Advances in Radiation Biology. Elsevier, 1975, pp. 241–271. DOI: https://doi.org/10.1016/B978-0-12-035405-4.50012-8.

[30] International Commission on Radiation Units and Measurements. *Linear Energy Transfer*. Tech. rep. Report 16. Washington, DC: ICRU, 1970.

[31] Ugo Amaldi and Gerhard Kraft. “Radiotherapy with beams of carbon ions”. In: *Reports on Progress in Physics* 68.8 (2005), pp. 1861–1882. DOI: 10.1088/0034-4885/68/8/R04.

[32] Thomas Friedrich, Marco Durante, and Michael Scholz. “The Local Effect Model - Principles and Applications”. In: 2013. URL: https://api.semanticscholar.org/CorpusID:9485701.

[33] Eric J. Hall and Amato J. Giaccia. *Radiobiology for the Radiologist*. 8th. Lippincott Williams & Wilkins, 2018. ISBN: 978-1-4963-3541-8.

[34] John F. Fowler. “The linear-quadratic formula and progress in fractionated radiotherapy”. In: *British Journal of Radiology* 62.740 (Aug. 1989), pp. 679–694. ISSN: 0007-1285. DOI: 10.1259/0007-1285-62-740-679.

[35] K. H. Chadwick and H. P. Leenhouts. “A molecular theory of cell survival”. In: *Physics in Medicine & Biology* 18.1 (1973), pp. 78–87. DOI: 10.1088/0031-9155/18/1/007.

[36] Eleanor A. Blakely et al. “Inactivation of Human Kidney Cells by High-Energy Monoenergetic Heavy-Ion Beams”. In: *Radiation Research* 80.1 (1979), pp. 122–160. DOI: 10.2307/3575121.

[37] Antje-Christin Knopf and Antony Lomax. “In vivo proton range verification: a review”. In: *Physics in Medicine & Biology* 58.15 (July 2013), R131. DOI: 10.1088/0031-9155/58/15/R131. URL: https://doi.org/10.1088/0031-9155/58/15/R131.

[38] J. Chavaudra and A. Bridier. "Définition des volumes en radiothérapie externe : rapports ICRU 50 et 62". In: *Cancer/Radiothérapie* 5.5 (2001), pp. 472–478. ISSN: 1278-3218. DOI: https://doi.org/10.1016/S1278-3218(01)00117-2.

[39] Katia Parodi. "PET monitoring of hadrontherapy". In: *Nuclear Medicine Review* 15.C (2012), pp. 37–42. ISSN: 1644-4345.

[40] J. Krimmer et al. "Prompt-gamma monitoring in hadrontherapy: A review". In: *Nuclear Instruments and Methods in Physics Research Section A: Accelerators, Spectrometers, Detectors and Associated Equipment* 878 (2018). Radiation Imaging Techniques and Applications, pp. 58–73. ISSN: 0168-9002. DOI: https://doi.org/10.1016/j.nima.2017.07.063.

[41] Silvia Muraro et al. "Monitoring of Hadrontherapy Treatments by Means of Charged Particle Detection". In: *Frontiers in Oncology* Volume 6 - 2016 (2016). ISSN: 2234-943X. DOI: 10.3389/fonc.2016.00177.

[42] Jorge Lerendegui-Marco et al. "Simultaneous neutron and gamma imaging system for real time range and dose monitoring in Hadron Therapy and nuclear security applications". In: *EPJ Web of Conferences* 261 (Jan. 2022), p. 05001. DOI: 10.1051/epjconf/202226105001.

[43] L Piersanti et al. "Measurement of charged particle yields from PMMA irradiated by a 220 MeV/u 12C beam". In: *Physics in Medicine & Biology* 59.7 (2014), p. 1857. DOI: 10.1088/0031-9155/59/7/1857.

[44] Fondazione CNAO. *Fondazione CNAO Website*. https://fondazionecnao.it/en/.

[45] Michela Marafini et al. "The INSIDE Project: Innovative Solutions for In-Beam Dosimetry in Hadrontherapy". In: *Acta Physica Polonica A* 127 (May 2015), pp. 1465–1467. DOI: 10.12693/APhysPolA.127.1465.

[46] G. Traini et al. "Review and performance of the Dose Profiler, a particle therapy treatments online monitor". In: *Physica Medica* 65 (2019), pp. 84–93. ISSN: 1120-1797. DOI: https://doi.org/10.1016/j.ejmp.2019.07.010.

[47] G. Traini. "Development of an innovative device for beam range monitoring in particle therapy". Available at https://hdl.handle.net/20.500.14242/90226. Ph.D. thesis. Rome, Italy: Sapienza University of Rome, 2018.

[48] Istituto Nazionale di Fisica Nucleare. *Osservare le radiazioni in tempo reale per rendere ancora più precise le terapie oncologiche*. URL: https://www.infn.it/osservare-le-radiazioni-in-tempo-reale-per-rendere-ancora-piu-precise-le-terapie-oncologiche/.

[49] R. Ricotti et al. "Long-time clinical experience in patient setup for several particle therapy clinical indications: management of patient positioning and evaluation of setup reproducibility and stability". In: *British Journal of Radiology* 93.1107 (Mar. 2020). DOI: 10.1259/bjr.20190595.

[50] Richard O. Duda and Peter E. Hart. "Use of the Hough transformation to detect lines and curves in pictures". In: *Commun. ACM* 15 (1972). ISSN: 0001-0782. DOI: 10.1145/361237.361242.

[51] Rene Brun and Fons Rademakers. "ROOT — An object oriented data analysis framework". In: *Nuclear Instruments and Methods in Physics Research Section A: Accelerators, Spectrometers, Detectors and Associated Equipment* 389.1–2 (1997). Ed. by M. Werlen and D. Perret-Gallix, pp. 81–86. DOI: 10.1016/S0168-9002(97)00048-X.

[52] Jr. Bidgood W. D. et al. "Understanding and using DICOM, the data interchange standard for biomedical imaging". In: *Journal of the American Medical Informatics Association* 4.3 (May 1997), pp. 199–212. DOI: 10.1136/jamia.1997.0040199.

[53] Paul A. Yushkevich et al. "User-Guided 3D Active Contour Segmentation of Anatomical Structures: Significantly Improved Efficiency and Reliability". In: *Neuroimage* 31.3 (2006), pp. 1116–1128.

[54] ITK-SNAP Official Website. *ITK-SNAP: Interactive Software for Image Segmentation*. URL: http://www.itksnap.org.

[55] Mohammad Hussein, Catharine Clark, and Andrew Nisbet. "Challenges in calculation of the gamma index in radiotherapy – Towards good practice". In: *Physica Medica* 36 (Apr. 2017), pp. 1–11. DOI: 10.1016/j.ejmp.2017.03.001.

[56] Daniel A. Low et al. "A technique for the quantitative evaluation of dose distributions". In: *Medical Physics* 25.5 (1998), pp. 656–661. DOI: https://doi.org/10.1118/1.598248.

[57] M. Pini. "3D Inter-Fractional Monitoring in ^{12}C Ion Therapy: Simulation Study of MULTIPASS Detector Performance in the framework of the INSIDE Clinical Trial at CNAO". Available at https://medusa.mi.infn.it/wp-content/uploads/2026/02/Tesi_Magistrale_MPini.pdf. Master's thesis. Statale University of Milan, 2026.

[58] G. Giacchi. "Monitoraggio 3D inter-frazione delle variazioni morfologiche in trattamenti con ioni ^{12}C al CNAO tramite rivelazione di frammenti secondari carichi". Master's thesis. Sapienza Università di Roma, 2022.

[59] F. Ballarini et al. "The FLUKA code: Overview and new developments". In: *EPJ Nuclear Sciences and Technologies* 10 (2024), p. 16. DOI: 10.1051/epjn/2024015.

[60] T. T. Bohlen et al. "The FLUKA Code: Developments and Challenges for High Energy and Medical Applications". In: *Nuclear Data Sheets* 120 (2014), pp. 211–214. DOI: 10.1016/j.nds.2014.07.049.

[61] A. Ferrari et al. *FLUKA: A multi-particle transport code*. Tech. rep. CERN-2005-010, INFN/TC-05/11, SLAC-R-773. Geneva: CERN, 2005. DOI: 10.5170/CERN-2005-010.

[62] G. Battistoni et al. "The FLUKA Code: An Accurate Simulation Tool for Particle Therapy". In: *Frontiers in Oncology* 6 (2016), p. 116. DOI: 10.3389/fonc.2016.00116.

[63] *FLUKA – A fully integrated particle physics Monte Carlo code*. https://www.fluka.org/.

[64] FLUKA Collaboration. *Flair User Guide 2023*. 2023. URL: http://www.fluka.org/flair/index.html.

[65] Leonardo Lampertico. "Inter-fractional monitoring of ^{12}C ion treatments with the Dose Profiler detector: simulation studies and clinical trial results at the CNAO facility". Corso di Laurea Magistrale in Fisica. Master's Thesis. Università degli Studi di Milano, 2024.

[66] Ilmo Leivo. "Intestinal-Type Adenocarcinoma: Classification, Immunophenotype, Molecular Features and Differential Diagnosis". In: *Head and Neck Pathology* 11.3 (2017), pp. 295–300. ISSN: 1936-0568. DOI: 10.1007/s12105-017-0800-7.